Fakultät für Physik
Technische Universität München

Multimessenger searches for the sources of high energy cosmic rays: IceCube, Fermi, Auger, TA.

Andrea Turcati

Vollständiger Abdruck der von der Fakultät für Physik der Technischen Universität München zur Erlangung des akademischen Grades eines

Doktors der Naturwissenschaften (Dr. rer. nat.)

genehmigten Dissertation.

Vorsitzender:
Prof. Dr. Andreas Weiler

Prüfende der Dissertation:
1. Prof. Dr. Elisa Resconi
2. Prof. Dr. Lothar Oberauer

Die Dissertation wurde am 01.07.2019 bei der Technischen Universität München eingereicht und durch die Fakultät für Physik am 13.08.2019 angenommen.

Thesis advisor: Professor Prof. Elisa Resconi Andrea Turcati

Multimessenger searches for the sources of high energy cosmic rays: IceCube, Fermi, Auger, TA.

ABSTRACT

The results of multiple analyses using different astrophysical messengers are presented in this thesis. The first test to be reported is a two-point autocorrelation analysis using seven years of neutrino data recorded by the IceCube Neutrino Observatory. No significant evidence of clustering of neutrino events at small angular scales is observed, thus upper limits are calculated for the northern and southern sky separately. The second analysis focuses on the population of sources of blazars of the *BL Lac* type, more specifically on the objects presenting a synchrotron peak located at high frequencies. The correlation between IceCube neutrino events and catalogs of γ-ray sources is investigated as a starting point for the development of a three-messenger analysis. The catalogs included in the search are the *Third Catalog of Hard Fermi*-LAT sources and the third version of the *WISE High Synchrotron Peaked* Catalog. No significant evidence of correlation is reported. The goal of the third analysis is to include in the same correlation framework the information of ultra-high-energy cosmic ray events recorded by the Pierre Auger Observatory and Telescope Array. Despite the absence of significant correlation, conclusions can be extracted from the analysis, providing an outlook for future iterations of the test. The final analysis presents the first quantitative test aimed at connecting astrophysical neutrinos from the IceCube experiment and AGN outflows. Based on the same correlation analysis presented in the previous parts, constraints on different models of neutrino emission from AGN outflows can be placed.

Thesis advisor: Professor Prof. Elisa Resconi Andrea Turcati

Zusammenfassung

Die Resultate von mehreren Analysen, die unterschiedliche astrophysikalische Messenger verwenden, werden in dieser Arbeit präsentiert. Zuerst werden Ergebnisse einer zwei-punkt Autokorrelationsanalyse, von sieben Jahren IceCube Neutrino Daten, präsentiert. Keine signifikanten Häufungen von Neutrino Events bei kleinen Winkelskalen wird gesehen und daraus wurden obere Schranken für den Nord- und Südhimmel bestimmt. Die zweite Analyse behandelt *BL Lac* Quellen, Objekte die einen Synchrotron Peak bei hohen Energien aufweisen. Dafür wurde die Korrelation zwischen IceCube Neutrino Events und Katalogen von Gamma-Ray Quellen untersucht. Dies dient als erster Schritt einer drei-messenger Analyse. Die verwendeten Kataloge sind *Third Catalog of Hard Fermi*-LAT Quellen und die dritte Version des *WISE High Synchrotron Peaked* Katalogs. Signifikante Korrelationen wurden nicht gefunden. Die dritte Analyse nimmt das vorige Korrelationsframework und inkludiert ulra-high-energy cosmic ray events gemessen vom Pierre Auger Observatorium und dem Telescope Array. Obwohl keine Korrelation gefunden wurde, können Rückschlüsse auf zukünftige Analysen dieser Form geschlossen werden. Zuletzt wird der erste quantitative Test einer Korrelation zwischen astrophysikalischen neutrinos, gemessen von IceCube und AGN Outflows gemacht. Diese Analyse beruht auf den früheren dreien und führt zu Grenzen für verschiedene Modelle, die Neutrinoemission von AGNs beschreiben.

Contents

Introduction

The IceCube Neutrino Observatory has by now established its pivotal role in the newborn field of multimessenger astronomy. After the first discovery and measurement of an astrophysical neutrino flux [1, 2] in 2013, the tied relationship between different astrophysical disciplines was made clear in 2017 by the observation of an extremely-high-energy neutrino event at the location of a γ-ray emitting object in correspondence of a flaring state [3]. This exciting result also highlighted the many challenges that the scientific community has to face in order to gain a deeper knowledge on the processes that characterize our universe. These difficulties can be looked at from different points of view: physical, mathematical, computational and organizational, but they all provide a very inspiring outlook from the way they are one by one tackled and solved.

In this thesis, I will report my contribution to the path towards establishing multimessenger astronomy. In order to build a comprehensive analysis, starting from the IceCube neutrinos, all the information provided by γ-ray photons and Ultra High Enegy Cosmic Rays will be introduced. Every chapter is written with the intent of providing a new step towards gaining an insight to the complete multimessenger picture and along the way the most recent results will be presented. At the end of each chapter I will also provide an outlook and the description of the main challenges that each step presents. The structure of the Thesis is summarised in the following:

- *Chapter 1* - In the first chapter, the physics of the three particles at the center of this Thesis is introduced. The current information we have about cosmic rays is presented, together with the principles of their acceleration in astrophysical environments. The focus is then moved to two neutral particles: γ-ray photons and neutrinos, highlighting their importance for multimessenger astronomy.

- *Chapter 2* - Two different classes of putative cosmic rays sources are described in the second chapter. Active Galactic Nuclei, with particolar focus on blazars of the *BL-Lac* type, are discussed in detail from a multi-wavelength viewpoint. A second class of sources, Active Galactic Nulclei presenting ultra-relativistic outflows, is then introduced together with their physical mechanisms of particle acceleration.

- *Chapter 3* - This chapter will introduce the reader to the IceCube Neutrino Observatory. The detector itself is discussed in great detail before explaining all the steps of a neutrino event reconstruction. The focus of the chapter is on neutrino events that provide the best astronomical information. The status of the knowledge about the measured astrophysical neutrino flux is here summarised.

- *Chapter 4* - The most recent results of a two-point autocorrelation analysis performed on 7 years of IceCube data is here reported. After an introduction on the statistical method and a comparison to complementary methods, both results of the autocorrelation analysis and current upper limits are presented. A closer look at the interesting galactic area of the *Cygnus Region* is also reported.

- *Chapter 5* - In this chapter, the second messenger (γ-rays) will be finally introduced as a starting point to build a more complex analysis with three messengers. After a brief summary on the status of the IceCube analyses investigating the connection between the astrophysical neutrino flux and different γ-ray catalogs, a statistical method to look for correlations between the most interesting neutrino events and different *Fermi*-LAT γ-ray sources is described. The results of this method are then reported, together with a discussion on their possible explanation and an outlook on the method itself. An intuitive mathematical method to calculate the significance of a correlation between a neutrino event and a flaring γ-ray source is then described in a dedicated section.

- *Chapter 6* - This chapter will finally present the complete Counterpart Method with three messengers. The statistical method is described in detail before presenting the most recent results of the analysis. A comparison with previous results and a dedicate discussion will conclude this part which focuses on high-synchrotron-peaked *BL-Lacs*.
- *Chapter 7* - The last chapter applies for the first time the statistical methods discussed in the previous chapter on the population of AGNs with ultra-relativistic outflows. Two different sets of sources are investigated in great detail, providing results that can be used as a solid starting point for future analyses.

1

The three messengers

After more than one hundred years from their discovery, cosmic rays are still one of the most challenging fields of study in modern physics. Many developments have been made over the years, but the main questions still remain unanswered. What are the sources of cosmic rays? What are the mechanisms of their production? What happens during their propagation to the Earth? Every piece of information that can get us closer to the solution of these problems is fundamental to obtaining a deeper understanding on the underlying principles that drive our universe. And while many experiments can be performed on Earth to study the fundamental laws of physics, Cosmic Rays offer a unique window to an energy range that is yet not attainable within a laboratory. This chapter will provide an overview on the properties of Cosmic Rays, with a focus on their high energy components, γ-ray photons and neutrinos.

1.1 Cosmic Rays

We define *Cosmic Rays* (*CRs*) the particles that reach the Earth after being produced and accelerated at astrophysical sources. Protons, α particles and heavier ionized nuclei consititute the largest part of the primary cosmic radiation that hits the atmosphere of our planet. These are the particles usually referred to as CRs. Other elementary particles such as γ-ray photons and neutrinos, despite formally being CRs, are usually treated separately beacause of their importance in the field of multimessenger astronomy.

The energy range covered by CRs spans over twelve orders of magnitude, making them one of the most interesting natural laboratories for particle physics at very different energy scales. The most energetic part of the CR spectrum, where particles present themselves with ultra-relativistic energies up to 10^{20} eV, makes up for only a small fraction of the total flux, but a very promising one. *Ultra High Energy Cosmic Rays* (*UHECR*), if protons will point back to their source, are one of the best probes to discover the origin of the CRs, and to shed light on the mechanisms of production and acceleration of these particles.

Many astronomical parameters enter in the modeling of CR diffusion, leaving room for different interpretations of the phenomenon. Nevertheless, it is clear that only a small fraction of the CRs is produced within our Solar System, while the majority has properties consistent with a galactic origin. The most energetic part of the CRs is instead believed to be produced outside of our Galaxy, in astrophysical accelerators that have yet to be unequivocably identified [4].

In the following sections the main properties of the primary CRs are introduced, along with possible mechanisms that could explain their production and energy spectrum. Dedicated sections will then describe the details of the gamma rays and the neutrinos of astrophysical origin.

1.1.1 ENERGY SPECTRUM, FLUX AND COMPOSITION

The *Differential Energy Spectrum* (Eq. 1.1) is one of the first properties used to characterize CRs. It represents the number of particles at a given energy (E) per unit area (A), time (T) and solid angle (Ω). The integral of this quantity from a given energy to infinity is also sometimes used and quoted as *Integral Energy Spectrum* (Eq. 1.2).

$$\frac{d\Phi(E)}{dE} = \frac{d\left(\frac{N}{A\cdot T}\right)}{d\Omega \cdot dE} \quad \left[\frac{\text{particles}}{cm^2 \cdot sr \cdot s \cdot GeV}\right] \tag{1.1}$$

$$\Phi(E) = \int_E^{+\infty} \phi(E')dE' \quad \left[\frac{\text{particles}}{cm^2 \cdot sr \cdot s}\right] \tag{1.2}$$

Particles that constitute CRs can reach the Earth with energies spanning from 1 GeV to almost 100EeV, nearly twelve orders of magnitude higher in energy. Low energy particles are measured in high abundance, in the order of thousands per second per square meter, while the particles detected at the highest energy are so rare that only a few are expected per square kilometer per century (Figure 1.1). This difference in statistics plays a role in the differing detection techniques used for low and high energy particles. Low energy particles can be measured by relatively small detectors, usually satellite or baloons experiments are preferred in order to avoid backgrounds caused by the atmosphere. These types of detectors are usually also able to determine with precision the particle's type and its energy. UHECRs detection needs instead a very large instrumented area in order to detect a reasonable amount of particles. For this reason, experiments focused on energies higher than $10 \mathrm{TeV}$ are forced to be ground based. They detect *primary* CRs trough the measurement of the particles produced by their interaction with the atmosphere (*secondary* CRs), drastically reducing the precision of the measurement of the primaries. The uncertainty of the energy measurements over the whole spectrum usually scales proportionally to the energy, making a logarithmic scale a natural way to represent the energy spectrum [4].

The differential energy spectrum is showed in Figure 1.1, plotted as $E^2 \cdot \phi = E^2 \cdot dN/dE = E \cdot dN/d\ln E$ which is equivalent to the spectral energy density $\nu F(\nu)$, a common quantity in multiwavelength astronomy, where the letter ν indicates frequency. The spectrum can be in first order approximated with a power law of the type $d\Phi(E)/dE \propto E^{-\gamma}$, with the power law index changing at two different points, the so called *Knee* and *Ankle*. The primary CR energy spectrum begins with a power law index of 2.7, then a hardening to a 3.1 index is observed starting at the Knee around 10^6 GeV, and a softening back to a 2.7 index appears at EeV energies. The spectrum then cuts off at 10^{11} GeV [4, 5]. The most common interpretation of the spectrum changes considers the lower energy part dominated by CR originating in the Solar system. The window between knee and ankle is instead believed to be populated by particles accelerated inside our Galaxy, and only the most energetic tail of the spectrum is thought to be of extragalactic origin.

Protons and helium nuclei represent the vast majority of the CRs. Electrons and positrons are also present, but only at the percent level due to their significant energy

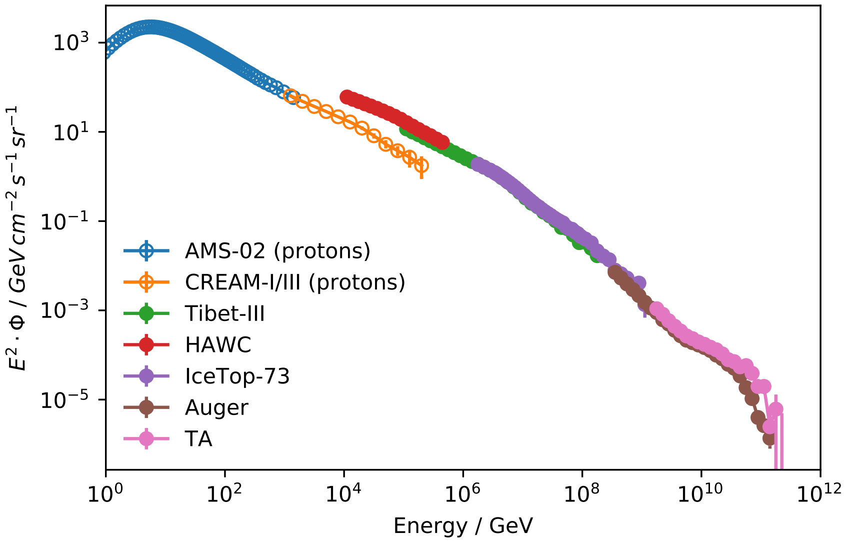

Figure 1.1: Cosmic Ray spectra from different experiments. If not specified otherwise, data points show the *all particles* flux. Statistical plus systematical (where given) errors are shown. Data is taken from [6–12].

losses during propagation. The remaining part of the CRs is made of nuclei heavier than helium, up to $Z \leq 30$. Despite consituting the minority, they can provide important information about the mechanism of CRs diffusion through galactic material. Figure 1.2 shows the relative abundances of different elements in CRs compared to the abundances of the same elements in the Solar System. The abundances are comparable for most of the elements, suggesting that the species present in the CRs originate in an environment with a similar chemical composition to the one of the Solar System. Nevertheless, two groups of elements (Li, Be, B and Sc, Ti, V, Cr, Mn) are overabundant in the CRs by as much as five orders of magnitude. These elements do not enter the CRs from stellar nucleosynthesis and are produced by spallation, that is the collision of cosmic ray particles with the interstellar medium. By knowing the cross sections of these processes, it is then possible to learn about the amount and density of material traversed by the CRs between their production and their observation. The results bring to the conclusion that CRs are confined for a long time in the galaxy before diffusion processes let them escape in the extra-galactic universe[4].

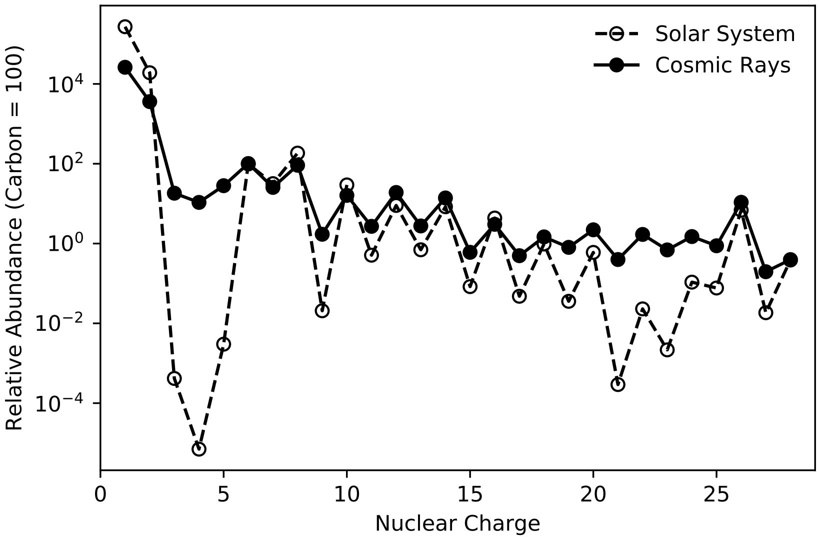

Figure 1.2: Comparison between relative elemental abundances of Cosmic Rays at Earth (solid circle, filled line) and Solar System (open cirlce, dashed line). Reference is Carbon=100. Data is measured at energies between 100 MeV and 1-2 GeV [13].

1.1.2 Galactic Cosmic Rays

The energy region up to a few GeV of the CR spectrum is dominated by the particles accelerated by the Sun. Different experiments like PAMELA have proven this by studying the correlation between the solar activity and the flux of CR arriving at Earth [14, 15]. Starting from ~ 4 GeV, particles accelerated outside our system have enough energy to penetrate the shielding offered by the solar wind.

The CRs produced in our Galaxy are thought to dominate the energy spectrum until 10^{18}eV. Charged particles are bound to interact with galactic magnetic fields, adding a random deflection to their direction. Nevertheless, at these energies the Larmor radius of the particles is usually still smaller than the spatial dimension of the galactic disk, providing confinement inside the galaxy [5].

The smooth steepening of the energy spectrum starting at $3 \cdot 10^6$ GeV (also called *Knee*, see Figure 1.3) is a feature not unequivocally understood yet, traditional explanations ar the *Peters cycles* [4, 16]. Given a maximum energy attainable by particles in a generic accelerator, magnetic fields encountered both at origin and during propagation must characterize the energy spectrum. The relevant quantity to take into consideration is then the *magnetic rigidity* ($R \approx E/Ze$). If a characteristic rigidity exists, particles with different value of Z will cut off at different energies, producing a spectrum with the familiar shape as sketched in Figure 1.4. Different analyses performed by different air-shower experiments seem to suggest the veridicity of this model by showing a change from light to heavy elements in CR composition [17]. The presence of more than one class of galactic CR accelerator is nevertheless not ruled out [4].

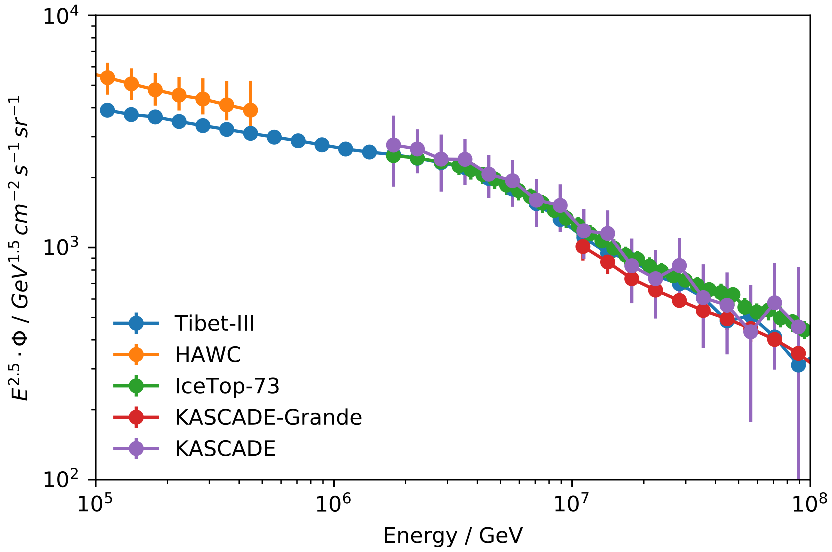

Figure 1.3: Cosmic Ray spectra from different experiments in the energy range of the *Knee*. If not specified otherwise, data points show the *all particles* flux. Statistical plus systematical (where given) errors are shown. Data is taken from [8–10, 16, 18].

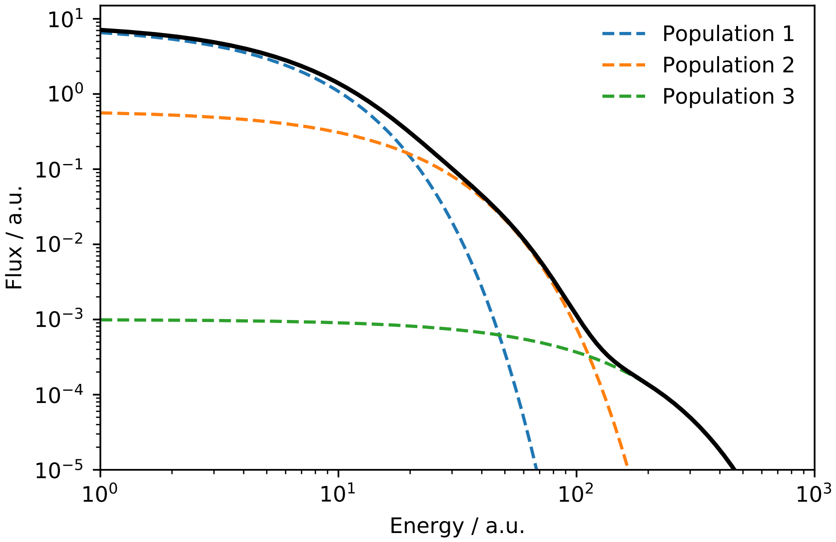

Figure 1.4: Sketch of the total flux (filled black line) obtained assuming three different populations of particles with a different cut-off energy (dashed coloured lines).

1.1.3 ULTRA HIGH ENERGY COSMIC RAYS

Above the *Knee*, the CR energy spectrum can be described with a single power law until the *Ankle* at $\sim 10^9$ GeV. This description is only valid as a first approximation: recent experiments have shown that different features with varying slopes appear in the region between the *Knee* and the *Ankle* [17]. The effect can be explained by overlapping contributions of different species of particles coming from different populations of accelerators [4].

In this energy range particles can escape the magnetic fields at their origin, and travel through intergalactic spaces. The extragalactic origin of these CRs is also supported by the absence of any anisotropy in their arrival direction correlated with the galactic plane. It is important to note that the presence of a dipole anysotropy of CRs above 8 EeV, non correlated with our Galaxy, has been observed by the Pierre Auger Observatory [19].

Above the *Ankle*, the CR from extra-galactic sources are finally thought to dominate over the ones with galactic origin [5]. Finally, the energy spectrum above $6 \cdot 10^{10}$ GeV shows a clear steepening of the power law. It is still unclear if the cut-off is caused by the Greisen-Zatsepin-Kuzmin (GZK) effect, *i.e.* the interaction of CR protons above the energy of $5 \cdot 10^{10}$ GeV with photons of the Cosmic Microwave Background (CMB) producing Δ^+ resonances [20, 21]. Another possible interpretation of the cut-off could be a feature of the CR sources themselves, which might indicate that at this point of the spectrum a maximum energy available for particle acceleration is reached. In this last framework the results of the chemical composition analyses of the UHECR are of fundamental importance. A high percentage of heavy elements in

CRs at these energies, as reported by the latest measurements from the Pierre Auger Observatory (Figure 1.6), might infact suggest the presence of Peter's Cycles at these energies, indicating the existence of a limit in acceleration energies of the CR sources [22–24].

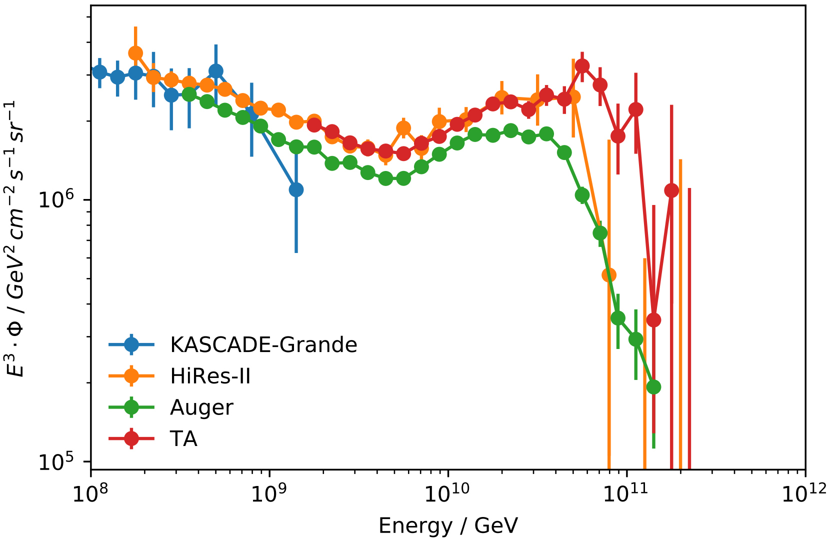

Figure 1.5: Cosmic Ray spectra from different experiments in the energy range of the *Ankle*. If not specified otherwise, data points show the *all particles* flux. Statistical plus systematical (where given) errors are shown. Data is taken from [11, 12, 18, 25].

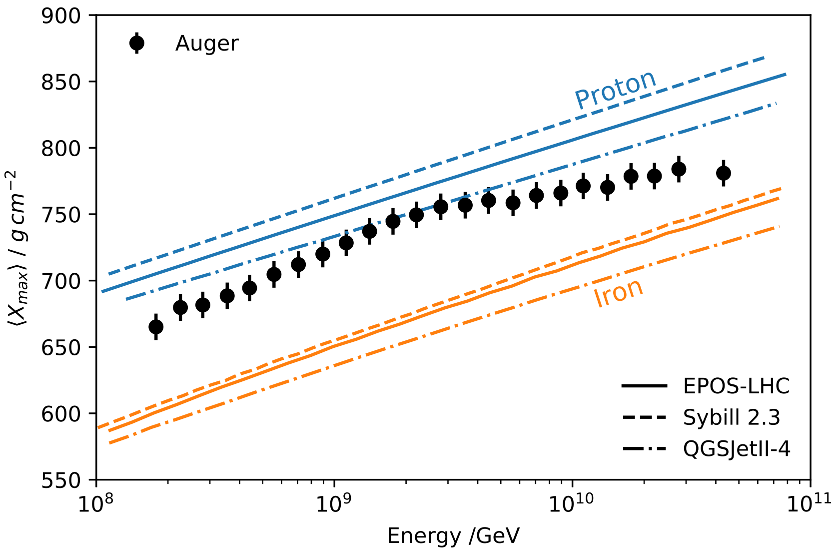

Figure 1.6: Position of the average shower maximum X_{max} versus energy. Measurement from the Pierre Auger Observatory [22] are compared to air shower simulation for protons (orange) and iron (cyan) using different hadronic interaction models.

1.2 CR PRODUCTION AND ACCELERATION

CR particles arrive at Earth with energies much larger than the thermal energies of typical astrophysical environments. Specific acceleration mechanisms different from blackbody radiation are needed to explain the energy spectrum observed. The acceleration processes have to be able to explain the shape of the measured spectrum, once convolved with the effects of the propagation through galactic and intergalactic spaces. This means that charged particles can not be traced back directly to a pointlike source because of the deflection due to magnetic fields. The study of neutral secondaries is then fundamental to pinpoint production and acceleration centers of CRs.

1.2.1 SHOCK ACCELERATION

Historically, the first candidates for particle acceleration in astrophysical phenomena were *supernovae explosions* [26]. They are not only plausible from an energy balance point of view, but the shock wave associated with the explosion served as a starting ground to develop the different acceleration mechanisms that can be used to describe the physics of many different species of astrophysical objects.

FIRST AND SECOND ORDER FERMI ACCELERATION

With a first article in 1949, Enrico Fermi developed the two basic scenarios that model how a particle can be brought to very high energies through multiple repeated interaction with clouds of material. In this framework, large masses of moving magnetized plasma can transfer energy to individual charged particles that happen to collide with them. If the particle remains contained in a delimited region where these collisions are frequent enough, it could be brought to the very high energies measured in CRs. This mechanism, called *Second Order Fermi Acceleration* [27], produces a power law energy spectrum as needed, but its characteristic time is inversely proportional to the square of the cloud velocity. The quadratic dependence makes it much less efficient when compared with the *First Order Fermi Acceleration*[28]. In this other framework, the particles subjet to acceleration are moving between two (or more) mutually approaching clouds of material, or through two zones of material separated by a shock front. The geometry of the plane shock front forces head-on collisions which, in contrast to the interaction of the Second Order mechanism, always produce an increase of energy for the colliding particle. The characteristic time for the acceleration is then drastically reduced, significantly increasing the efficiency of the acceleration.

The most striking feature of the Fermi Acceleration model is that, even though the exact resulting value varies depending on which parameters are used to describe the inner properties of the clouds, the predicted differential spectral index for a standard case of a plane shock front in a monoatomic gas is very close to the one actually observed in the CR energy spectrum [5].

The maximum energy attainable by a charged particle during acceleration processes is always function of its Larmor radius: with a radius large enough, the particle will in fact escape the region in which the acceleration occurs. This dependence poses limits on the maximum energy of shock accelerated CRs that is dependent on the properties of the accelerator, namely its magnetic field and its size (B and R in Eq. 1.3).

$$E_{Max} \propto Ze\beta BR \tag{1.3}$$

1.3 Gamma Rays

The charged particles that constitute the cosmic rays undergo relevant deflections due to magnetic fields during their propagation. This makes the identification and study of the CR sources an almost impossible task by only using the charged fraction of the particles arriving to Earth. Photons are neutral particles that are produced by accelerated electrons and possible also protons, and they have been measured up to very high energies in the CR spectrum. Contrary to charged particles, photons do not get deflected by magnetic fields and point straight to the objects where they originated. While photons are produced through radiation or decay by both leptonic and hadronic processes, neutrinos are instead created only in hadronic processes (see next Section 1.4). The standard naming definition calls photons from $\sim$ 30 MeV to

$100\,\mathrm{GeV}$ *High Energy* (HE) γ-rays, and *Very High Energy* (VHE) γ-rays ones with larger energies.

The Spectral Energy Distribution (SED) of an object represents the energy flux of the object in different energy bands and it is commonly used to characterize different types of astrophysical objects. The quantities plotted in a SED are the *flux density per frequency* ($\nu F(\nu)$ vs. ν), or the equivalent in energy units ($E^2 dN/dE$ vs. E).

1.3.1 The hadronic model

The acceleration of charged hadrons like protons is always accompanied by photons and neutrinos generated by the decay of charged and neutral mesons. These mesons, a majority being pions, are produced by proton-proton collision via standard interaction of the type

$$p + p \rightarrow \pi^{\pm}, \pi^{0}, K^{\pm}, K^{0}, p, n, ... \tag{1.4}$$

These interactions are dominated by inelastic processes, with secondary particles characterized by low transverse momentum values. In analogy with the terrestrial accelerator experiments, these processes are often called by the name of *astrophysical beam dump* [4].

A second process of photon production by protons is similar to the one underlying the GZK cutoff. High energy protons can interact with low energy ambient photons (*photoproduction*), the resonance produced will then decay in the form of secondary mesons:

$$
\begin{aligned}
p + \gamma \rightarrow \Delta^{+} &\rightarrow \pi^{+} + n \qquad (1.5)\\
&\rightarrow \pi^{0} + p \qquad (1.6)
\end{aligned}
$$

The cross section of the former process is two order of magnitude larger than the latter one, nevertheless, in an environment with a high density of ambient photons compared to the density of matter, the photoproduction process might be dominant. Different types of sources will be characterized by different contributions of the two processes [5].

Neutral pions decay in γ-rays:

$$\pi^{0} \rightarrow 2\gamma. \qquad (1.7)$$

The two photons per meson produced by the decay are emitted isotropically in the rest frame, but they are boosted as the meson in the laboratory frame. The consequence is that the γ-ray spectrum, after a steep rise above production threshold energy ($\sim$ 200 MeV), reproduces the original spectrum of the protons. The presence of a so called *pion-decay bump* is an unique feature to identify proton acceleration in astrophysical objects. Neutral pion decay is the main source of diffuse γ-ray radiation inside our Galaxy [4].

1.3.2 The leptonic model

The SED window that goes from radio to soft X-rays is in most objects dominated by the radiation emitted by accelerated electrons propagating through strong magnetic fields. The radiation pattern of the relativistic electron in a magnetic field is beamed in the direction of motion of the electron itself, which bends proportionally to the magnetic field. The spectrum of the radiation emitted depends on the energy of the electron (E) and on the magnitude of the field (B), showing a peak at the *synchrotron frequency* (ν_s)

$$\nu_S \propto BE^2. \tag{1.8}$$

The synchrotron flux from source with radius R at a distance d emitted by a population of particles with a power-law energy distribution $dN/dE \propto E^{-p}$, can be shown to be

$$F(\nu) \propto \frac{R^3}{d^2} B^{1+\alpha} \nu^{-\alpha}, \tag{1.9}$$

where $\alpha = (p-1)/2$. Charged particles with a mass larger than the electron experiment a suppression of the synchrotron radiation proportional to their mass. This implies that proton synchrotron radiation becomes relevant only in extreme objects [5].

The full synchrotron spectrum of a source is observable only if the material surrounding the acceleration region is transparent enough to allow the radiation photon to escape. These sources take the name of *optically thin*. In the opposite case, *optically thick* sources present absorption patterns that modify the shape of the spectrum. *Synchrotron self-absorption* takes place when charged particles interact with the emitted synchrotron photons. Depending on their frequency ν, photons will travel different lengths inside the material, permitting high-energy photons to travel through the entire absorption region, while the lower energy ones are able to escape only if produced close enough to the edge of the source. In an asymptotical case, for an optically thick source this reflects in a differential power emitted that is not dependent on the energy distribution of the emitting particles ($\propto \nu^{5/2}$). The more common case will present a differential spectrum in which the emitted power increases with the frequency until it reaches a peak, then it will fall off with the same powerl-law α of the emitting particles.

Another important secondary radiaton process is *Inverse Compton* scattering. Contrary to standard Compton emission, in which an electron at rest scatters with a high-energy photon. In this case it is the accelerated charged particle that donates part of its energy to an ambient photon. Depending on the energy of the photon, this process is regulated by the classical Thompson cross section ($E_\gamma \ll m_e c^2$) or by the Klein-Nishina cross section ($E_\gamma \gg m_e c^2$). The former case being much more efficient when compared to the latter. This type of interaction takes advantage of a factor of Γ^2 in boosting the photon energy, permitting to a photon in the Thompson regime to easily gain a large amount of energy in a reasonable amount of scatterings.

1.3.3 EXTRAGALACTIC BACKGROUND LIGHT

Once the distance to a γ-ray source is larger than the mean free path of a photon, the Universe becomes opaque to γ-rays with high energies. The main process of photon absorption is pair production through scattering with ambient low energy photons

$$\gamma + \gamma_{\mathrm{Amb.}} \rightarrow e^+ + e^-. \tag{1.10}$$

The ambient photons cover an energy range that goes from the Cosmic Microwave Background (CMB) to Ultraviolet wavelengths. These photons take the name of *Extragalactic Background Light* (EBL). The cross section describing the process become significant for scatterings on CMB photons starting from a γ-ray energy of approximately 100 TeV [5].

The presence of significant contamination from nearby objects creates many problems for the direct measurement of the EBL. Different models have been developed, but the intensity and shape of the EBL spectrum is still variable in a wide range due to different modeling approaches and uncertainties in model parameters [29, 30].

1.4 NEUTRINOS

The existence of CRs sources motivated neutrinos as probe of cosmic accelerators. Since neutrinos have a much lower interaction cross section than photons, the detection of neutrinos of astrophysical origin turns out to be much more challenging than γ-rays. Together with photons, neutrinos share the advantage of not being deflected by magnetic fields, and more over they do not suffer relevant absorption phenomena thanks to their very small cross section. Neutrinos are also of fundamental importance to unequivocally investigate the hadronic processes that take place inside CRs sources.

The *astrophysical beam dump* process used to explain γ-ray production through the decay of neutral pions can also be used to explain the production of high-energy neutrinos. Together with π^0, π^+ and π^- are produced in approximately the same number. While their neutral counterpart decays in two photons, the processes connected to charged pions decay are

$$\pi^+ \longrightarrow \mu^+\nu_\mu \tag{1.11}$$

$$\pi^- \longrightarrow \mu^-\bar{\nu}_\mu. \tag{1.12}$$

$$\tag{1.13}$$

The muons produced by pion decays also decay in the following:

$$\mu^+ \longrightarrow e^+\nu_e\bar{\nu}_\mu \tag{1.14}$$

$$\mu^- \longrightarrow e^-\bar{\nu}_e\nu_\mu. \tag{1.15}$$

$$\tag{1.16}$$

For detection purpouses, neutrinos and anti-neutrinos are equivalent, from now on we will indicate both as *neutrinos*. The final particle balance of these decay processes is a ratio of $1/3$ between γ-rays and neutrinos. The final ration between photons and neutrinos in *photoproduction* processes is also

$$\frac{L_\nu}{L_\gamma} = \frac{1}{3}. \tag{1.17}$$

Concerning the flavour of neutrinos, a ratio between ν_e, ν_μ and ν_τ of $2:1:0$ at the source will be diluted to a $1:1:1$ ratio at detection thanks to oscillation during the very long propagation path [4].

2

Source Candidates

The first evidence of neutrino emission in coincidence with a γ-ray flare from a blazar sets a milestone for the young field of neutrino astronomy [3]. Nevertheless, the road to reach a state of development similar to the current γ-ray astronomy is still long and challenging. The process of understanding the components of the diffuse astrophysical neutrino flux, identifying its sources and unequivocally connect them to γ-rays and Cosmic Rays is still in its infancy, but the cornerstone of a real multimessenger astronomy has been placed. This chapter will review the theory behind two different putative classes of sources: Active Galactic Nuclei (AGN) of the *BL Lac* type and AGN presenting strong relativistic outflows.

2.1 Active Galactic Nuclei

Active Galactic Nuclei are strong astrophyisical sources that emit radiation over many orders of magnitude in frequency, covering nearly the full electromagnetic spectrum. Their name is motivated by the presence of an active nucleus that compared to standard galaxies is able to outshine the stellar material. This nucleus is constituted by a spinning *Supermassive Black Hole* (SMBH), with a mass larger than 10^6 Solar Masses and an extension between 10^{-7} and 10^{-3} pc. AGN are powered by the gravitational energy that is released by material falling into the central SMBH. The mass of the black hole is usually proportional to the luminosity of the AGN, making heavier black holes easier to discover. Another important quantity for the SMBH description is its spin, which is thought to influence the radiative efficiency of the accretion disk and the emission of relativistic jets. The accretion material is located in a thin disk surrounding the nucleus, extending to distances up to 1 pc. The accretion flow is of fundamental importance in the description of the AGN, its rate is infact connected to the luminosity of the disk and its internal structure may influence the launching of relativistic jets and explain the variability that is observed in every AGN. Additional clouds of material are usually located in the region between 1 and 10 pc in a typical toroidal shape. The internal structure of the torus remains uncertain, but it is thougt to be extremely variable and change from a diffuse and homogeneus distribution to an assemblement of clumpy clouds. These differences are important in the description of the possible obscuration of the SMBH and the accretion disk. The possible presence of Doppler boosted radiation in the form of jets and their orientation have a major role in AGN classification, and their emission carachteristic are described in Section 2.1.2. The role of the host galaxy is of increasing importance with the decrease of the AGN luminosity, it infact mostly produces contamination and obscuration effects, but it is also taken into consideration as an additional source of fuel for the black hole accretion [31].

AGN have many different characteristics that make them very interesting candidates in the search for CRs sources. They are the most powerful non-explosive objects in the known Universe, with very high luminosities, up to $L_{Bol} = 10^{48}$ erg s^{-1}. This feature makes it possible to observe incredibly far AGN, the furthest of them being measured at $z = 7.1$ [32]. Their luminosity function presents a strong evolution, with a peak at $z \sim 2$. The emission region have a size of the order of 10^{10} km, which can be considered small for the energies of observed emission, this implies the presence of very high energy densities [33, 34].

The SED of AGN covers the full electromagnetic spectrum, showing different features that can be connected to different physical processes happening in different regions of the object. These features are commonly used to classify AGN in many different classes that most of the time focus on a specific property in a specific window of the energy spectrum. This approach can cause selection effects and biases that can be prevented with a broad multiwavelength study of the objects, see [31] for more details. Starting from the lower energy bands, it is possible to explore the different aspects that characterize AGN and describe the physical processes that are believed to produce them. The main features of the spectrum are illustrated in Figure 2.1.

The *radio* energy band is dominated by syncrotron emission of accelerated charged particles that can usually be parametrized with a power law. The coefficient α of the power law can be used to distinguish steep ($\alpha \leq 0.5$) from flat ($\alpha \geq 0.5$) [35–37] radio spectra: a steep spectrum usually corresponds to extended sources, while a flat

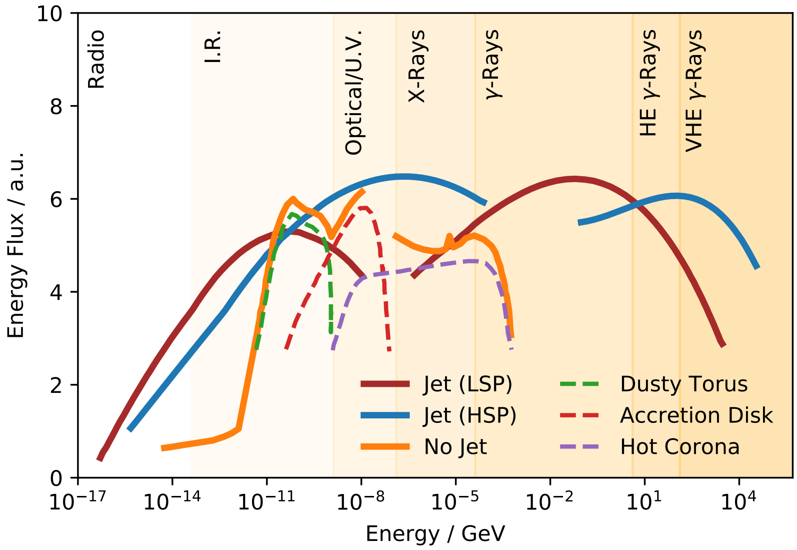

Figure 2.1: Illustration of different AGN Spectral Energy Distributions (SEDs). The non-jetted SED is based on observation of quasars ([Elvis et al., 1994; Richards et al., 2006a]). The jetted high synchrotron peaked (HSP) distribution is based on the SED of the BL Lac *Mrk 421*. The jetted low synchrotron peaked distribution (LSP) is based on the SED of *3C 454.3*. Image adapted from [31]

spectrum is characteristic of more compact objects. Among the compact objects, the ones that host relativistic jets oriented at an angle smaller than 20° with respect to the line of sight are called *blazars* [38, 39]. Blazars are the dominating class of sources in the bright radio energy band.

It is now commonly accepted that the dusty torus surrounding the accretion disk is responsible of the features of in the *infrared* (IR) band of the energy spectrum of the object. The clouds of material that constitute the torus can interact with the radiation originated in the accretion region, shifting it to lower energies in order to dominate the IR band [40]. The details of the spectrum depend on the amount of obscuration that the dusty torus provides over the inner accretion region [41].

The accretion disk surrounding the SMBH generates radiation in a continuum that goes from *optical* wavelengths, to *ultra violet*, to *X-rays* [42]. More in detail, when the AGN orientation permits the direct observation of its inner region, it is possible to distinguish a region with broad emission lines (BLR), typical of gas moving at a velocity of a few thousands of kilometers per second [43]. This region is believed to be located between the central SMBH and the inner surface of the dusty torus. Gas with slightly lower velocity ($300 - 100 \mathrm{km/s}$) is instead present in the narrow emission lines region (NLR), located below and on top of the accretion disk. The two subclasses of blazars can be identified by features in the optical wavelengths. *Flat Spectrum Radio Quasars* (FSRQ) present strong broad emission lines, while *BL Lacs* are often completely featurless, displaying weak emission lines at most and absorption features in some cases. These differences can be observed in Figure 2.2.

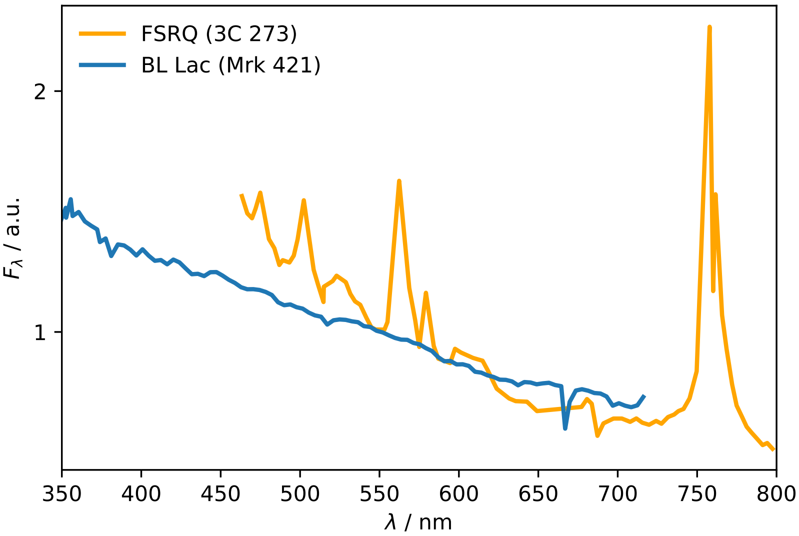

Figure 2.2: Comparison between the spectra at optical wavelengths of a *BL Lac* (*Mrk 421*, blue line) and a FSRQ (*3C 273*, orange line). Data from [44, 45].

Current measurements show that every AGN type presents some form of emission in the X-ray wavelength. This observation is caused both by the fact that X-ray photons, especially at higher energies, can penetrate through large quantities of matter and by the fact that X-ray emitting processes from the host galaxy are typically different orders of magnitude fainter than the ones observed in the AGN. These features make the X-ray surveys the most complete in terms of AGN identification in the universe [46]. The specifics of the energy spectrum are tightly related to the inclination of the objects with respect to the line of sigths and to the geometry of the internal components of the AGN. It is believed that the main contributing process is the inverse Compton scattering of photons from the accretion disk and their interaction with the atmosphere above and below the disk (called *Corona*) and with the dusty torus [47]. In AGN where jets are present, their contribution to the X-ray component of the spectrum can be significant.

AGN without a jet do not seem to reach energies high enough to populate the spectrum at the γ-ray wavelengths [48]. Only blazars are detected in this energy band, making them the dominand contributors at the highest photon energies. Their extremely powerful radiation originates in the relativistic jets pointing directly to the observer [38].

2.1.1 Blazars

As introduced in Section 2.1, Blazars are AGN that present at least one jet that is collinear to the line of sight. Despite being a minority among AGN, blazars dominate the γ-ray sky and the bright-radio wavelength. The SED of blazars spans over the full electromagnetic spectrum, covering many orders of magnitude in energy with a very characteristic double humped spectrum (see Figure 2.1). The first hump is universally accepted to be produced by synchrotron emission from electrons. The peak of the hump takes the name of ν-peak, and it is usually located in the I.R., Optical/U.V. or X-ray energy band. The position of the peak is used to classify these objects: sources with a ν-peak situated at frequencies smaller than 10^{14} Hz are called LSP (*Low Synchroton Peaked*), sources with a ν-peak situated between 10^{14} and 10^{15} Hz are ISP (*Intermediate Synchroton Peaked*), and finally sources with a ν-peak larger than 10^{15} Hz are HSP (*High Synchroton Peaked*) [49, 50]. The physical process behind the second hump is still unknown, with the candidates being a pure leptonic origin [51], a pure hadronic one [52], or a mixture of the two (see Section 1.3). In a leptonic scenario, the hump is produced by inverse Compton scattering of the electrons accelerated in the jet with their own synchrotron emission. The hadronic scenario instead has synchrotron emission from protons as the source of this spectral feature. This latter case is interesting for multimessenger studies because it will imply that blazars are also sources of high energy neutrinos and CRs [53, 54].

While the two classes of blazars (BL Lacs and FSRQs) are classified using features of their spectrum at optical wavelengths, they present significant differences also in the highest energy part of the SED. FSRQs mostly show a steep γ-ray energy flux in the HE energy band, dropping off before the VHE band in most of the cases. BL Lacs present a more flat spectrum at HE, with the cutoff being at VHE energies. Both classes of blazars are found to be highly variable objects, with flares being observed at different wavelengths (usually X-rays and γ-rays). The time scales of the flares are also very different and they can cover from short (minutes to hours) to very long (months) time intervals. The duration of the flares can provide useful information on the size of the environment in which the particle acceleration takes place. The trigger mechanisms behind the flares are still under study [55–57].

Thanks to detailed studies on blazar luminosity functions, their cosmological evolution and their number densities, together with the latest models of EBL absorption, it has been possible to estimate the contribution of both BL Lacs and FSRQs to the *Extragalactic γ-ray Background* (EGB). It has been calculated that blazars consitute significant part of the whole EGB [58]. Especially above 100 GeV, HSP objects are shown to be the dominant source candidate, leaving very small to no room for other species of sources (see Figure 2.3).

2.1.2 The Jet

The role of a collimated outflow of relativistic particles under the form of a jet is of fundamental importance in the description of the fluxes of γ-rays, neutrinos and eventually UHECR. Current telescopes are still challenged by the observation of the details of the jet and can not yet provide a clear confirmation to the mechanism of the jet production and to its composition. The accretion of the disk material into the black hole with the corresponding release of gravitational energy is thought to be the main engine powering the jet emission. Particles in the jet will experience a relativistic boost up to a Lorentz factor of 50, exhibiting a further beaming effect in the case of jets pointing towards the observer, even producing cases of apparent superluminal motion. The particles of the bulk of the jet will encounter various photon fields on their way to the observer, providing different ways of explaining the fluxes measured at Earth [59].

If the energies of the accelerated protons are not above photoproduction threshold, the main component of the observed flux will be produced by accelerated electrons and pairs interacting with photons fields at lower energies. These fields may have various different origins: radiation from the accretion disk, the corona or the dusty torus, or they could be a feature of the jet itself and be produced by an outer layer of slow moving material interacting with a boosted spine of ultrarelativistic plasma in the inner region of the jet. When protons are accelerated at high enough energies, their synchrotron radiation together with the radiation produced by their secondary muons dominates the second hump of the blazar SED [60].

The complex feature of the SED and especially the time variability in the emission of the jets are very difficult to explain with elementary models which describe the emission region as spherical and uniform. More advanced models picture the jet as a set of different cylindrical layers [61], or a set of shells ejected at different speed that collide with each other [56]. Such models with multiple zones of emission are currently under study, and offer promising results [62].

2.1.3 The Cumulative Neutrino Background

Decades of experience in γ-ray astronomy made possible to develop advanced models that are of fundamental importance in explaining the measured spectral data points from various astrophysical objects. Neutrino astronomy is comparatively in its infancy, but it can learn significatively from the techniques that have been adopted before in the γ-ray branch.

A detailed modeling of the blazar SED can infact convey important information on the expected neutrino fluxes and possibly guide the existing neutrino experiments towards the discovery and characterization of neutrino sources. As an example, as showed in [63], an expected flux of neutrinos at Earth can be estimated starting from the modeling of HBL objects that have been spatially and energetically correlated with single High Energy Starting Event (HESE) measured by the IceCube Neutrino Detector. The physical assumption is a standard leptohadronic [64] model that is parametrized by a proportionality factor between the neutrino flux and the γ-ray flux. The flux of the single objects can then be inserted in a generalized model able to reproduce the statistical properties of blazars in different energy bands (the *Blazar Simplified View* [65]), and after integration an expected flux of neutrino can be calculated. As showed in Figure 2.3, in parallel to what it is believed to happen in γ-rays, BL Lacs could explain the whole neutrino flux above a certain energy (100 GeV for γ-rays, 0.5 PeV for neutrinos). However, it is important to note that recent analyses on the neutrino data constrain the maximum blazar contribution to the measured neutrino flux to $\sim 30\%$ (see chapter 4).

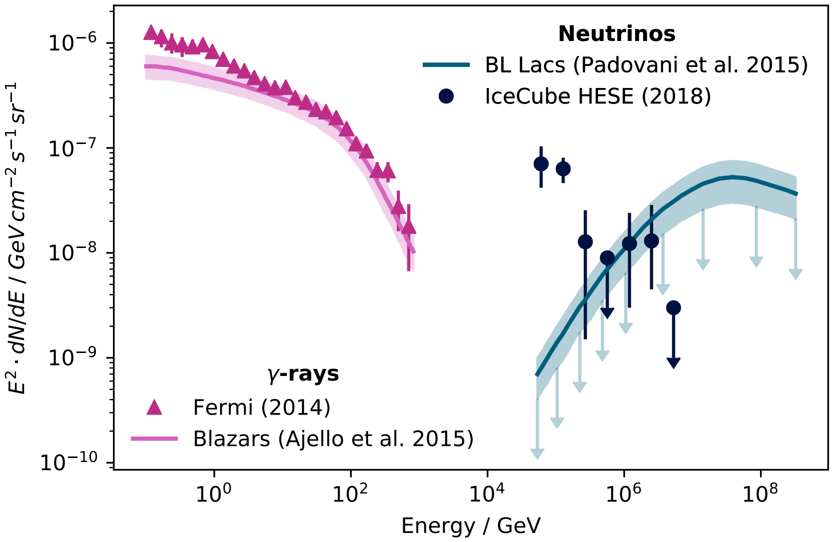

Figure 2.3: The γ-ray and neutrino extragalactic background predicted by [58] (pink band) and [63] (cyan band). The points represent the data measured by the experiments: *Fermi*-LAT (purple triangles) and IceCube (blue dots).

2.2 AGN OUTFLOWS

Even though the contribution of blazars to the Extragalactic γ-ray Background (EGB) is of primary importance at high energies, they can account for $\sim 50\%$ of the flux at energies lower than 10 GeV [58, 66]. This energy band sees the emergence of other possible contributing classes of sources, and among the more established populations of radio galaxies and star-forming galaxies, recent models predict a significant contribution from AGN without relativistic jets. Several observations have shown that these objects are capable of emitting wide-angle, non-collimated *outflows* of high velocity material [67–69].

The large scale outflows are generated by the interaction of soft relativistic winds ejected from the inner constituents of the AGN with the galactic material. These winds are believed to be able to sweep material out of the galaxies and in extreme cases to even stop star formation [70]. The shock interaction of the ionized particles accelerated by the winds and the interstellar material (ISM) can originate non-thermal emission in γ-rays and possibly neutrinos and UHECR.

2.2.1 Dynamics of the winds

The process of particle acceleration that takes place in AGN outflows is thought to be similar to the one used to describe shock acceleration due to supernovae explosion. Once theorized to explain the mechanism at the origin of the death of certain galaxies, these outflows are now commonly observed [71, 72] in objects at a wide range of redshift, with outflows measured up to velocities of $0.1 - 0.3$c [73, 74].

The constituents of the winds are ionized and neutral nuclei and protons, likely belonging to the accretion disk of the AGN. They are accelerated through radiation pressure by the radiation fields surrounding the central SMBH, and can cover distances that go from 10^{-3} to 10^{3} parsec [75]. The interaction of the AGN winds with the ISM can be modelled in a similar way as the stellar winds interacting with ISM gas. The particles accelerated by the winds drive shock fronts in outward direction. The shock contributes to accelerate and sweep the ISM particles. At the same time an inward directed front travels backwards, decelerating the wind itself. In *momentum* driven shocks, most of the energy of the wind is dissipated in form of radiation, and only its momentum is transferred into the ISM. In winds with the right properties, the cooling does not happen efficiently, causing all the energy of the gas to be shared with the target material, inducing an adiabatic expansion able to push the ISM even further away. These latter types of shocks are called *energy* driven [76]. Collision between accelerated particles are able to generate γ-rays, neutrinos and more in general CR as described in chapter 1.

2.2.2 Outflow contribution to the three messenger fluxes

Different prediction on the fluxes of particles produced by AGN outflowsare currently available for all three of the astrophysical messengers. Three models concern both γ-rays and neutrinos Wang et al. [77, 78], Lamastra et al. [76], Liu et al.[79] and only one goes as far to predict a possible outflow contribution to the UHECR flux (Wang et al.) [80].

The first step of each model is to describe the hydrodynamics of the outflow with equations that provide a description for the evolution of the masses, pressures and dimensions of the different shells that constitute the shock. A population of accelerated protons is then injected into this environment with a chosen power law energy distribution and its dominating interactions are taken into consideration to provide the fluxes of particles exiting the galaxy. Inelastic scattering between protons generates neutral and charged pions, that can decay in γ-ray photons, electrons and neutrinos. Accelerated electrons can further contribute to the γ-ray flux. The single source flux is then integrated over the entire AGN population at all bolometric luminosities and redshifts. Further extragalactic effects like EBL absorption are finally applied to provide the fluxes measured at Earth.

Figure 2.4 shows the fluxes predicted by Wang et al., Lamastra et al. and Liu et al. The first one is the model that seems to better describe the data: by fitting the γ-rays to the residual (the fraction of the flux not attributable to other sources) of the EGB measured by the *Fermi*-LAT experiment [66], it is possible to reproduce the fluxes observed in both astrophysical neutrinos and UHECR without further parameter tuning. The addition of the contribution by electrons and the integration using a dedicated Semi Analytical Model of hierarchical galaxy formation by Lamastra et al. produces similar results, with the worrying feature of overshooting the EGB measured by Fermi in the few GeV energy window. The latest model by Liu et al. introduces further complexity and provides the most stringent results for the outflow contribution to the three astropysical messenger fluxes. The differences between the two former models and the latter are multiple: at first approximation, Wang et al. and Lamastra et al. take a R^{-2} approximation for proton density in the galaxy down to the smallest radii, introducing an artificial high density and scattering efficiency. Liu et al. model the inner core of the galaxy as uniform, generating a flatter spectrum at energies smaller than 10 GeV. Their work also include proton cooling effects due to inelastic collisions and the adiabatic expansion of the gas. Additionaly, it is important to notice that the fluxes produced by the expansion of the shock through the galactic disk and the outer galactic halo are significantly different. Since the time spent by the shock front in the halo is much larger than the one spent in the disk, and the average life of an AGN is shorter than the age of the galaxy, it is appropriate to average the γ-ray and neutrino luminosity over the entire evolution, and then integrate over redshifts, as done both in Wang et al. and Liu et al. Finally it is important to point out that the EBL absorption model used in Wang et al. and Lamastra et al. ([30]) has been proven outdated, a more recent model ([29]) is used by Liu et al.

The optimistic conclusion that can be taken from these studies, is that AGN outflows can contribute up to $\sim 30\%$ to the EGB flux without violating other independent upper limits. The contribution to the neutrino diffuse flux is limited to $\sim 20\%$

in the energy range 1 — 100 TeV, but the fraction can become larger at higher energies. For what it concerns the UHECR flux, despite a connection to AGN outflows is very intriguing, the studies are still too few to provide a clear estimate on the possible contribution.

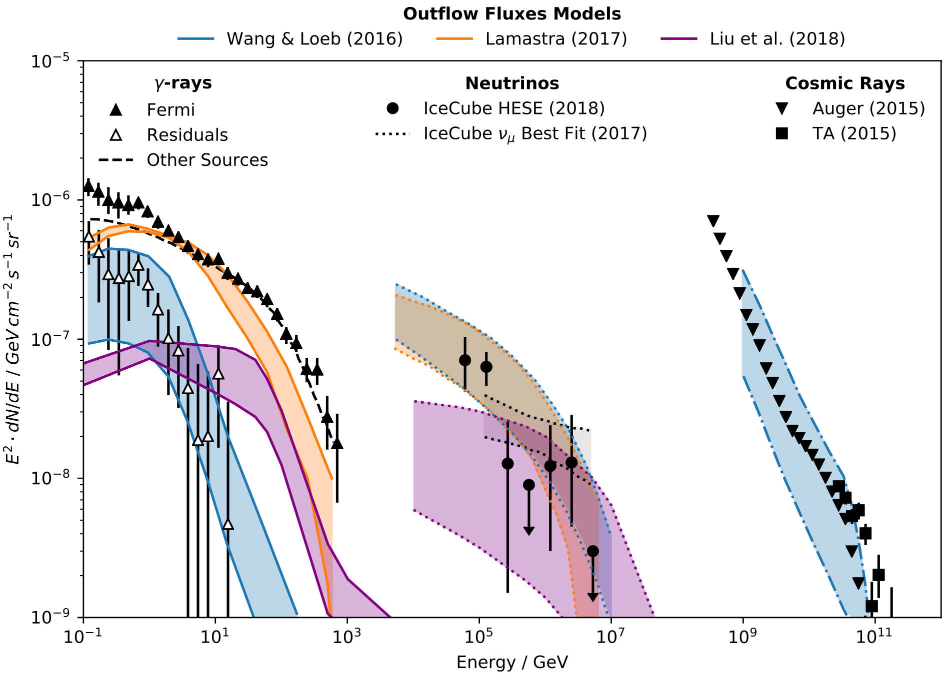

Figure 2.4: From left to right, using filled markers, measured data is shown for the cumulative EGB (upward triangles) [66], the diffuse neutrino flux measured in two different topologies (grey shaded area and circles) [2, 81] see chapter 3, and UHECR flux (downward triangles and squares) [82, 83]. For the EGB, the contribution from sources other than AGN outflows, *i.e.* blazars, radio galaxies and star-forming galaxies is plotted using a dashed black line. The residual flux is plotted using with upward triangles. The fluxes predicted by [80] are showed as a blue shaded area (upper/lower limits for a proton injection spectrum of $\Gamma = 2.3$ and $\Gamma = 2.4$). The fluxes predicted by [76] are showed as an orange shaded area (upper/lower limits for a proton injection spectrum of $\Gamma = 2.3$ and $\Gamma = 2.2$). The fluxes predicted by [79] are showed as a purple shaded area (upper/lower limits for a proton injection spectrum of $\Gamma = 2.1$ and $\Gamma = 2.3$). Figure extrapolated from [80].

3

The IceCube Detector and the Astrophysical Neutrino Flux

In the first part of this chapter the principles of neutrino detection using a large volume of trasparent medium will be reviewed. The second part will provide more detailed information on the IceCube Neutrino Observatory at the South Pole. In the third part the current status of the searches for pointlike neutrino sources will be presented. The last part will contain the description and the results of an analysis performed to look for small scale anisotropies in the neutrino sky.

3.1 Neutrino Detection

The first proposal about using large volumes of water to detect neutrinos was developed independently by Greisen, Markov, and Reines in 1960 [84, 85]. The basic idea is to instrument an array of light detectors inside a large volume of a pure, transparent medium. The easiest way to obtain such a large quantity of material with those characteristics is to make use of natural resources like deep sea water or polar ice. The material will provide first of all the nucleons that can serve as a target for the neutrino interaction, but in addition to that it can allow the propagation of the Cherenkov photons emitted by the relativistic secondary particles. Since the instrumented volume will be placed as deep as possible, all the water or ice between the detector and the surface can additionally serve as shielding from the large background of particles generated by CR interacting with the atmosphere.

Neutrinos interact with nucleons only via weak interaction. Two different interactions are possible: charged current (CC) interaction,

$$\nu_\ell + N \rightarrow \ell + \text{hadrons}, \tag{3.1}$$

with ℓ being electron, muon or tau leptons, and neutral current (NC) interaction,

$$\nu_\ell + N \rightarrow \nu_\ell + \text{hadrons}. \tag{3.2}$$

The cross secton of the interaction (see Figure 3.1) is proportional to the energy of the neutrino up to 10^4 GeV and starts to flattens above this energy. Neutrinos can additionally interact with electrons, but this process is suppressed by its very small cross section. At a neutrino energy of 6.3 PeV, the so called Glashow Resonance can take place:

$$\bar{\nu}_e + e^- \rightarrow W^-, \tag{3.3}$$

which manifests itself with a peak in the cross section.

The neutrino interaction length, which is inversely proportional to the cross section, is several order of magnitude larger than the cross section of high energy photons, allowing the observer to reach with neutrinos part of the universe than would be too far to be explored with γ-rays.

The hadronic and electromagnetic cascade that develops after the neutrino interaction is usually too compact to be resolved in a large, but sparsely instrumented detector. This is the reason why all NC interactions and the electron CC interactions are only measured as spherical shaped deposit of energies. These types of events are usually called *Showers*. The reconstruction of the arrival direction of the primary neutrino is very difficult in these cases, but since all the energy is usually deposited inside the instrumented volume, the energy resolution is good enough to permit detailed calorimetric measurements.

CC interactions where a high energetic muon is produced are usually called *Tracks*. Muons can infact travel for very long distances through matter before decaying (the range of a 100 TeV muon is larger than 10 km). When a muon traverses the detector, a typical cone-shaped track of Cherenkov photons is emitted along its path. A long track gives a long lever arm to reconstruct the directional information of the primary neutrino with an angular resolution better than 1° [86]. The directional separation due to kinematics effects between the primary neutrino and the detected muon is negligible at high energies. The energy of these events is on the other hand difficult to reconstruct, because if the track is not completely contained inside the detector, the total energy deposit can be only estimated through simulation.

Tau neutrino CC interactions usually leave a shower-like signature inside the detector. The τ particle produced will infact decay too quickly to be resolved from the cascade that is left by the primary interaction. At energies larger than 1 PeV, the τ can travel enough distance to leave a track-like signature in the detector, before decaying causing a second hadronic cascade separated from the first one. These special types of events are named *Double Bangs*.

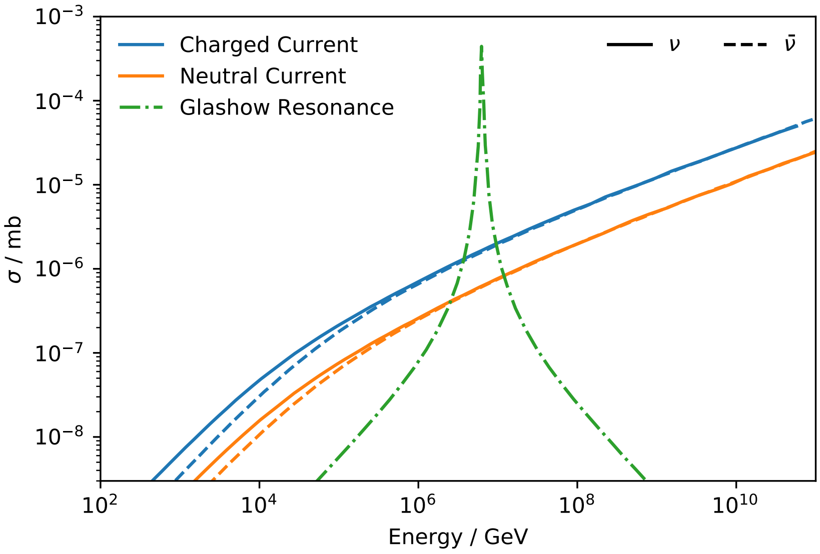

Figure 3.1: Cross sections of neutrino-nucleon scattering via CC and NC interactions and of neutrino-electron scattering via CC interactions of electron anti-neutrinos (data from [87, 88]).

3.2 ICECUBE DETECTOR

The IceCube Neutrino Observatory [89] is located at the Scott-Amundsen South Pole Station, at the Geographical South Pole. The ice cap is almost three kilometers thick at this location, and it is the result of snowfall accumulation over many centuries. This layering process traps air and impurities inside the ice, which affect on ice properties like scattering and absorption length for Cherenkov photons travelling through the medium. IceCube precursor, AMANDA, provided the first measurements of these ice properties [90]. Starting from depths of 1400 meters, the ice substains an enormous amount of pressure that renders its crystalline structure optimal to measure photons at the wavelengths between 200 and 400 nm.

From 2005 to 2010, a total of 86 strings have been deployed inside the antartic ice using a dedicated system for hot water pressure drilling. The strings are arranged in an esagonal footprint on a triangular grid with a spacing of ~ 125 m between each other. They consist of a single cable containing twisted copper-wire pairs. 78 strings are equipped with 60 Digital Optical Modules (DOMs), which are positioned at equally spaced lengths of 17m between depths of 1405 and 2450 m. This part of the detector is called *IceCube*. The remaining 8 strings constitute the *DeepCore* subdetector. They are deployed in the center of the array with a denser spacing (72 m of average length). DOMs are placed vertically closer to each other, at depths starting from 1750 m, avoiding the region between 2000 and 2100 m. This layer of ice, the *Dust Layer*, presents a significantly higher level of impurities, therefore reducing the scattering and absorption lengths of the ice. The full detector instruments $1\mathrm{km}^3$ of ice with a total of 5160 DOMs. On the surface of the ice, approximately at the same location of the In-Ice Array strings, 162 ice-filled tanks equipped with DOMs arranged in 81 stations constitute the cosmic-ray shower array denominated *IceTop*. The IceCube Laboratory (ICL) is positioned at the center of the array and it is the central operations building of the detector. The cables from the strings and from the stations are connected to a server room inside the building where all the computers performing the data acquisition and the data filtering are located. The structure of the full detector is depicted in Figure 3.2.

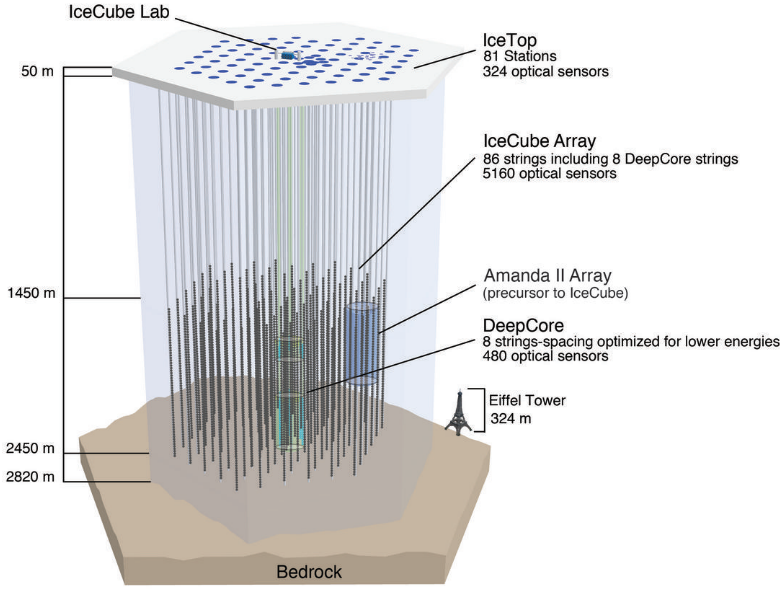

Figure 3.2: The IceCube detector at the South Pole. Each black dot in the ice represents a DOM of IceCube. The DeepCore sub-array is highlighted in green and the positions of the IceTop tanks on the surface are marked in blue. AMANDA, the precursor of IceCube is also highlighted in blue inside the ice. Figure credits to the IceCube Collaboration.

The DOMs are the fundamental unit of the IceCube detector, performing both tasks of light detection and data acquisition. They consist of a downward-facing photomultiplier (PMT) and the corresponding circuit board, which are housed inside a glass sphere of 33 cm diameter and a thickness of 13 mm. The PMTs used in Deep-

Core DOMs have a higher quantum efficiency than the standard IceCube DOM. Each DOM is additionally equipped with a LED flasher board that can be used for calibration purposes. The internal components of a DOM are depicted in Figure 3.3.

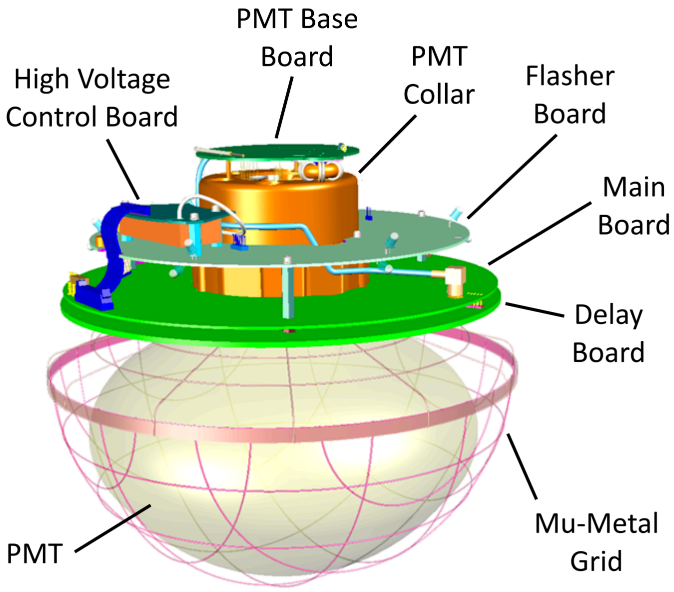

Figure 3.3: The internal components of the glass sphere of a DOM are here depicted. The labels give a description of each part. Figure credits to the IceCube Collaboration.

When a photon hits one of the PMTs, and triggers a response that is above 0.25 times the single photo electron threshold, the DOM registers a *hit*, which consists of a timestamp and a charge measurement over 6.4µs. Two digitizers, an Analog Transient Waveform Digitizer (ATWD) and a Fast Analog to Digital Converter (FADC), are installed on the mainboard of every DOM to ensure data taking over different time ranges. Two ATWDs are present on each DOM to reduce dead time. Multiple channels are set up with different gains on the ATWD to provide a wider dynamic range. When *hits* are isolated, they are called *Soft Local Coincidences* (SLCs), and only three sample points from the FADC are digitized. If there is more than one DOM registering a hit in an array of four neighbouring DOMs on the same string, the so called *Hard Local Coincidence* (HLC) condition is fulfilled. In this case the full digitized waveform is stored and sent to the surface. Data is saved in the DOM in blocks of $\sim 1\,\mathrm{s}$ before being transferred up the chain of processing. Before being process by the Data Aquisition (DAQ) system in the ICL, each hit goes through the *DOMHub*, which is a computer that manages all the DOMs of a single string.

SLCs are mostly used to add information in order to increase the accuracy in energy and directional reconstruction of events when additional HLCs are present, or to veto events where a contribution from an atmospheric shower is present. Isolated SLCs are usually generated by dark noise of the PMTs due to radioactivity inside the glass sphere of the DOM and need to be cleaned from the recorded data. The standard trigger, called Simple Multiplicity Trigger (SMT), checks for multiple HLCs inside sliding a time window of $5\,\mu\mathrm{s}$. All hits recorded in a window of $-4\,\mu\mathrm{s}$ to $+6\,\mu\mathrm{s}$ around a trigger make up an *Event*. Multiple triggers inside the same time window are merged together. An example of the rate of the SMT8 trigger, in which eight HLCs are requested inside the time window, is shown in Figure 3.4.

Real time DAQ is necessary to process the raw data stream of the detector and it reduces it to a size that fits the limited satellite bandwith allowed at the South Pole. For this reason the digitized waveforms are firstly converted into series of *pulses*: a combination of amplitude, width and leading edge time that describe the deposited charge. Pulses are then further cleaned by removing isolated hits which are not causally connected to the others. Elementary but computationally inexpensive reconstructions are then performed on the cleaned pulses belonging to an event. Different filters can at this point be applied *online*, in order to select the interesting data to be transferred to the northern hemisphere. The *Muon Filter* is the most relevant filter when trying to correlate the incoming direction of a neutrino with any astrophysical object. This filter is responsible for the selection of good reconstructed track-like events. The filter treats upgoing tracks with zenith angles larger than 85° and downgoing tracks differently. The former are selected based on the quality of the reconstruction, the latter have an additional cut on the deposited enegy, zenith angle dependent, applied in order to reduce the atmospheric background and tuned to match the rate of upgoing events (34Hz on average). After the filtering, events are furtherly processed *offline* with more complex methods, to final level, which is used by the physics analyses.

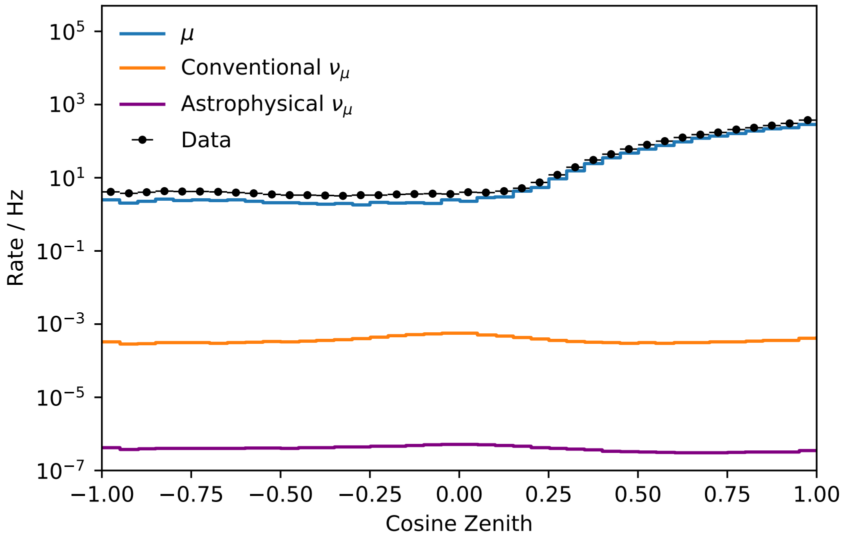

Figure 3.4: Rate of the Simple Multiplicity Trigger with eight HLCs inside the time window (SMT8) as a function of the cosine zenith angle of the reconstructed direction of the event. Events with $\cos(\theta) < 0$ are downgoing, originating from the northern hemisphere. Atmospheric muons dominate both the southern and the northern skies.

3.3 THE EVENT RECONSTRUCTION

A significant number of different algorithms have been developed over the years to make the best use of the information measured by the DOMs and provide an accurate measurement of different physical variables of the neutrino events. Two broad categories of reconstructions are relevant in the case of track-like events originated from high-energy muons: the tracing of the direction of the orimary neutrino, and the estimation of its energy.

3.3.1 DIRECTIONAL RECONSTRUCTION

The muon produced in a neutrino interaction is emitted at an angle $\Delta\theta$ with respect to the primary particle direction. This offset is nevertheless decreasing with energy (see Eq. 3.4)

$$\Delta\theta = 0.7^{\circ} \left(\frac{E}{\mathrm{TeV}}\right)^{-0.7}, \tag{3.4}$$

and becomes negligible for the high-energy events that are employed in neutrino astronomy analyses.

The reconstruction process uses likelihood maximization techniques [86] and starts with simple and inexpensive first-guess algorithms that are subsequentially feeded as a seed to more complex and detailed reconstructions. The easiest approach, named *LineFit*, assumes light travelling at constant speed and in straight lines through the ice. The time stamps of the hits at each DOM are used to identify the most likely direction of the particle that generated them. Time residuals, namely the differences between the measured times of the hits and the expected times from geometrical propagation of the light without scattering, can be analytically modeled by the Pandel function [91]. An experimental modeling of the ice has been a continuous effort during the years of detector operation. The different properties of the ice layers, together with the angular acceptance of the modules have been measured thanks to dedicated calibration runs that make use of the LED flashers embedded in the digital board of each DOM. Monte Carlo simulation of the photon propagation obtained from muon tracks of infinite length have been tabulated. These numerical tables are subsequently interpolated with multidimensional splines. The median angular resolution obtained from different reconstruction algorithms is shown in Figure 3.5 in comparison with the angular difference between primary neutrino and secondary muon due to kinematics.

The accuracy of the angular reconstruction can be estimated in different methods that go from a generic *point spread function* distribution as a function of energy for the whole sample to a specific event-by-event error estimation. The latter is the standard used by IceCube neutrino astronomy analyses. The most detailed error estimation for a single event can be obtained by Monte Carlo simulation of neutrino events with similar properties. Analyses using event samples with high statistics suffer from the computational bottleneck that this approach creates and have to accept an alternative approach that is slightly less precise. In these cases, the likelihood parameter space is scanned and a bi-dimensional parabola is fitted around the maximum. A mean square is then computed using the two axis of the parabola, obtaining the radius of an area of circular shape which indicates an approximated uncertainty region around the event coordinates. The algorithm here described takes the name of *Paraboloid*. From simulations it is possible to notice an overestimation of the accuracy proportional to energy, this effect is counter balanced by applying an *ad hoc* energy dependent rescaling of the estimated angular error.

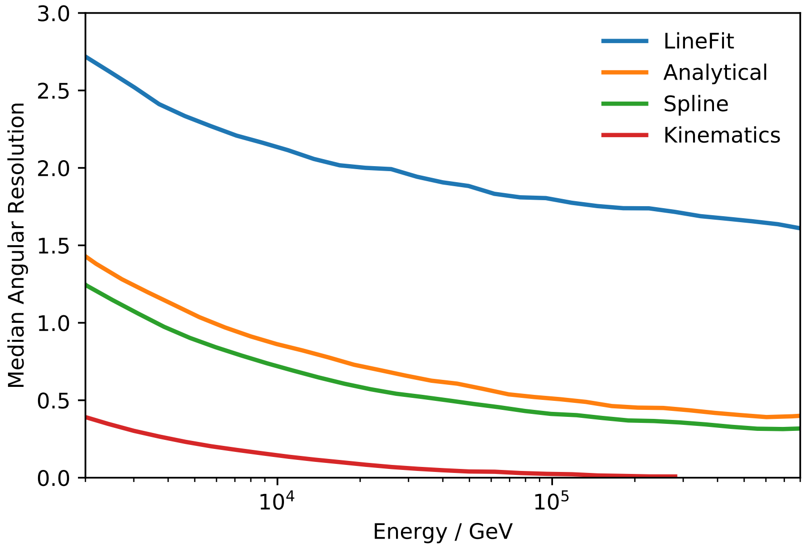

Figure 3.5: Median angular resolution obtained from different reconstruction algorithms (blue, orange and green lines). A comparison with the angular difference between primary neutrino and secondary muon is also shown in purple.

3.3.2 Energy Measurement

In the framework of neutrino astronomy, the measurement of the energy deposited by a particle interacting inside the detector volume and the estimation of the energy of the primary particle serve two main purpouses. The first one is the distinction between events of astrophysical origin, the signal, and background events. The second purpose, once a source candidate is found, is to fit its spectrum and extract additional information on the physical processes of the source itself. While the use of the energy for background rejection has been established and standardized over the years, the calculation of the spectrum of a neutrino source in a multimessenger approach has only recently started to be used for tentative source characterization [53].

For the IceCube detector, energy reconstruction of events that lie completely inside the detector, *i.e.* cascades, is easier and more precise than for track-like events, which only deposit part of their energy inside the instrumented volume [92]. The mean energy loss of a muon inside the ice is usually parametrized as

$$-\frac{dE}{dx} = a(E) + b(E) \cdot E, \tag{3.5}$$

where the term $a(E)$ corresponds mainly to ionization losses usually described by the *Bethe-Bloch* formula. The second term becomes dominant at higher energies and describes radiative processes that are extremly variable in amount of energy deposited and characterized by small cross-sections, usually defined as *stochastical* energy losses. Energy losses due to Cherenkov radiation are negligible.

The amount of light measured by the PMTs is proportional to the energy deposited by the particle, but due to different ice properties in different regions of the detector it is necessary to take the DOM response into account via Monte Carlo simulation. The energy reconstruction algorithms that are used for track-like events try to estimate the number of emitted photons from the number of photons that have been observed. The energy is estimated for subsequent deposits of spherical shape along the reconstructed direction of the particle, in unit steps of 10m. A maximum likelihood approach with the directional information seeded by different reconstruction algorithms is usually chosen to mantain a reasonable computation time, the software that implements is in IceCube is called *MuEX*.

3.4 SIGNAL AND BACKGROUND

While the sources of the astrophysical neutrino flux measured by IceCube remain uncertain, the description of the flux itself is rapidly improving thanks to the stability of the detector. The uptime of the detector is close to 100% and this increases steadily the statistical precision of each analysis. In parallel to the study of the signal, an appropriate description of the background expected is of fundamental importance to the interpretation of the measured data. For the IceCube detector, in the framework of pointlike source searches, the main source of background are muons and neutrinos from the interaction of CRs with the atmosphere.

3.4.1 THE ATMOSPHERIC BACKGROUND

High-energy particles of cosmic origin interact with the molecules of the Earth's atmosphere producing *showers* of secondary particles. The extension and depth of each shower is strongly dependent on the type and energy of the primary particle, but their development through the atmosphere until they reach the surface is similar. The shower can ideally be divided in two parts: one hadronic and one leptonic. The leptonic part consists of electrons and photons, which do not become relevant as background for the IceCube detector. The hadronic part instead, is composed by proton, neutrons, pions, electron neutrinos and kaons. These particles can decay into muon and muon neutrinos. Pions decay following Eq. 1.13, while kaons preferred decays involving neutrino production are [93]:

$$K^+ \rightarrow \mu^+ + \nu_\mu \qquad (63.56 \pm 0.11\%)\,, \tag{3.6}$$

$$K^+ \rightarrow \pi^0 + e^+ + \nu_e \qquad (5.07 \pm 0.04\%)\,, \tag{3.7}$$

$$K^+ \rightarrow \mu^+ + \nu_\mu + \pi^0 \qquad (3.35 \pm 0.03\%)\,. \tag{3.8}$$

The charge conjugate are valid for K^- decays; the percentages represent the branching ratios of each process. The contribution to the atmospheric neutrino flux from different particles changes with energies. At lower energies, the contribution of pions is dominant because the muon produced by pion decay does not have a long enough range to reach the surface and will decay or get absorbed. Starting from neutrino energies of $\sim$ 100 GeV, most muons can reach the surface. They will therefore not contribute to the overall neutrino flux. Kaons become the dominant channel of neutrino production at these energies. At higher energies the neutrino flux is suppressed by the fact that both kaons and pions have a decay length which is larger than the mean free path in the atmosphere. They will then lose energy via interactions and consequently produce less neutrinos. This effect changes the power law coefficient of the so called *conventional* atmospheric neutrino flux, which becomes $\gamma = 3.7$ from the standard primary CR spectrum ($\gamma = 2.7$).

Another component of the atmospheric neutrino flux is predicted to become dominant starting at $\sim 10^6$ GeV. These neutrinos are produced by the decay of heavier mesons containing a charmed quark, *i.e.* D^0 or D^+. These particles decay promptly after production (from which the name *prompt* neutrino flux originates), mantaining an harder spectrum closer to the primary CR if compared to the conventional flux. While the conventional flux has been measured in detail by many different experiments, the prompt component of the neutrino flux has still to be unequivocally discovered [94]. IceCube currently puts upper limits at 1.06 times the nominal value [95].

The flavor ratios ($\nu_e : \nu_\mu : \nu_\tau$) of these two components are significantly different from each other, and they are furthermore different from the expected ratio of an astrophysical signal [96]. The conventional atmospheric neutrino flux presents an approximate ratio of 1:2:0, while the prompt component has a predicted ratio of 1:1:0.1.

As can be seen in Figure 3.4, the IceCube detector suffers from different backgrounds from the two hemispheres. This is due to the fact that the Earth serves as a shield for particles coming from the northern hemisphere, absorbing the atmospheric muons that would intersect the detector with an upgoing direction. Unfortunately, the Earth is transparent for atmospheric neutrinos, which can reach the detector completely unaffected by its presence. The downgoing background is even more problematic, because the top layer of ice is not thick enough to be an effective muon absorber. Atmospheric muons are therefore the main source of background coming from the southern hemisphere by many orders of magnitude. In addition to that, down-going muons misreconstructed as up-going are a source of background that can affect also the Northern hemisphere. An additional periodic variation of ~ 0.5 Hz in the overall measured rate can be observed [97]. This is due to seasonal effects that by varying the temperature and density of the atmosphere, increase or reduce the likelihood of pions to decay or lose energy by interaction.

3.4.2 The Diffuse Astrophysical Neutrino Flux

In order to look for neutrinos of astrophysical origin over an overwhelming atmospheric background, the IceCube detector took inspiration from other neutrino undergound experiments and developed a veto technique to discriminate the most likely signal events [98]. This selection consists of events well contained inside the detector, that do not present energy deposits on the outer layers of PMTs. This requirement assures that the neutrino is not accompanied by an atmospheric shower. In addition to that, events are selected above an energy threshold of 60 TeV, at a level where the atmospheric neutrino flux is steeply falling of, revealing the astrophysical signal. The first evidence of an isotropic astrophysical neutrino flux came from this data sample of high-energy starting events (*HESE*) [1, 99] and it is described as

$$\Phi_\nu(E_\nu) = \phi_0 \cdot \left(\frac{E_\nu}{100\mathrm{TeV}}\right)^{-\gamma}, \tag{3.9}$$

where

$$\phi_0 = (2.46 \pm 0.08) \cdot 10^{-18} \mathrm{GeV}^{-1} \mathrm{cm}^{-2} \mathrm{s}^{-1} \mathrm{sr}^{-1} \tag{3.10}$$

$$\gamma = 2.92^{+0.29}_{-0.33}, \tag{3.11}$$

in an energy range that goes from 60 TeV to 10 PeV, assuming a flavor ratio of 1:1:1 (see Figure 3.6).

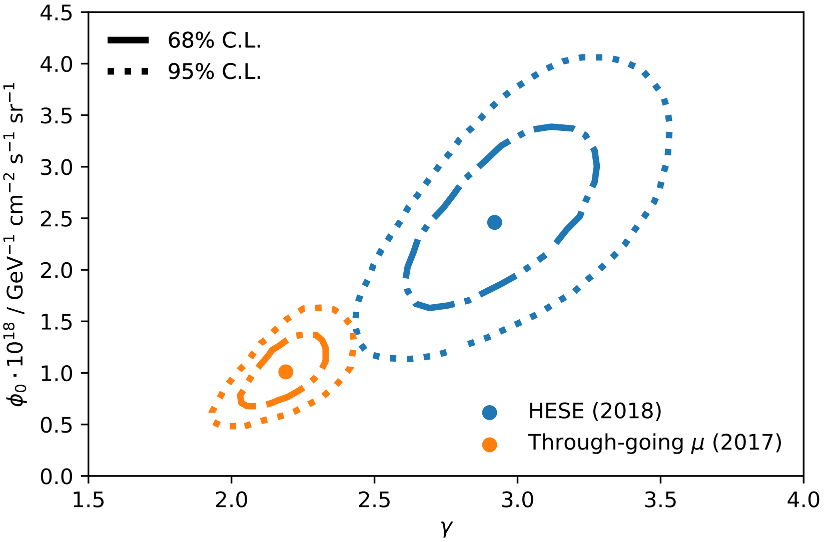

Figure 3.6: Best fit values (dots) and confidence level contours (68% dash-dotted line, 95% dotted line) of the astrophysical neutrino flux normalization ϕ_0 and spectral index γ based on an isotropic, unbroken power-law hypothesis. The results on the HESE data sample are shown in blue [1], while the results on the trough-going muon tracks are shown in orange [2].

This measurement has been confirmed by a different and independent analysis performed on a different data sample [2]. The event selection of this analysis focused on up-going muon tracks travelling through the detector volume and likely originated by neutrinos coming from the Northern hemisphere. The energy threshold for this analysis is slightly larger, starting at 100 TeV. The latest results of the analysis are

$$\phi_0 = (1.01^{+0.26}_{-0.23}) \cdot 10^{-18} \mathrm{GeV}^{-1} \mathrm{cm}^{-2} \mathrm{s}^{-1} \mathrm{sr}^{-1} \tag{3.12}$$

$$\gamma = 2.19 \pm 0.10, \tag{3.13}$$

in an energy interval between 120 TeV and 4.8 PeV.

The IceCube detector has measured neutrino events up to PeV energies, thus allowing to calculate upper limits on the neutrino flux at the high energy end of the spectrum, at energies larger than 5 PeV. An event selection dedicated to the discovery of neutrino of cosmogenic origins is focusing on extremely high-energy (*EHE*) neutrinos. It recently produced the best limits so far for a cosmogenic neutrino flux (see Figure 3.7 [100]).

The HESE and EHE selections are currently used to provide realtime information to the scientific community [101]. An alert system has been developed, which shares with multiple instruments within the AMON project the direction coordinates and energy of track-like events in the IceCube detector. A GCN notice is also shared with the community shortly after the first reconstruction of track-like events that pass the HESE or EHE selection. This system has played a central role in the process of finding the first evidence of neutrino emission from a blazar (see Section 5.7).

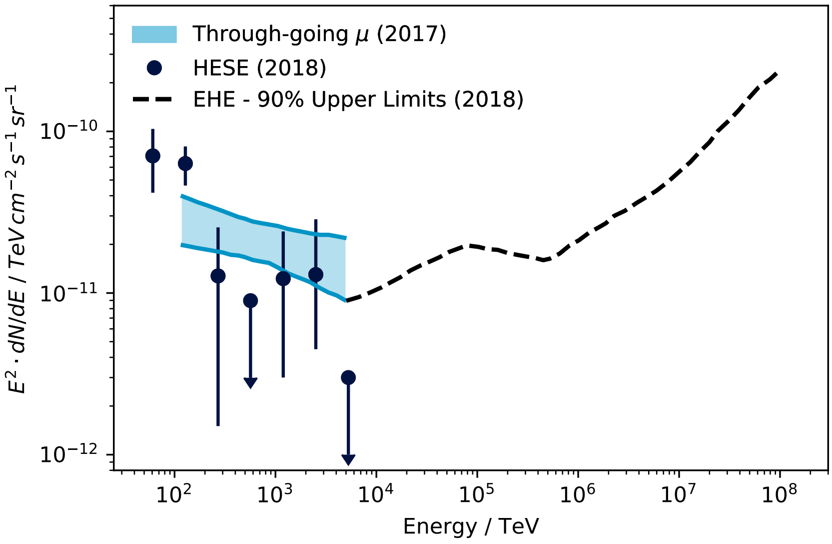

Figure 3.7: Unfolded neutrino flux measured with HESE (black dots) [1], compared with the best fit astrophysical muon neutrino flux obtained from the trough-going tracks (cyan band)[2] and upper limits on cosmogenic neutrino flux from the EHE selection (dashed line) [100].

4

Searching for Small Scale Anisotropies in the Neutrino Sky

In the first part of the chapter the status of the point-like sources searches is summarized, with particular focus on the most recent results connected to blazars. The second part of the chapter will present the results of a two-point autocorrelation analysis performed on 7 years of IceCube data. These results have been presented at the 35th International Cosmic Ray Conference [102], *M. G. Aartsen et al. The IceCube Neutrino Observatory - Contributions to ICRC 2017 Part I: Searches for the Sources of Astrophysical Neutrinos. 2017.*

4.1 Point-like Sources Searches

Neutrino events originating from a single point-like source naturally tend to cluster around a determinate set of coordinates, providing an unique feature to construct a statistical test in order to identify the position of the source. The first test to be formalized is a binned maximum likelihood test, which uses an elementary counting method to identify windows of the sky in which the number of events is significantly higher when compared to other off-source control regions. Since the background is constant and uniform in the spatial coordinates, the choice of the window size is left to the accuracy of the reconstruction of the events, which as shown in Figure 4.2 depends on the energy of the event. An additional feature of the atmospheric background, as showed in chapter 3, is that its energy spectrum steeply drops with increasing energies, uncovering the expected astrophysical component.

The addition of the energy information to the statistical test, together with the event-by-event coordinates and the angular reconstruction uncertainties, bring to the development of the unbinned maximum likelihood formulation that is nowadays largely used in neutrino astronomy. The formalism is usually summarised by the expression

$$\mathcal{L}(\vec{x}_S, n_S, \gamma) = \prod_{i=1}^{N} \left[\left(\frac{n_s}{N} \right) \mathcal{S}_i(\vec{x}_i, \vec{x}_S, E_i, \gamma) + \left(1 - \frac{n_s}{N} \right) \mathcal{B}_i(\vec{x}_i, E_i) \right], \tag{4.1}$$

where the product is performed over the N events present in the data sample and the value n_S represents the number of signal events in the sample. The factor $\mathcal{S}$ represents the probability of a single event to have a signal origin given a source of spectral index γ. It is usually expressed as

$$\mathcal{S}_i(\vec{x}_i, \vec{x}_S, E_i, \gamma) = \frac{1}{2\pi\sigma_i^2} e^{-\frac{|\vec{x}_i - \vec{x}_S|}{2\sigma_i^2}} \cdot \mathcal{E}_S(\vec{x}_i, E_i, \gamma), \tag{4.2}$$

where the first factor represents the spatial probability of the event and the factor $\mathcal{E}$ represents the energy probability. This last factor is estimated using Monte Carlo events originating from a source with spectral index γ at coordinates $\vec{x}_S$.

The factor $\mathcal{B}$ has a similar construction, with the additional simplification thanks to the spatial uniformity of the background:

$$\mathcal{B}_i(\vec{x}_i, E_i) = \frac{\mathcal{P}(\delta_i)}{2\pi} \cdot \mathcal{E}_B(\delta_i, E_i). \tag{4.3}$$

The first spatial probability factor here depends only on the declination δ_i of the event thanks to the daily rotation of the IceCube detector around the right ascension axis. The second factor does not depend on an energy spectrum γ and in the standard approach it is estimated directly from the distribution of the measured data.

The significance of the clustering at a determinate source position can be evaluated with a standard likelihood ratio test of the maximised likelihood versus the null hypothesis, defined as

$$\mathcal{TS} = \log \Lambda = 2 \log \frac{\mathcal{L}(n_S, \gamma)}{\mathcal{L}(n_S = 0)}. \tag{4.4}$$

With this definition, $\mathcal{TS}$ should then be distributed as a χ^2 with two degrees of freedom. Its distribution is nevertheless fitted from scrambled experimental data in order to avoid artifacts. In the standard analysis, the likelihood is maximised only over the two parameters n_S and γ. The likelihoods of different data samples are evaluated separatedly to account for differences in selections and variables distributions produced *e.g.* by different detector geometries.

In a so called *All Sky* search, the likelihood calculation is performed on each point of an isotropic grid that covers the whole sky. This grid is constructed with a point-to-point spacing chosen to be smaller than the expected event angular resolution. The most significant point in the sky is therefore identified as a *hotspot* and its significance is usually expressed with a p-value after the necessary correction for the *Look Elsewhere Effect*. For a detailed explanation of the method see [103] and references therein.

4.1.1 The Event Sample

In order to maximize the chances to observe the faint neutrino signal of a point-like source over an overwhelming atmospheric background, many steps have to be performed before obtaining the final data sample. The experimental data needs to be processed in detail to select the best events to use for the task and to obtain high quality measurements of the variables that will enter the likelihood calculation. In order to increase the statistics of neutrino events, the selection is applied to through-going muons that leave a track like signature inside the detector. These category of events is dominated by many orders of magnitude by muons of atmospheric origin even in the upgoing direction that is shielded by the Earth. A multivariate selection technique is tuned on a fraction of the experimental data and subsequently applied to the whole sample to best discriminate the neutrino signal from the expected background.

The two halves of the sky as seen by the IceCube detector are significantly different, for this main reason the selection is split in two from the start. The Northern Sky contains upgoing events with $\delta \geq -5°$, the Southern Sky contains downgoing events with $\delta \leq -5°$.

Different levels of filtering are responsible for skimming the data and subsequently applying more complex and computational demanding reconstructions only to the most interesting events.

- *Level 0* - The first layer of selection consists in collecting the data from the different triggers and filtering them.
- *Level 1* - This further step applies the HLC condition and performs the first analytical reconstructions.
- *Level 2* - This level is responsible of cleaning the events from spurious pulses and to perform a further set of advanced reconstructions using the ones performed at the previous level as seeds.
- *Level 3* - At this point, selection cuts on the quality of the tracks are applied and finally the most complex reconstruction algorithms are used.

The large amount of reconstruction variables is at this point used to optimize the selection and to train multivariate selection algorithms like *Boosted Decision Trees* (BDTs). The scores of the BDTs are finally used to perform the final cuts on the data that will enter the analysis.
The first runs recorded by the IceCube detector date back to April 2008, when the detector was still incomplete. The first seasons of IceCube are then treated differently from the ones in which the detector was fully operational. The details of the seasons are briefely summarised in the following paragraphs (for a detailed description of the sample see [103] and references therein).

- IC40 - The season of data taking started in April 2008 and ended in May 2009, with a total uptime of 375.5 days. The cuts applied for the selection are described in details in [104]. The full sample consists of 14121 upgoing events and 22779 downgoing events, for a total of 36900 events.
- IC59 - The second season of data taking started in May 2009 and ended in May 2010, collecting a total uptime of 348.1 days. Straight cut were replaced by two Boosted Decision Trees which operate on a total of 12 variables. A

combination of the two scores is used to perform the final event selection. The training of the BDTs is performed using 10% of the experimental data, after randomizing the right ascension values, as background description. The signal fraction is obtained from Monte Carlo simulation, assuming a spectrum of E^{-2} and $E^{-2.7}$. This is the first season which uses the additional information provided by the IceTop surface array as a veto for events reconstructed with a downgoing direction ($-90° \leq \delta \leq -40°$). The efficiency of the veto is estimated at 99% in this declination band [105]. The total sample consists of 107569 events, 64257 downgoing and 43312 upgoing.

- IC79 - This season consists of 316.2 days of uptime, going from June 2010 until May 2011. The selection is here further refined, training multiple BDTs for events originating from the northern hemisphere and one BDTs for the southern one. The different rates between the declination bands that correspond to each BDT are subsequently matched by applying the proper energy cut. This season makes use for the first time of the directional reconstruction that uses the splines to describe the photon propagation in ice (SplineMPE). This new feature, together with the improvements in the BDTs, permits an enhanced backround rejection [106]. The sample contains a total of 93842 events, divided in 48904 upgoing and 44938 downgoing.

- IC86-I - This is the first season that benefits of a complete detector geometry, which records 333 days of uptime between May 2011 and May 2012. The definition of the BDTs is changed again, and four BDTs are present for the northern hemisphere defined between the declinations $-5°$ and $90°$ and divided in two declination bands. Only one BDT is used for the southern hemisphere. The total number of events of the sample is 138322, with 69227 upgoing and 69059 downgoing events [107].

- IC86-II-III-IV - Three full seasons of IceCube have here been processed together, providing uniformity to a statistically large sample of events. A total of 1058 days of uptime are collected. The selection is performed similarly to IC86-I, using different BDTs to distinguish signal from background events in the two hemispheres. The sample consists of a total of 338585 events, 235602 upgoing and 102983 downgoing [103].

The *Point Source* (PS) sample consists of 7 years of data for a total of 2431 days of uptime and 711869 events. The sample clearly differentiates the northern from the southern hemisphere, with a boundary placed at the declination angle of $-5°$. For this reason, the analyses presented in this chapter will provide results from each hemispheres separately.

Both the event selection and the evaluation of the performance of the final sample rely strongly on the studies of simulated events. Monte Carlo samples of muon neutrinos leaving a signal in the detector are used, each different geometry has been simulated and it is used to evaluate IceCube performances for the different seasons. The standard scenario of an astrophysical signal with a power law spectrum with a γ index of -2 is usually assumed as a benchmark configuration, and it is therefore used in all the following plots if not specified otherwise.

The efficiency of the detector, that considers the convolved factors of geometrical acceptance and the probability of observing an event at a certain energy, is usually expressed with a quantity called *Effective Area*. The effective area increased over the years, reaching its full potential with the completion of the detector and remaining constant in the 86 strings configuration. The effective area in different declination bands at different energies is reported in Figure 4.1 for the IC86 samples. At higher energies, it is possible to notice the effect of the Earth absorption, which makes the detector more efficient for detecting tracks coming from horizontal directions. The energy threshold for events from the Southern hemisphere is significantly higher, and increases with the verticality of a track. This effect is caused by the declination dependent energy cuts necessary to remove the background of atmospheric muon bundles.

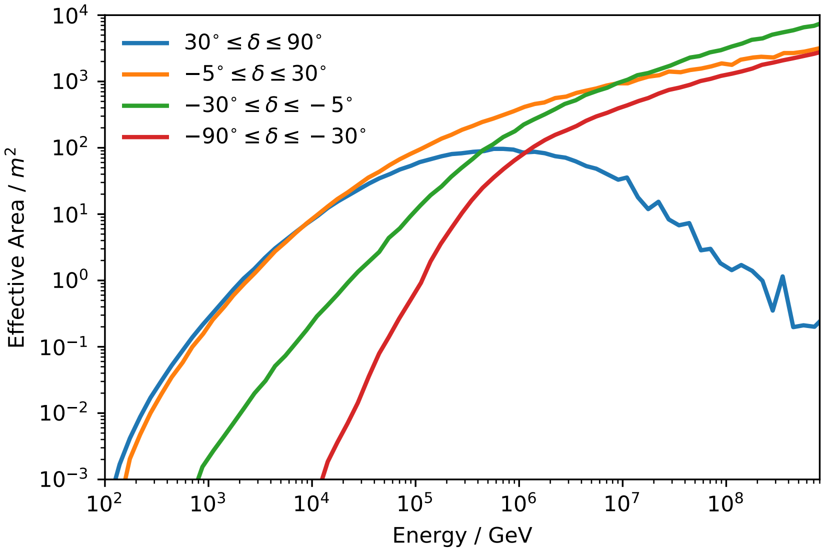

Figure 4.1: Effective area of the detector with a complete geometry as function of the primary neutrino energy. Different colors represent different declination bands. At declinations between 30° and 90° (blue line) the effective area shows a decreasing behaviour starting at approximately 10^6 GeV, this is due to the assorbtion effect caused by the Earth.

Another important parameter to evaluate the quality of a sample that is going to be used to localize point sources is the *Point Spread Function* (PSF). This quantity is usually represented by the median angular uncertainty and it is shown in Figure 4.2. As expected, the accuracy of the reconstruction of the direction of the tracks increased over the seasons, both because of a larger geometry of the detector and because of more efficient reconstruction algorithms. The resolution of the full sample is overall better than 1°, reaching values better than 0.4° in the high energy fraction of the sample.

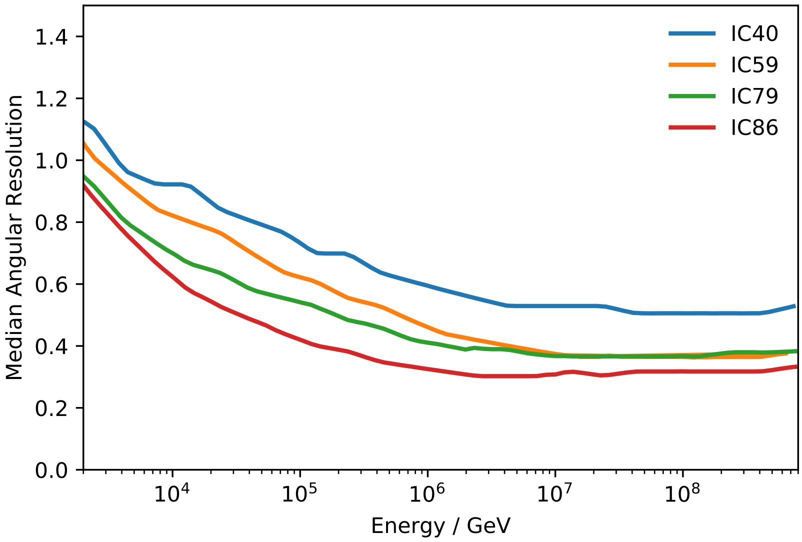

Figure 4.2: Median angular resolution using *SplineMPE* reconstruction as a function of the primary neutrino energy. Different colors are used to distinguish the samples of the different seasons.

4.1.2 RECENT RESULTS

The Point Source Sample, consisting of data recorded over 7 years of detector uptime, has been analysed to look for evidence of neutrino emission from pointlike sources [103]. The search was performed both as an all-sky scan, and using a list of interesting sources identified a priori. The method used is the one described in Section 4.1. The results show no significant clustering of neutrino events over the expected background. The all sky scan identifies the two most significant clusterings (*hotspots*), one for each hemisphere. Both are compatible with the background expectation, yielding 90% upper limits at the level of $E^2 \frac{d\Phi}{dE} \sim 10^{-12}$ TeV cm^{-1} s^{-1} for the Northern Sky and $E^2 \frac{d\Phi}{dE} \sim 10^{-11}$ TeV cm^{-1} s^{-1} for the Southern Sky. The two lists of sources are also fully compatible with the null hypothesis. Figure 4.3 shows the 90% upper limits obtained for the all sky scan (line) and for the objects of the sources lists (dots).

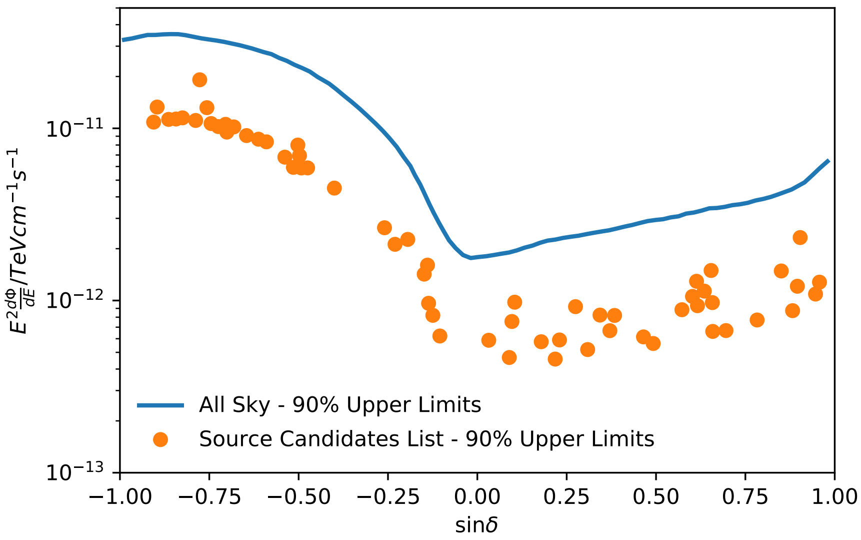

Figure 4.3: Post trial 90% upper limits of the all sky (line), and list (dots) pointlike source search as a function of sine declination. Figure from [103].

4.2 The 2-Point Autocorrelation

The standard likelihood method for the search of point-like sources focuses on looking for a single strong source in the sky. This technique does not perform at its best in the different case of a universe where many sources of neutrinos are emitting fluxes at a level much lower than the sensitivity of the method. The signature of this case would infact be the appearence of many sub-threshold clusterings of neutrinos events, too weak to be significant in the point-like source approach. This scenario of small clusterings becomes relevant both in the case of constant but faint sources, and in the case of more powerful flares, where the signal gets diluted by integrating the analyses over the uptime of the sample.

One method that has been developed to look for multiple clusterings of events is the so called *Two Point Autocorrelation*. This procedure looks for an excess of pair of events at close angular distances, and additionally factors in the calculation the energy information in order to increase its sensitivity. One particular feature of the method is that by design it will look at the data with the most model independent approach possible, turning also out to be sensitive to more general cases than the point-like source, as extended sources at small angular scales.

The method presented here in the following is the updated version of a previous autocorrelation analysis that has been performed on a sample made of four years of detector uptime [108].

4.2.1 THE STATISTICAL METHOD

The idea behind an autocorrelation test is to investigate the presence of hidden correlations between the coordinates of the events in the same data sample. More in detail, the two-point autocorrelation analysis has been proven [108] to be a solid statistical test to assess the presence of spatial clustering at different angular scales in a set of events distributed on a skymap.
The purpouse of this test is to compare two different hypotheses: the *Null Hypothesis* consists of the case of a completely uniform distribution of events over the Sky. This option coincides with the absence of neutrino sources at a flux level that is resolvable by the resolution of the current IceCube detector. The *Signal Hypothesis* consists instead in the existence of a population of sources, of unknown properties, which will reveal itself with a signature in the distribution of events over the sky. The analysis looks at the difference between the two hypoteses in the statistical distribution of the angular distances between event-pairs (i, j). The actual distribution is defined as the cumulative number of event-pairs having an angular distance $\Psi_{i,j}$ that is less or equal

to a defined angular distance θ (angular bin),

$$N(\theta) = \sum_{i,j>i} \Theta(\theta - \Psi_{i,j}), \tag{4.5}$$

where Θ is the Heaviside step function.

One of the concepts at the base of the analysis was to develop its framework by optimizing its sensitivity while keeping the hypothesis almost completely data-driven. The advantage of this approach versus an optimization for a specific source population is that only basics prior assumptions on the signal are needed in order to perform the full analysis. This choice was made to be complementary to many other analyses currently performed by the IceCube Collaboration, which rely on a very detailed description of a possible signal. A more general approach, while likely not providing the best sensitivities to specific cases, results in a larger exploration of the parameter space and it is applicable in various different situations, *e.g.* the analysis on the Cygnus region (see Section 4.2.5).

While reducing the modeling of a signal to the minimum, it is still valuable to assume that astrophysical neutrinos are expected to have a harder spectrum compared to the atmospheric neutrino background. This information has been included in two different ways in the analysis.

- The first and simplest way was to divide the event sample in four subsamples according to the energies of the events. In this way, the *bin* containing only the events with the highest energies would have a natural suppression of the atmospheric background simply because of statistics. This approach will be named *Energy Binned* in the rest of the discussion. The energy bins investigated in this analysis are four, incuding 100%, 10%, 1% and 0.1% of the sample (See Table 4.1).

- The second method, called *Energy Weighted*, can be seen as the limit case of an energy binning, in which every bin has at most one event. This is equivalent to assigning an *energy weight* to each event, which is proportional to its energy. The formulation of the distribution of pairs is changed in this case to

$$N_w(\theta) = \sum_{i,j>i} w_i \cdot w_j \cdot \Theta(\theta - \Psi_{i,j}), \tag{4.6}$$

  where w_i, w_j are the weights assigned to each event. In this case, the number $N_w(\theta)$ is not equivalent anymore to the number of event pairs observed in the sky.

Energy Bin	Minimum Energy [GeV]	No. of Events
	Northern Hemisphere	
100%	7.24	435385
10%	$2.99 \cdot 10^3$	43538
1%	$1.40 \cdot 10^4$	4353
0.1%	$6.05 \cdot 10^4$	435
	Southern Hemisphere	
100%	60.5	290047
10%	$4.73 \cdot 10^5$	29004
1%	$1.02 \cdot 10^6$	2900
0.1%	$2.21 \cdot 10^6$	290

Table 4.1: Minimum energy and number of events for each of the energy bins of the sample, divided in northern and southern hemispheres.

The weighting scheme chosen for the analysis is an update to the one used in [108]. Here the weights are calculated independently from specific signal models, by utilizing the normalized energy distribution $\mathcal{P}(E)$. Each weight is defined as a logarithm of the probability of observing an event with equal or higher energy in the sample and it is calculated as

$$w_i = w(E_i) = -\log_{10}\left(1 - \int_0^{E_i} \mathcal{P}(E)\mathrm{d}E\right). \tag{4.7}$$

The analytical integration results computationally expensive in the analysis framework, for this reason the weight is approximated numerically. Its evaluation is done by summation on the histogram of the energies of the events (Figure 4.4), treating different declination bands separately.

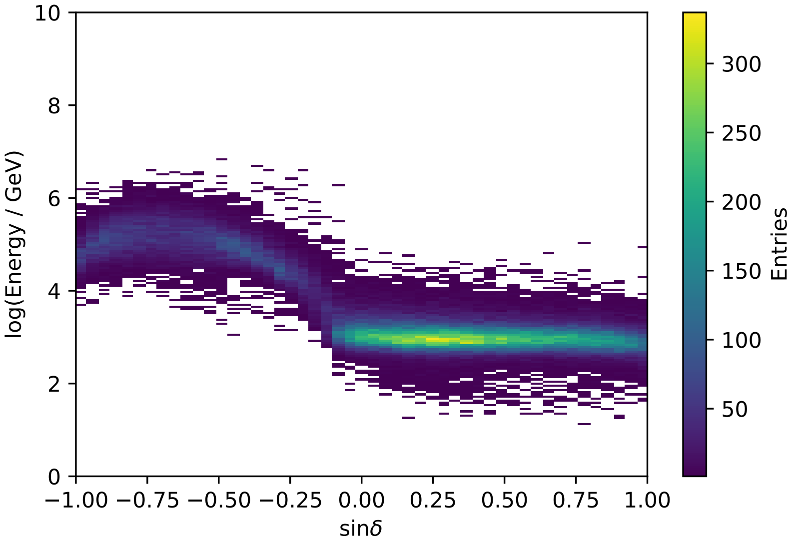

Figure 4.4: Two-dimensional histogram showing events from IC86-II-III-IV. On the x-axis the sine of the declination angle is showed in 50 bins between the values of -1 and 1. On the y-axis the logarithm of the energy is showed in 1000 bins between the values of 0 and 10 ($\log(\mathrm{GeV})$). This histogram is used for the calculation of the energy weights of the events.

4.2.2 The Background Distribution

The background distribution of $N_w(\theta)$ at a given angular scale θ is obtained from performing the analysis many times (*trials*) on skymaps that resemble the *Null Hy-*

pothesis. Background-like skymaps are obtained by assignign random right ascension values to the events of the sample. This procedure, named *scrambling*, produces a skymap with uniformly distributed events, while maintaining the declination dependent acceptance of the IceCube Detector.

The number of pairs $N_w(\theta)$ counted in each of the trials is then histogrammed. The angular scales investigated by the analysis go from $0.25°$ to $5°$ in steps of $0.25°$, for a total of 25 angular bins. Each angular scale θ (*angular bin*) shows a Gaussian shaped distribution, with an asymmetrical tail on the right (see Figure 4.5-Top). This distribution can be approximated with a Gamma Distribution of the form:

$$g(x) = \frac{\beta^{-\alpha}(x-\mu)^{\alpha-1}e^{-\frac{x-\mu}{\beta}}}{\Gamma(\alpha)}, \tag{4.8}$$

where α is the shape parameter, μ the location parameter and β the scale parameter. Since we are interested in calculating a p-value from this distribution, it is computationally convenient to fit the histogram of the inverse cumulative function of the distribution (see Figure 4.5-Bottom). The inverse c.d.f. of the Gamma distribution has the form:

$$c(x) = 1 - \left(\frac{1}{\Gamma(\alpha)}\int_0^{\frac{x-\mu}{\beta}} t^{\alpha-1}e^{-t}dt\right). \tag{4.9}$$

To be conservative and avoid the possibility to obtain artificially low p-values by overfitting low statistics, the right tail of the distribution is modeled with an exponential function, with the transition between the two distributions being at the three sigma value. An example of the *Null Hypothesis* distributions in the northern hemisphere is reproduced in Figure 4.5 (top), which shows the histogrammed number of pairs, calculated as in Eq. 4.6, at the angular scale of $1°$. The corresponding Gamma function (eq. 4.8) at this angular scale is illustrated in red. Figure 4.5 (bottom) illustrates the inverse cumulative representation of the previous histogram, together with the fitted c.d.f. (4.9).

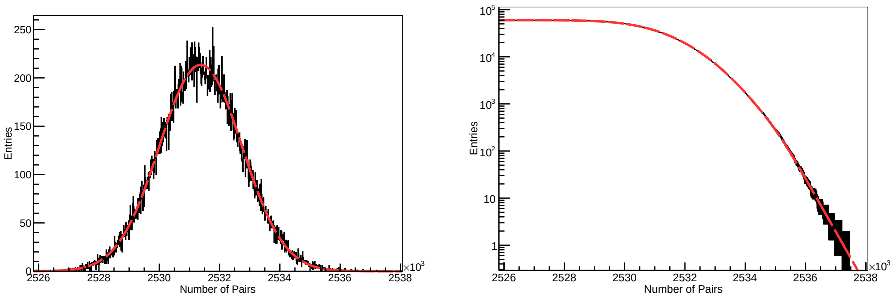

Figure 4.5: Left: Example of the distribution of the weighted number of pairs in the case of a uniform distribution of events in the sky. Values on the x-axis are calculated as in Eq. 4.6, at the angular scale of 1° for the northern hemisphere. The corresponding Gamma function (eq. 4.8) at this angular scale is illustrated in red.
Right: The histogram of the top plot is here illustrated in its inverse cumulative distribution. The fitted gamma c.d.f. of the form 4.9 is depicted in red.

For each trial is then possible to calculate a p-value at each angular bin just by evaluating the corresponding fitted function at the value of the measured number of pairs $N_w(\theta)$ (or $N(\theta)$).

$$p(\theta) = c_\theta(N_w(\theta)) \tag{4.10}$$

The most significant p-value from all the tested angular scales is then choosen to define the test statistic:

$$TS = -\log_{10}(p(\theta)_{\text{Best}}). \tag{4.11}$$

Since the test is repeated many times for different angular scales and energy bins, it is necessary to consider the *Look Elsewhere Effect*. In order to correct for the trial factor a large number of isotropic realization of the skymap is produced. This is needed to obtain the distribution of the TS variable in the *Null Hypothesis* case (see Figure 4.6). The trial corrected p-value is then equivalent to the probability of obtaining a TS at least as large as the one obtained from data. The distribution of the most significant

TS in the northern hemisphere is showed in Figure 4.6, the red over-imposed solid line represents its expected analytical distribution:

$$f(x) = a_0 \ln(10) N \left(1 - e^{-a_0 \ln(10) x}\right)^{N-1} e^{-a_0 \ln(10) x}, \qquad (4.12)$$

where a_0 is a scale parameter and N corresponds to the effective trial factor. The effective trial factors are approximately 5 for the Energy Weighted analysis and 21 for the Energy Binned analysis. These values are smaller than the total number of angular bins because the angular bins are mutually dependent, *i.e.* larger angular scales contain the event-pairs of smaller angular scales, thus reducing the total number of effective trials. The Energy Binned approach is performed on additional four energy bins, providing a larger trial effect. The median and the 5σ value of the distribution are used in the evaluation of the sensitivity and the discovery potential of the method (see Section 4.2.4).

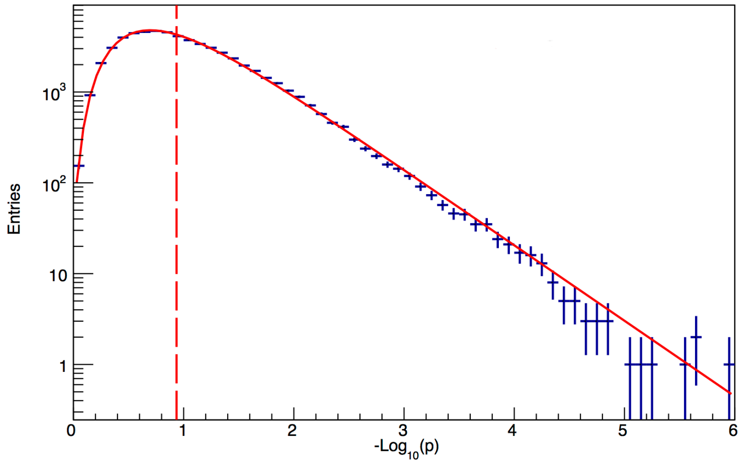

Figure 4.6: Distribution of the best TS values ($-\log_{10}(p)$) for $6 \cdot 10^5$ background trials reproducing a uniform distribution of events in the northern hemisphere. The results of the trials is histogrammed (blue markers), the median value of the distribution is marked with a dashed red line. The red solid line over-imposed on the histogram represents the fitted analytical expected distribution of the best best TS values (Equation 4.12).

It is additionally interesting to study the distribution of the angular bin that provides the best TS. The angular scale that shows the most significant evidence of events clustering can provide useful information on the angular spread of the event clustering around the source. This evidence can be used to differentiate the case of point-like sources versus more extended sources. The distribution of the most significant angular bin in the case of a background-like skymap is showed in Figure 4.7.

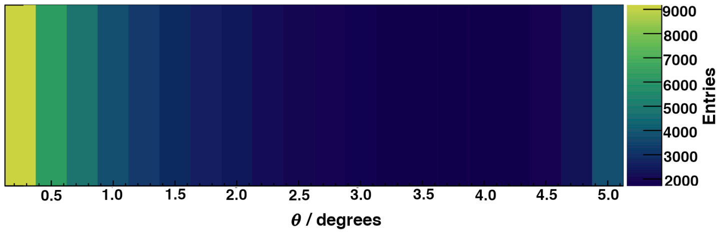

Figure 4.7: Distribution of angular bin θ that produces the best TS values for $6 \cdot 10^5$ background trials reproducing a uniform distribution of events in the northern hemisphere. The most significant clustering is observed most likely from the smallest angular scale tested.

4.2.3 SIGNAL INJECTION

In order to evaluate the performances of this method, it is necessary to test it in scenarios that will resemble the presence of signal. This is done by creating skymaps that contain both scrambled data events and Monte Carlo generated events located as if they originated from one or more sources. The procedure of injection of signal events in the skymap is illustrated in the following:

1. The first step consists in creating a uniform skymap by scrambling in right ascension all the data events.

2. The position of a fixed number of sources (N_{Sources}) is generated uniformly over the sky.

3. To each source a weight (w_s) is assigned; w_s is proportional to the acceptance of the detector for the declination band in which the source lies. The sum of the weights is normalized among the sources.

4. A random number of events (N_{Injected}) is drawn from a Poissonian distribution with a fixed mean value (N_{Events}).

5. A mean number of $N_{\text{Injected}} \cdot w_s^j$ events is distributed over each source j according to a Poissonian distribution.

6. Events for injection are selected from the same declination band in which the source is located. The energy spectrum of the injected events is choosen and it is uniform among the sources.

7. The true Monte Carlo direction of each injected event is rotated to the position of the corresponding source, the same rotation matrix is used to rotate the reconstructed direction.

8. In case of extended sources, an additional separation from the center of the source is included in the rotation.

9. For each injected event, the background event that lies closest in declination is removed from the skymap

10. After the new skymap is created, the energy weights are calculated.

The distribution of the TS of the sky realisations that contain injected events is then compared to the background distribution in order to evaluate the power of the test. The effect of the event injection is evident in Figure 4.8. The histogram is showing the distribution of the TS for $5{\cdot}10^3$ random trials with signal injection in the skymap. As expected, the distribution (solid blue line) is shifting to more significant values when compared to the background-like distribution (blue dashed line).

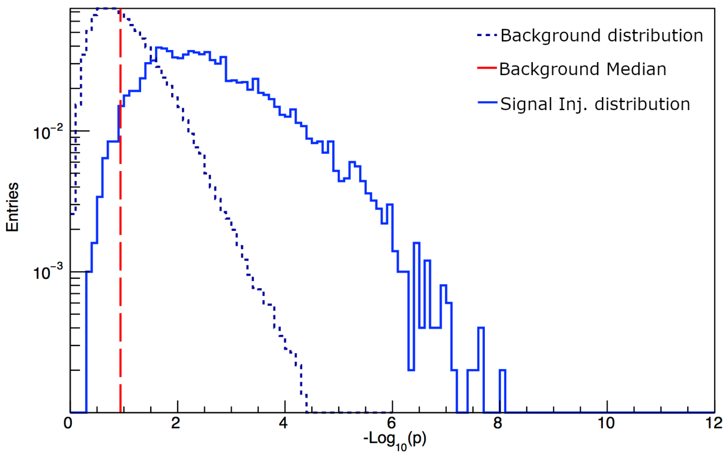

Figure 4.8: Distribution of the best TS values ($-\log_{10}(\mathrm{p})$) for 5000 trials with signal injection, values are histogrammed (blue line). The signal scenario consists of 100 point-like sources with a source strength of 7 events per source. The blue dashed lines shows the background scenario as comparison, together with the background median (red dashed line).

Figure 4.9 (Top) shows the distribution of the most significant angular bin for the same signal injection scenario illustrated in Figure 4.8. It is possible to notice the difference in the same distribution resulting from random trials in which a scenario with extended sources with gaussian shape are injected in the skymap 4.9 (Bottom). The feature here highlighted can be used to distinguish the two different cases.

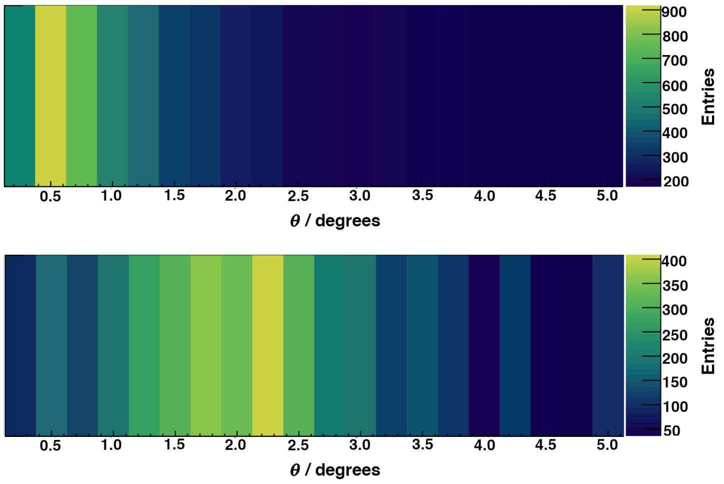

Figure 4.9: Top: distribution of angular bin θ that produces the best TS values ($-\log_{10}(p)$) for 5000 trials with signal injection (same scenario as Figure 4.8).
Bottom: distribution of angular bin θ that produces the best TS values ($-\log_{10}(p)$) for 1000 trials with signal injection. The scenario injected corresponds in this case to 30 sources with a source strength of 3 events per source. The sources are in this case extended, with a gaussian shape with $\sigma = 2^\circ$. It can be noticed that in this case the clustering manifests at a larger angular scale when compared to the point-like source case.

4.2.4 PERFORMANCE

The performance of an analysis method are usually evaluated by the calculation of two different neutrino fluxes to which the method is sensitive. The *Sensitivity Flux* is defined as the flux needed to shift 90% of the TS distribution to values higher than the median of the background distribution. The *Discovery Potential Flux* is defined as the flux needed to shift 50% of the TS distribution to values higher than the 5σ quantile of the background distribution.

Figure 4.10 (top) and Figure 4.10 (bottom) show respectively Sensitivity and Discovery Potential for the autocorrelation analysis illustrated in the previous Sections. Blue colors represent the values relative to the northern hemisphere, orange colors the ones relative to the southern hemisphere. A solid line is used for the energy weighted approach, while a dashed line is used for the Energy binned. It can be noticed that the Weighted method outperforms the Binned one. For this reason, the former will be used to calculate results and the latter will be performed only as a cross check. Upper Limits from the point source analysis [103] are included as a comparison (shaded areas). The through-going ν_μ best fit flux [2] is also showed (dash-dotted line). Whenever the lines of the current analysis are above the through-going ν_μ best fit flux, the proposed method is not sensitive enough to the measured flux.

Sensivity fluxes have also been estimated for two additional cases, different from the standard point-like sources with an energy spectrum proportional to E^{-2}. The first alternative scenario consist of extended sources, of gaussian shape with $\sigma = 1°$. The sensitivity flux per source in the case of 100 sources is in this case $E^2 dN/dE = 3 \cdot 10^{-7} TeV cm^{-2} s^{-}1$. The second alternative scenario keeps the sources point-like, but changes the energy spectrum to E^{-3}. The sensitivity flux per source in the case of 100 sources is in this case $E^3 dN/dE = 4 \cdot 10^{-7} TeV^2 cm^{-2} s^{-}1$. Both fluxes refer to the Energy Weighted method.

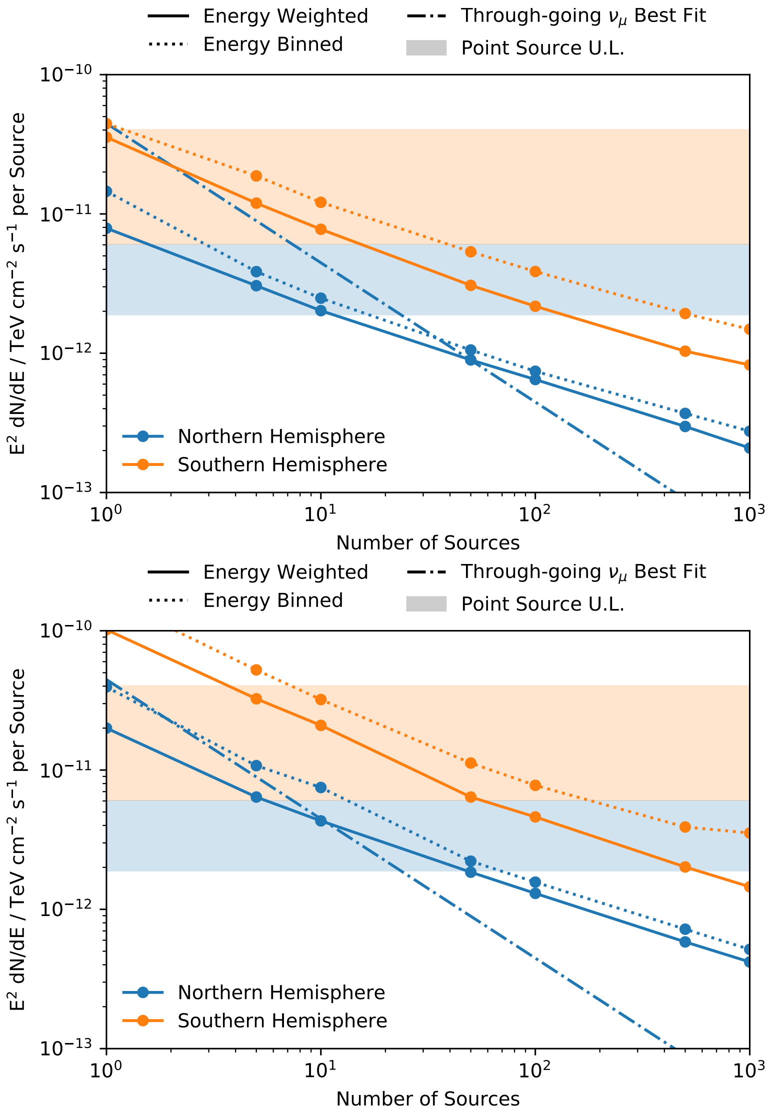

Figure 4.10: Sensitivity (**top**) Discovery Potential (**bottom**) fluxes of the two-point autocorrelation analysis. lux per source is plotted on the y-axis, the x-axis represents the number of sources present in the skymap. Blue colors represent the values relative to the northern hemisphere, orange colors the ones relative to the southern hemisphere. A solid line is used for the energy weighted approach, while a dashed line is used for the Energy binned. Upper Limits from the point source analysis [103] are included as a comparison (shaded areas). The through-going ν_μ best fit flux [2] is also showed (dash-dotted line).

4.2.5 RESULTS

The two-point autocorrelation analysis illustrated in the previous section has been performed on the 7 years data sample described in Section 4.1.1. The results are compatible with the background expectation of an isotropic neutrino events distribution over the sky, with no evidence of clustering at any angular scale in the range from 0.25° to 5°. Flux upper limits are calculated with frequentist approach at the 90% confidence level and compared to the results of the point source analysis and the flux measured by the through-going ν_μ best fit [2, 103]. The results are presented in the following Sections, divided in northern and southern hemispheres.

NORTHERN HEMISPHERE

The results of the Two-Point Autocorrelation analysis performed on the northern hemisphere are compatible with the null hypothesis. The results are showed in Figure 4.11 (top panel) as measured number of weighted event-pairs (N_{pairs}) divided by the number of expected pairs ($< N_{pairs} >$) in a background-like scenario. The coloured bands represent the statistical uncertainty on $< N_{pairs} >$ at the one, two and three σ levels. A black dot represents a measurement at each angular scale (θ) that has been tested. The corresponding pre-trial p-value is reported for each measurement in the lower panel. The most significant p-value among the different angular scales is highlighted in red. A trial corrected p-value of 45%, compatible with the background expectation, is calculated for the most significant angular scale ($\theta = 1.75°$).

Flux upper limits at the 90% confidence level are calculated as the neutrino flux needed to shift the 90% quantile of the TS distribution above the most significant TS value obseved in the data. Figure 4.12 shows the upper limits as flux per source for a point-like source scenario (solid blue line) and for a gaussian-shaped source with

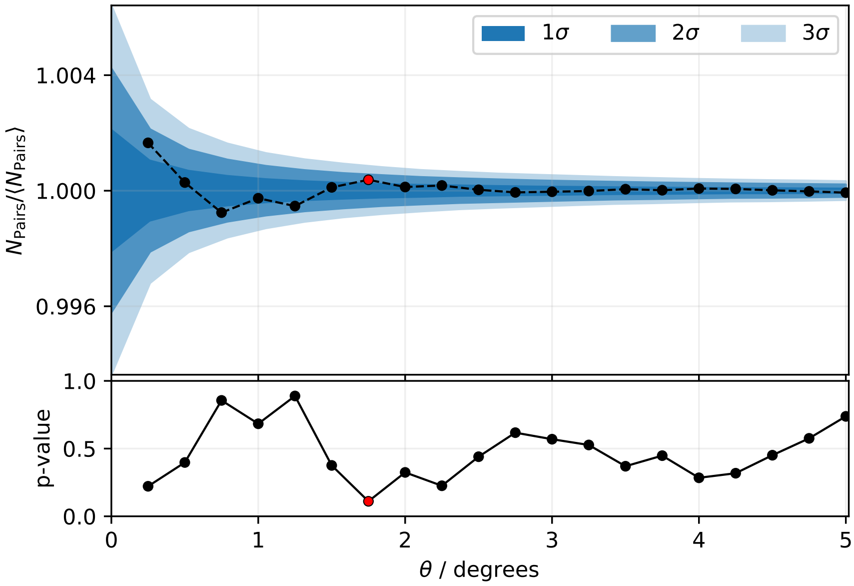

Figure 4.11: The results of the two-point autocorrelation analysis in the northern hemisphere are showed in the top panel. The y-axis represents measured number of weighted event-pairs (N_{pairs}) divided by the number of expected pairs ($< N_{pairs} >$) in a background-like scenario. The coloured bands represent the statistical uncertainty on $< N_{pairs} >$ at the one, two and three σ levels. A black dot represents a measurement at each angular scale (θ) that has been tested (x-axis). The corresponding pre-trial p-value is reported for each measurement in the lower panel. The most significant p-value among the different angular scales is highlighted in red.

$\sigma = 1^{\circ}$ scenario (dashed blue line). The limits are valid for populations of sources of different number densities, but with the same luminosity at Earth and with an unbroken energy spectrum proportional to E^{-2}. The flux values are presented as a function of the number of sources injected in the skymaps. For comparison, the range of the 90% upper limits from the point source analysis in the northern hemisphere is reported as a blue band. The measured astrophysical diffuse flux is also showed with a bule dash-dotted line.

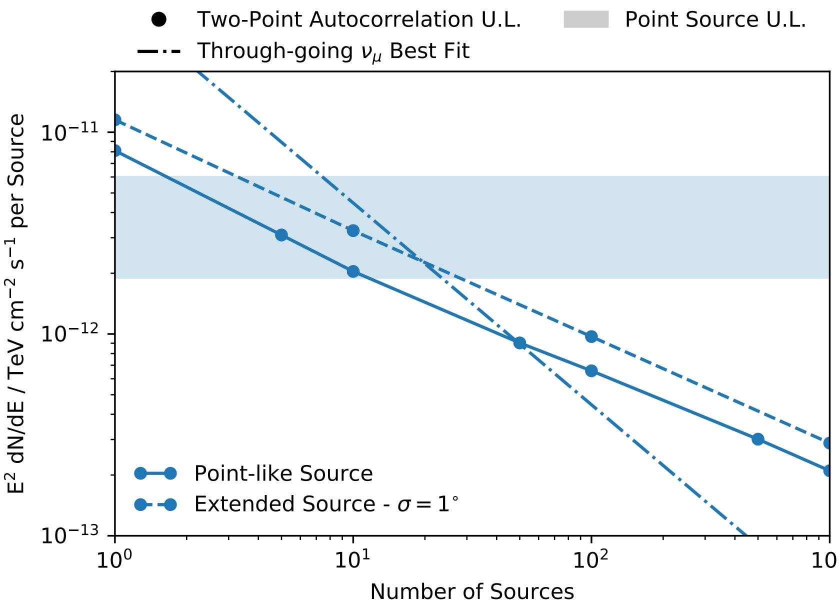

Figure 4.12: Flux upper limits at the 90% confidence level in the northern hemisphere are reported as flux per source for a point-like source scenario (solid blue line) and for a gaussian-shaped source with $\sigma = 1°$ scenario (dashed blue line). The limits are valid for populations of sources of different number densities, but with the same luminosity at Earth and with an unbroken energy spectrum proportional to E^{-2}. The flux values ar presented as a function of the number of sources injected in the skymaps. For comparison, the range of the 90% upper limits from the point source analysis in the northern hemisphere is reported as a blue band. The measured astrophysical diffuse flux is also showed with a bule dash-dotted line.

Southern Hemisphere

Similarly to the northern hemisphere, the results of the Two-Point Autocorrelation analysis performed on the southern hemisphere are fully compatible with the background hypothesis. The results are showed in Figure 4.13 (top panel) as measured number of weighted event-pairs (N_{pairs}) divided by the number of expected pairs ($< N_{\mathrm{pairs}} >$) in a background-like scenario. The coloured bands represent the statistical uncertainty on $< N_{\mathrm{pairs}} >$ at the one, two and three σ levels. A black dot represents a measurement at each angular scale (θ) that has been tested. The corresponding pre-trial p-value is reported for each measurement in the lower panel. The most significant p-value among the different angular scales is highlighted in red. A trial corrected p-value of 60%, suggesting a mild statistical underfluctuation, is calculated for the most significant angular scale ($\theta = 2.25°$). In the first bin a strong underfluctiation can be observed. This is caused by a very limited statistics in the number of pairs at very small angular distances. This underfluctuation is prograssively absorbed by the bins at larger angular scales.

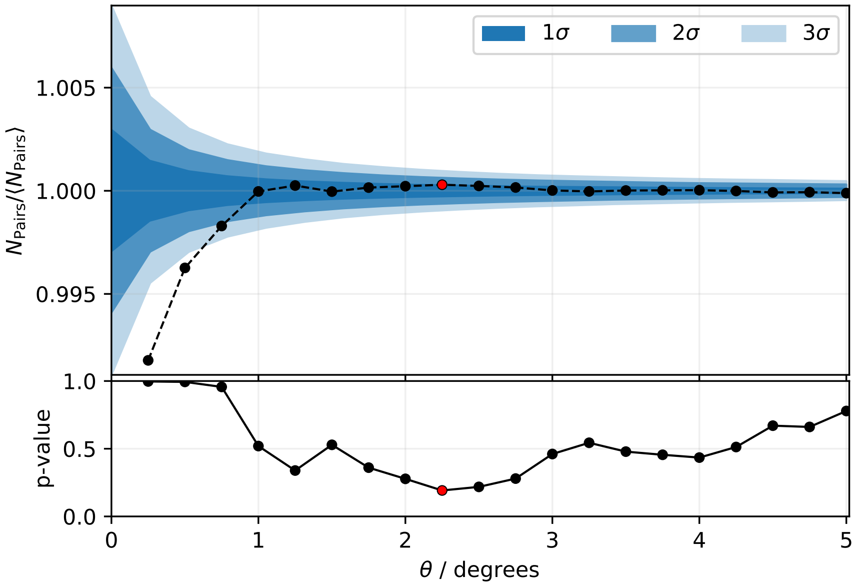

Figure 4.13: The results of the two-point autocorrelation analysis in the southern hemisphere are showed in the top panel. The y-axis represents measured number of weighted event-pairs (N_{pairs}) divided by the number of expected pairs ($< N_{pairs} >$) in a background-like scenario. The coloured bands represent the statistical uncertainty on $< N_{pairs} >$ at the one, two and three σ levels. A black dot represents a measurement at each angular scale (θ) that has been tested (x-axis). The corresponding pre-trial p-value is reported for each measurement in the lower panel. The most significant p-value among the different angular scales is highlighted in red.

Figure 4.14 shows the upper limits as flux per source for a point-like source scenario (solid orange line) and for a gaussian-shaped source with $\sigma = 1°$ scenario (dashed blue line). The flux values ar presented as a function of the number of sources injected in the skymaps. The limits are valid for populations of sources of different number densities, but with the same luminosity at Earth and with an unbroken energy spectrum proportional to E^{-2}. For comparison, the range of the 90% upper limits from the point source analysis in the southern hemisphere is reported as an orange band.

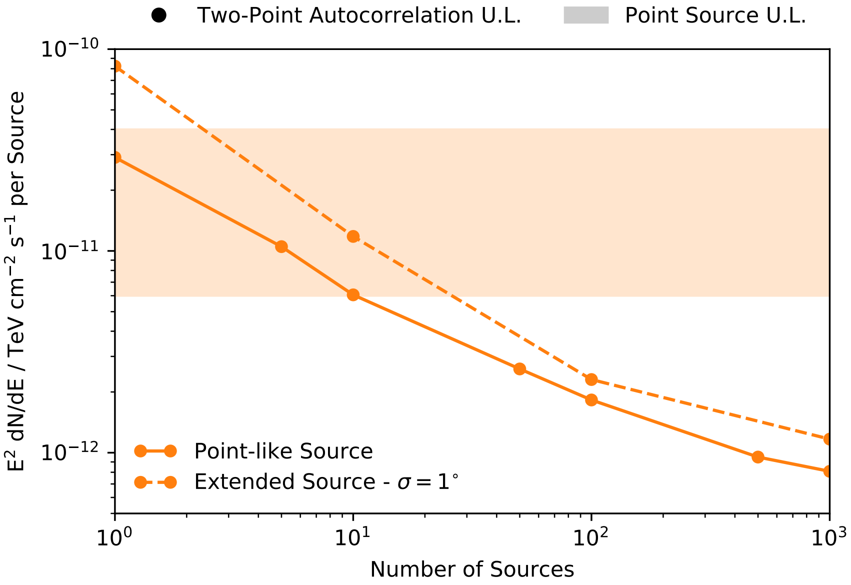

Figure 4.14: Flux upper limits at the 90% confidence level in the southern hemisphere are reported as flux per source for a point-like source scenario (solid orange line) and for a gaussian-shaped source with $\sigma = 1^\circ$ scenario (dashed orange line). The flux values ar presented as a function of the number of sources injected in the skymaps. The limits are valid for population of sources of different number densities, but with the same luminosity at Earth and with an unbroken energy spectrum proportional to E^{-2}. For comparison, the range of the 90% upper limits from the point source analysis in the southern hemisphere is reported as an orange band.

The Cygnus Region

A previous version of the two-point autocorrelation analysis was also performed on the area of Galactic sky called Cygnus region [108], resulting compatible with the background hypothesis. The update of the analysis presented here was also applied to this interesting region in order to provide updated limits.

The Cygnus region is defined here as the area of the sky extending between 72° and

83° in galactic longitude and -3° and 4° in galactic latitude. It is a massive star forming region, which is very bright in diffuse emission of galactic γ-rays and a very promising source of galactic neutrinos. Extensive studies have been performed by γ-ray experiments at different wavelengths ranging from radio to TeV energies. The presence of multiple bright sources of γ-rays, superimposed with the galactic diffuse emission creates an environment challenging to study. Different generations of surveys such as Milagro [109, 110], Veritas [111] and more recently HAWC [112] have nevertheless observed extended regions of γ-ray emission. CR acceleration and correlated neutrino production have also been considered for the region [113, 114].
Similarly to what has been done to the northern and southern hemispheres, the results of the two-point autocorrelation analysis are here presented. Given the smaller size of the area of the sky under analysis, it was computationally possible to reduce the spacing of the angular scales grid (θ) from 0.25° to 0.1°. Figure 4.15 (top panel) shows the results as measured number of weighted event-pairs (N_{pairs}) divided by the number of expected pairs ($< N_{pairs} >$) in a background-like scenario. The coloured bands represent the statistical uncertainty on $< N_{pairs} >$ at the one, two and three σ levels. A black dot represents a measurement at each angular scale (θ) that has been tested. The corresponding pre-trial p-value is reported for each measurement in the lower panel. The most significant p-value among the different angular scales is highlighted in red. A trial corrected p-value of 53%, in agreement with the expected values of a background scenario, is calculated for the most significant angular scale $\theta = 0.1^\circ$. An evident underfluctuation is present for all the angular scales larger than 0.3°.

Figure 4.16 shows the upper limits as flux per source for a point-like source scenario (solid orange line) and for a gaussian-shaped source with $\sigma = 1^\circ$ scenario (dashed blue line). The flux values ar presented as a function of the number of sources injected in the region. The limits are valid for sources with the same luminosity at Earth and

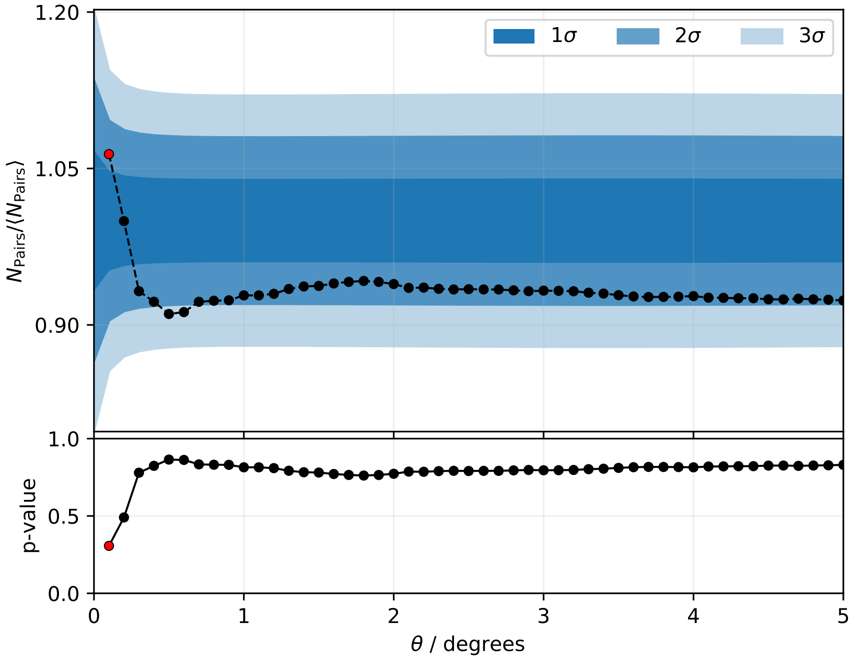

Figure 4.15: The results of the two-point autocorrelation analysis in the Cygnus Region are showed in the top panel. The y-axis represents measured number of weighted event-pairs (N_{pairs}) divided by the number of expected pairs ($< N_{pairs} >$) in a background-like scenario. The coloured bands represent the statistical uncertainty on $< N_p airs >$ at the one, two and three σ levels. A black dot represents a measurement at each angular scale (θ) that has been tested (x-axis). The corresponding pre-trial p-value is reported for each measurement in the lower panel. The most significant p-value among the different angular scales is highlighted in red.

with an unbroken energy spectrum proportional to E^{-2}.

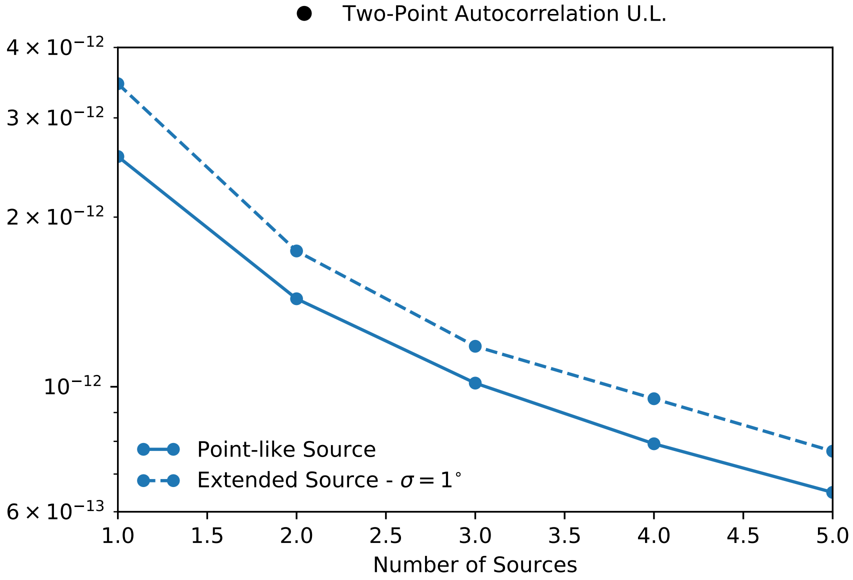

Figure 4.16: Flux upper limits at the 90% confidence level in the Cygnus region are reported as flux per source for a point-like source scenario (solid blue line) and for a gaussian-shaped source with $\sigma = 1^\circ$ scenario (dashed blue line). The flux values ar presented as a function of the number of sources injected in the region. The limits are valid for sources with the same luminosity at Earth and with an unbroken energy spectrum proportional to E^{-2}.

4.3 DISCUSSION

A two-point autocorrelation analysis has been performed on a data sample covering 7 years of uptime of the IceCube detector. In order to properly treat the different level of atmospheric background and to account for the differences in event selection, the northern and southern hemispheres have been analyzed separately. An additional test has been performed on the active galactic area called Cygnus Region. The results of the different searches are all very well consistent with the background hypothesis of isotropic distribution over the sky of astrophysical neutrino events. The southern hemisphere and the Cygnus region show a mild statistical underfluctuation in the number of measured event-pairs.

Upper limits at the 90% confidence level have been calculated for a population of sources with the same luminosity at Earth and with an unbroken energy spectrum proportional to E^{-2}. The case of point-like versus extended sources of gaussian shape has also been tested, calculating the relative upper limits. The analysis on the northern hemisphere, which is the most sensitive in terms of perfotmance, produced upper limit fluxes per source that range from $8 \cdot 10^{-12}$ TeV cm^{-2} s^{-1} in the case of one single source in the sky, to $9 \cdot 10^{-13}$ TeV cm^{-2} s^{-1} for 50 sources. While the former value is already ruled out by more stringent upper limits from the point source analysis [103], the latter is the last one allowed by the measurement of the diffuse astrophysical neutrino flux [2].

5

The γ-rays Counterparts

As discussed in chapters 1 and 2, the combined production of neutrinos and γ-rays is predicted by all hadronic mechanisms that try to describe the origin of CRs. It is therefore straightforward to try to use the information provided by one of these two messengers to identify the sources of the second one. This process can work in two specular ways: using the precisely known locations of the γ-ray sources to search for an accumulation of neutrino events, or using the less precisely reconstructed neutrino direction to look for a correlation with observed γ-ray sources. The first Section of this chapter will briefly discuss the most recent results obtained using the first approach on blazar catalogs. The second part of the chapter will focus on the search for γ-ray counterparts for the published IceCube neutrino events.

5.1 BLAZAR STACKING

The standard way to look for an accumulation of neutrino events at a single source position is the point source likelihood method illustrated in chapter 4. The most recent results looking at the position of known γ-ray sources and using the event sample described in chapter 4 are illustrated as upper limits in Figure 4.3 [103].

This method has not yet observed any neutrino source with high enough significance. For this reason the focus has shifted towards detecting a population of fainter sources. The method used to detect a population of sources at given known locations is an extension of the single source likelihood and it is called *Stacking*. In the same formalism discussed previously, the signal factor $\mathcal{S}$ of the likelihood (Eq. 4.2) is replaced by the weighted sum of the signal probabilities the event would have at each source position:

$$\mathcal{S}_i \rightarrow \mathcal{S}_i^{\text{Stack}} = \frac{\sum_{k=1}^{M} \mathcal{W}_k \cdot \mathcal{R}(\delta_k, \gamma) \cdot \mathcal{S}_k(\vec{x}_i, \vec{x}_k, E_i, \gamma)}{\sum_{k=1}^{M} \mathcal{W}_k \cdot \mathcal{R}(\delta_k, \gamma)}. \tag{5.1}$$

The factor $\mathcal{W}_k$ represents a theoretical weight given to each source k, which can be proportional to intrinsic properties of each source, *e.g.* luminosity, redshift, etc. The factor $\mathcal{R}(\delta_k, \gamma)$ accounts for the detector acceptance at declination δ_k for a source with a spectral index γ. The sum is performed over all the M sources of the catalog taken into consideration. Excluding this modification, the rest of the analysis is performed in the same way as a standard point source analysis.

The most recent results of a stacking analysis published by IceCube use three years of data (IC59, IC79, IC86-I) from the event selection discussed in Section 4.1.1 [115]. The sources under investigation are blazars of BL-Lac and FSRQ type, taken from the Fermi 2LAC catalog (see Section 5.4). The results of the analysis do not show any significant excess of neutrino emission at the location of 2LAC blazars. The upper limits on the flux are illustrated in Figure 5.1. When compared to the measured astrophysical neutrino diffuse flux, the tested catalog can explain a maximum of almost 30% of the total flux under the model assumption of an unbroken power-law. If a correlation between the neutrino flux and the γ-ray flux of the sources is introduced as a weighting parameter, an even smaller fraction is obtained. These results have been confirmed and even more stringent limits have been placed by more recent analyses performed both on an updated neutrino data sample, and on different and more recent catalogs [102].

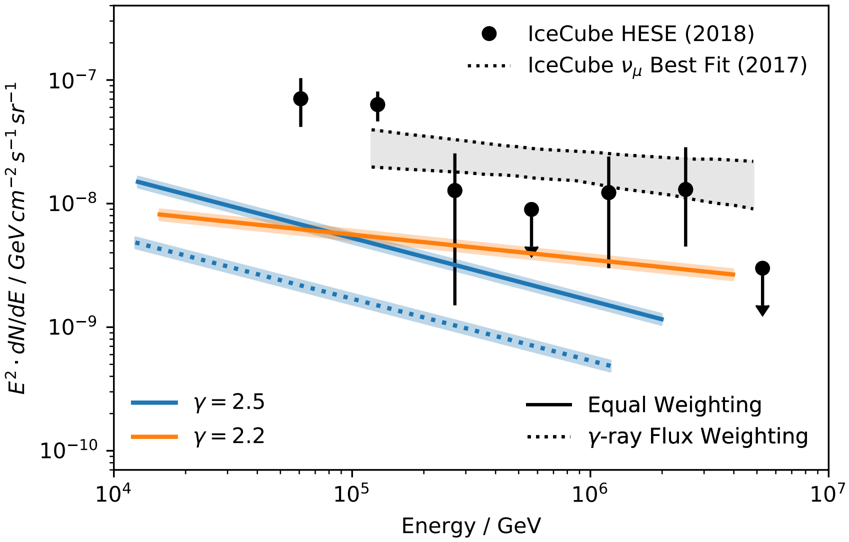

Figure 5.1: 90% upper limits on the stacking analysis performed with three years of IceCube data on blazars of the 2LAC catalog [115].

5.2 The Counterpart Method

The study of the correlation between neutrinos and γ-ray sources follows here the method used in [53]. The observable N_ν represents the number of neutrino events with at least one counterpart within the individual angular uncertainty. It is defined as

$$N_\nu(i) = \sum_\nu \Theta\left(\sum_{\gamma\in\mathcal{S}_i} \Theta\left(\sigma_\nu - \psi_{\gamma,\nu}\right)\right), \tag{5.2}$$

where the sums are performed over all the events in the neutrino sample (ν), and all the sources that belong to the sub-group $\mathcal{S}_i$ of the γ-ray catalog (γ). Each subsample is created by selecting all the sources of the catalog that fulfill a specific requirement, *e.g.* a flux larger than a specific threshold. The neutrino angular uncertainty corresponds to σ_ν and $\psi_{\gamma,\nu}$ is the angular distance between the neutrino event and the source location. The function $\Theta(x)$ is the Heaviside step-function, defined as follows.

$$\Theta(x) = \begin{cases} 0, & \text{if } x \leq 0 \\ 1, & \text{if } x > 0 \end{cases} \tag{5.3}$$

Scanning different partitions of the catalog by defining increasing flux thresholds presents an advantage over scanning the catalog as a whole. The scan will infact highlight the case in which only sources above a determinate flux are associated with IceCube events.

The chance probability $P(i)$ represents the likelihood to observe a given N_ν from the catalog subsample $\mathcal{S}_i$, and it is calculated by comparing the result to background-like cases. The background cases are generated by creating randomised skymaps in which either the neutrino events or the γ-ray sources are placed isotropically in the sky. The preferred strategy, in order to not alterate a possible large scale structure of the source population, is to scramble the neutrinos in right ascension, leaving the position of the sources untouched. This method is not applicable in the case of a catalog constructed by a survey that is not uniform over the full sky and focus only on specific regions. In this case a scrambling of the neutrinos cannot conserve the total area sampled by the neutrinos error circles, resulting in a biased statistics. The solution of this problem consists in leaving the neutrinos at their coordinates and randomising the positions of the sources inside the area covered by the survey.

A p-value is calculated for each of the subsamples of the catalog and the one with the highest significance is selected as results. In order to correct for the *Look Elsewhere Effect*, the usual trial correction procedure is applied.

5.3 The Neutrino Events

The neutrino event sample used to perform the analysis with the method described in Section 5.2 has been constructed by collectiong the publicly available events released by the IceCube collaboration. These events are selected by various IceCube analyses, using different filtering techniques and thus presenting distinct topologies inside the detector. The common characteristic that brings all these events together is the very high likelihood of having an astrophysical origin.

The first set of events used to build the full sample is the one selected and published over 6 years by the HESE analyses. It consists of high energy events that start inside the detector volume. The majority of the events are reconstructed with a cascade topology, presenting a large angular uncertainty compared to the remaining part of the sample, which is made of starting tracks. The second set of events is made of high-energy, through-going muon tracks, with an angular uncertainty smaller than 1°. The sample covers 8 years of detector uptime. The remaining events are collected from the public alerts that the IceCube collaboration has been providing in the last two years through the GCN network. For more details about the samples see Section 3.4.2 and references therein.

In order to select only events with a good enough reconstruction to perform a correlation analysis, and to more strictly remove any contamination by atmospheric neutrinos, two further cuts are applied to the neutrino sample.

1. The angular uncertainty of each event is required to be smaller than 20°.
2. Only events with a reconstructed energy higher than 60 TeV are allowed in the sample.

The final sample of neutrinos is illustrated on a skymap in Figure 5.2, the angular uncertainty is depicted with white circles. The color scale represents the number of overlapping neutrino events at a given point in the sky. The full sample consists of 110 neutrino events, of which 76 are tracks while the remaining are cascades. For a complete list and summary of the selected events, refer to [116].

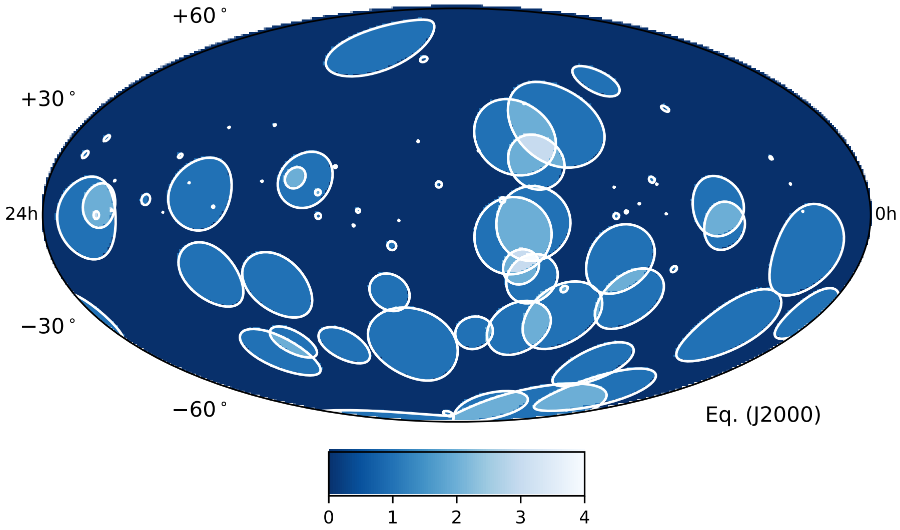

Figure 5.2: Position in the sky of the neutrino events selected for the correlation analysis. The angular uncertainty is depicted with white circles. The color scale represents the number of overlapping neutrino events at a given point in the sky.

5.4 THE FERMI/LAT EXPERIMENT

The *Large Area Telescope* (*LAT*) is the primary instrument of the *Fermi Gamma-ray Space Telescope* (*Fermi*) mission [117]. The LAT was launched in orbit in June 2008 by NASA and has been operating since. The main purpouse of the telescope is to measure coordinates, energy and arrival time of γ-rays over a wide field of view. The mechanism of operation is the conversion of colliding γ-rays into an electron-positron pair via interaction with a high-Z material. The telescope consists of four main subsystems: a precision tracker, a calorimeter, an anticoincidence detector (ACD) and a Data Aquisition System (DAQ) (see Figure 5.3). The tracker consists of a 4x4 array of 16 modules, where converter planes made of tungsten are coupled with position-sensitive silicon-strip detector. Additionaly, each tracker module has 18 tracking layers that contribute to the measurement of the tracks of the charged particles produced by the pair conversion. The calorimeter is made of 96 CsI(Tl) crystal, stacked in 8 layers of 12 elements each. The main purpouse of this subsystem is to measure the energy deposited by the interaction of the γ-ray, while its secondary function is to provide a background discriminator by imaging the development of the electromagnetic particle shower. The ACD is made of plastic scintillator material and covers the previous subsystems. Its purpouse is to reject with high efficiency the background of charged particles entering the tracker and calorimeter. The on-board DAQ system collects all the data recorded by the other instruments. It is also responsible for implementing the trigger and it performs online computations to reconstruct and filter the measured events in order to reduce the volume of data to transfer to Earth. Additional science tools are provided online to perform fast transient searches. The main observing mode of the telescope is the so called *Scanning Mode*, which offers an almost uniform coverage of the entire sky in about 3 hours of time. In the case of interesting targets, the observatory can be also pointed.

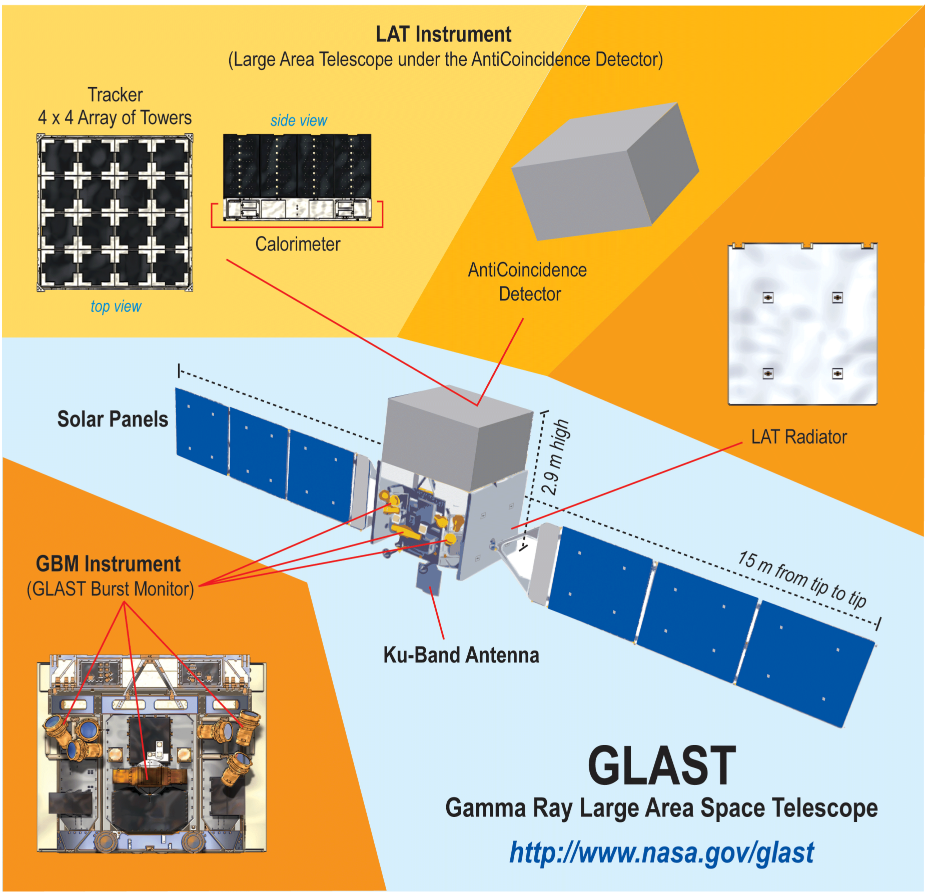

Figure 5.3: Schematic illustration of the Fermi/LAT space observatory. The single elements of the satellite are highlighted, the components of the LAT instrument are described in the text.

5.5 The 3FHL Catalog

The *Third Catalog of Hard Fermi*-LAT *Sources* (3FHL) is based on 7 years of data of the Fermi Large Area Telescope [118]. The catalog contains sources detected in the energy band that goes from 10 GeV to 2 TeV and it is made of a total of 1558 objects. The sensitivity and angular resolution are improved with respect to both the previous version of the catalog (1FHL [119]) and the 2FHL catalog [120], which had an energy threshold of 50 GeV. Among the different types of sources, the catalog lists 750 blazars of the BL-Lac type, 172 FSRQs and 290 additional blazar of unidentified category.

The SED of all the objects has been furtherly analyzed by using the tools provided by the Open Universe* project [121]. For each blazar object a manual fit to the energy distribution has been performed, in order to provide the most precise estimation possible of the ν peak. The results provide a detailed characterization of the catalog, as summarized in the second column of Table 5.1.

5.5.1 Results

A previous iteration of a counterpart analysis of the type described in Section 5.2 has been performed in [53]. The analysis was performed on a smaller neutrino sample, consisting of 4 years of HESE events and 6 years of through-going muon events. Among the various tested catalogs, the results were consistent between each other, providing significance at the two sigma level in the case of the 2FHL catalog. The source class that was showing the highest level of correlation with the neutrino events was the HBL. An updated version of both catalog and neutrino sample provides an interesting chance to further investigate the correlation previously observed. The results of the test are reported per source class in Table 5.1.

To highlight any correlation between neutrinos and the measured flux of the sources of the catalog, a scan on different partition of the catalog has been performed. Results are presented in Figure 5.5. The most significant p-value is obtained from the partition of the catalog containing HBL sources with a $F_{\gamma}(> 10 \mathrm{GeV}) > 8.43 \cdot 10^{-11}$ ph cm^{-2} s^{-1}. The p-value corresponds to 0.35 pre-trials, which becomes 0.65 after trial correction. The skymap showing both neutrinos and sources of the partition

---

*http://www.openuniverse.asi.it/

Source Class	Number of Objects	p-value
All Sources	1558	0.89
Blazar	1301	0.8
HBL	637	0.65
Non-Blazar	149	0.84

Table 5.1: Summary of the Counterpart analysis on the 3FHL Catalog. The analysis is performed separately on the different classes of sources, identified after the manual fit of ν peak [121]. P-values are trial corrected for testing multiple partitions of the catalog. Calculations are performed on sets of 5000 background-like sky realizations. Trial correction is applied.

providing the best p-value is showed in Figure 5.4.

In agreement with the choices in [53] regarding the γ-ray sources catalogs, objects close to the Galactic Plane have been removed from the sample. The SED of these objects is infact harder to analyse, presenting strong influence from photons originating in our Galaxy. Since the interest of the analysis relies on extra-galactic objects, this choice has also the positive outcome of removing spurious coincidences. After removing sources lying closer than $10°$ to the Galactic Plane and being careful in performing the random scrambles as discussed in 5.2, the most significant p-value is obtained from the same partition of the catalog containing HBL sources. The p-value is slightly more significant: 0.12 pre-trials, which becomes 0.33 after trial correction. The results of the scan are presented in Figure 5.6. From this point, all the results presented will include this prescription in treating objects close to the Galactic Plane.

The counterpart analysis in [53] observed a correlation between sources of HBL type and neutrinos with a cascade topology. This was believed to be caused by the small statistics of neutrino events with a track topology. Figure 5.7 shows the results of the counterpart analysis on the HBL sources using the two topologies of neutrino events separately. The same conclusion can be taken from the new results.

The distribution of the expected number of counterparts from background-like

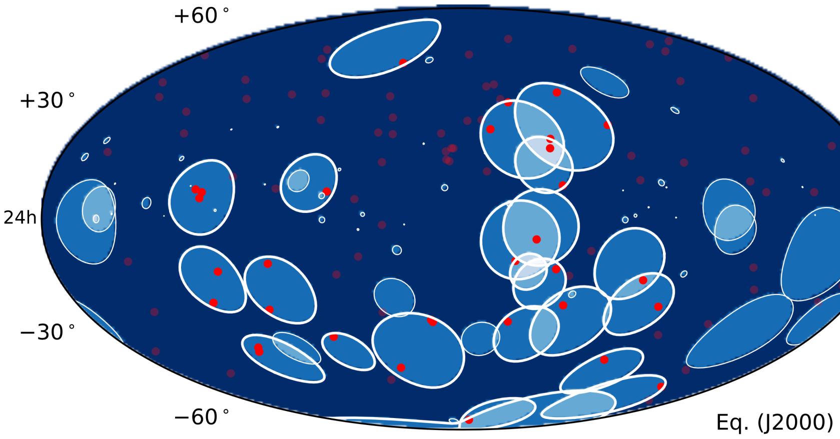

Figure 5.4: Skymap showing the position of the HBL sources in the 3FHL catalog belonging to the partition which provides the best p-value in the correlation test. Bright red circles show sources that lie inside the angular uncertainty of neutrino events, shaded red circles show non-correlating sources. Neutrinos are represented with the same style as Figure 5.2.

skymaps is presented in Figure 5.8, the measured number of counterparts is reported with a red vertical line. The distribution is calculated for the most significant partition of the catalog of sources of the HBL type. The three histograms represent the distribution obtained using the complete neutrino sample (*All*), and only events of a given topology (*Tracks, Cascades*).

To compare the results of the test with the previous analysis, the effect of the update on the neutrino sample and on the catalog are studied independently. Figure 5.9 (left) shows the result of the analysis that is obtained by using the HBL sources from the 3FHL catalog to look for correlation with the neutrino sample used in [53]. Figure 5.9 (right) is instead showing the results of the analysis that uses the current neutrino sample and the HBL sources from the 2FHL catalog.

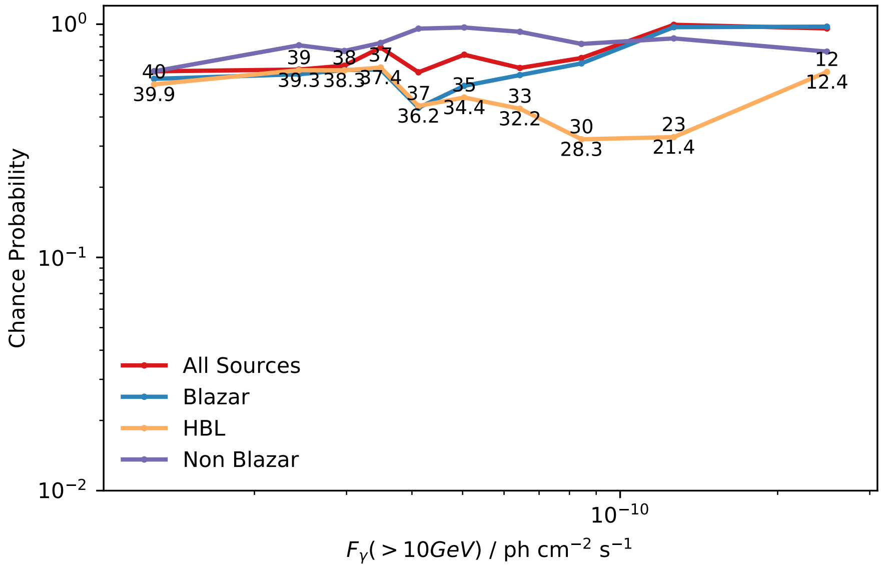

Figure 5.5: Chance probability of correlation between IceCube neutrinos and different classes of sources of the 3FHL Catalog (different colors). The results are shown for the case of background realization by scrambling the position of the sources of the catalog. The x-axis represents the thresholds in photon flux at which the catalog has been partitioned. The numbers represent the measured number of neutrino-source counterparts (top) compared to the expectation from background of the same quantity (bottom).

5.5.2 Discussion

The results of the counterpart analysis show a relevant reduction of the significance when compared to the results in [53]. This shift goes in the opposite direction of what would be expected if a direct correlation between sources of the HBL type and astrophysical neutrinos was real. Nevertheless, in the light of what is described in Section 5.7 it seems premature to conclude that there is no correlation at all.

A deeper look at the results shows that the updates applied to the analysis might not have trivial effects, and some parallels remain when compared to the previous test. The first analogy is the fact that the subcatalog containing HBL sources remains the one that provides the strongest significance of correlation with neutrinos. The over-

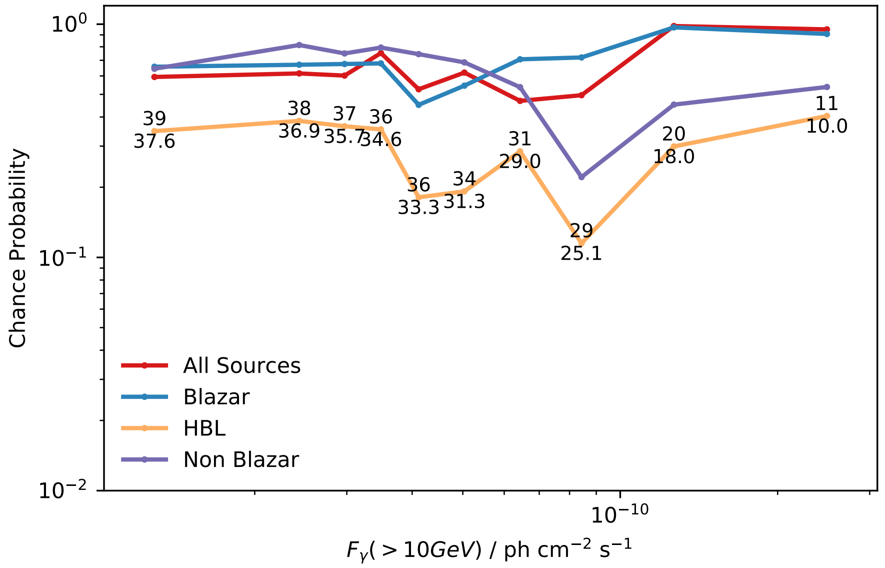

Figure 5.6: Chance probability of correlation between IceCube neutrinos and different classes of sources of the 3FHL Catalog after removing objects lying closer than 10° to the Galactic Plane (different colors). The results are shown for the case of background realization by scrambling the position of the sources of the catalog. The x-axis represents the thresholds in photon flux at which the catalog has been partitioned. The numbers represent the measured number of neutrino-source counterparts (top) compared to the expectation from background of the same quantity (bottom).

all effect of the change to the 3FHL catalog is very small, but nevertheless negative. On the catalog side, it is not clear what is the contribution of a change of threshold in the source selection between the second and the third version of the FHL catalog. The updated neutrino sample has a much stronger effect in reducing the significance. The first track-like events start to correlate with sources as expected with the increase of statistics in this topology. As seen in the previous test, cascade events are still the most significant contributors in the test. It is important to notice that with the increase of neutrino statistics, events with a large angular uncertainty like the ones with cascade-like topology will start to lose their power in filtering out interesting sources by spuriously selecting random objects in the sky. It is then believed that an update in

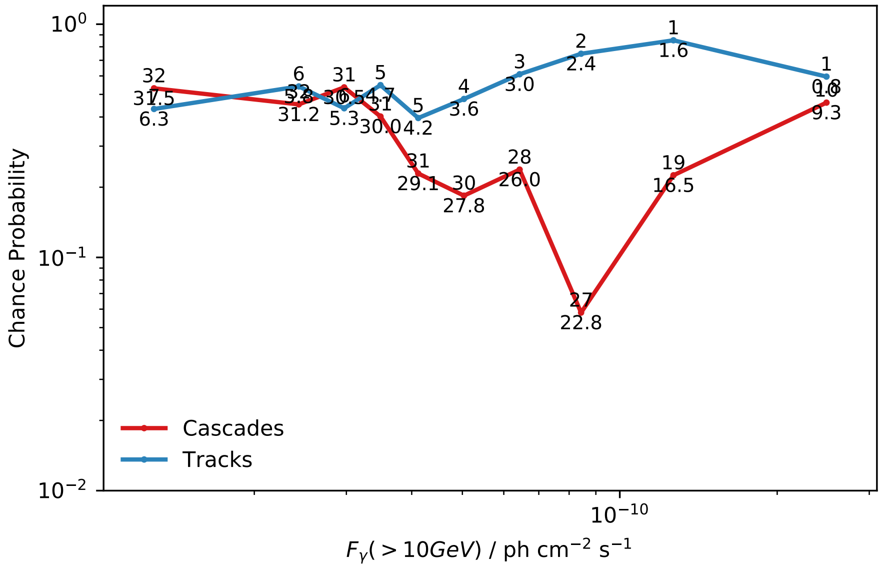

Figure 5.7: Chance probability of correlation between IceCube neutrinos and HBL sources from the 3FHL Catalog. The results are shown for the case of background realization by scrambling the position of the sources of the catalog. The x-axis represents the thresholds in photon flux at which the catalog has been partitioned. The neutrino sample is divided according to event topology: cascades are represented in red and tracks in blue. The numbers represent the measured number of neutrino-source counterparts (top) compared to the expectation from background of the same quantity (bottom).

the algorithm will be needed in the next iterations of the analysis if more neutrino data will be available. For these reasons, Section 5.6 will be focused on track-like events, exploring the possibility of a systematic underestimation of the angular error attributed to the neutrino tracks.

The results provided in this Section are the preliminary steps of an analysis using all the three astrophysical messengers taken into consideration in this work (see chapter 6).

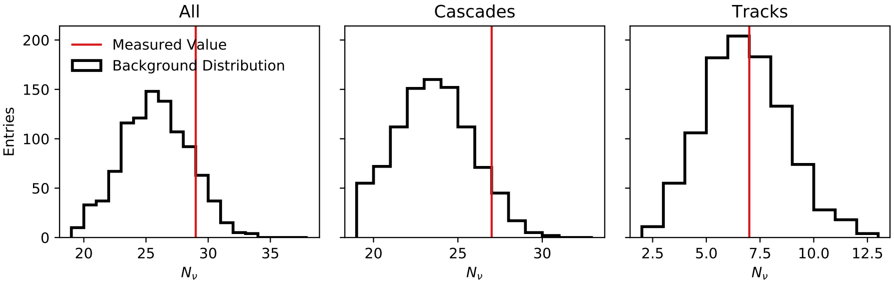

Figure 5.8: Distribution of the expected number of counterparts from background-like skymaps (black). The measured number of counterparts is reported with a red vertical line. The distributions are presented for the most significant partition of the catalog of sources of the HBL type. The three histograms represent the distribution obtained using the complete neutrino sample (*All*), and only events of a given topology (*Tracks, Cascades*).

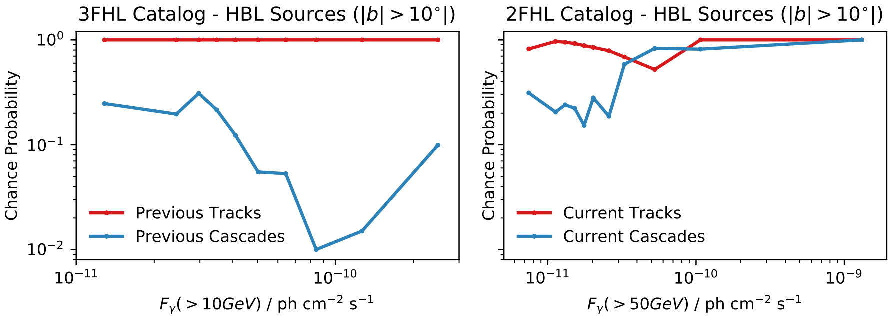

Figure 5.9: Left: Chance probability of correlation between IceCube neutrinos from [53] and HBL sources from the 3FHL Catalog. **Right:** Chance probability of correlation between IceCube neutrinos sampled in this work and HBL sources from the 2FHL Catalog. The results are shown for the case of background realization by scrambling the position of the sources of the catalog. The x-axis represents the thresholds in photon flux at which the catalog has been partitioned. The neutrino sample is divided according to event topology: cascades are represented in red and tracks in blue.

5.6 THE 3HSP CATALOG

A counterpart analysis similar to what has been performed on the 3FHL Catalog in the previous section is here performed as a test on a preliminary version of the 3HSP Catalog [122]. This catalog will become the third version of the *WISE High Synchrotron Peaked* (2WHSP) Catalog [123], and collects sources of the BL Lac type with a synchrotron peak higher than 10^{15}Hz. For each source a Figure of Merit (FoM) is calculated, which represents the likelihood of observing the object in the TeV γ-ray band. The FoM is defined as the ratio between the measured flux at the synchrotron peak and the flux of the faintest source detected in the TeV γ-ray band. The total number of sources is increased by 20% from the previous version, to a total of 2012 objects. Half of them have been observed in γ-rays. Figure 5.10 shows the distribution of the objects with respect of the FoM and in comparison to the previous realization of the catalog.

The counterpart method used to calculate the probabilities is described in details in Section 5.2. Each probability corresponds to the likelihood of observing a higher number of counterparts than the number expected from a background scenario. The probabilities are calculated using a sets of 10^5 randomised realisations of the sky.

The test has been performed not only considering the published angular uncertainty of each neutrino (σ), but also testing larger areas ($\Delta\Psi$): namely a factor 1.1, 1.3 and 1.5 times the previous uncertainty. This choice is made in order to take in consideration slightly larger areas of the sky, to include possible systematic effects that would increase the error on the directional reconstruction of the neutrinos.

The columns of Table 5.2 report the observed number of neutrino-source counterparts, which can be compared for each method of randomisation to the expectation from background. Additionally, the probability of observing a larger number

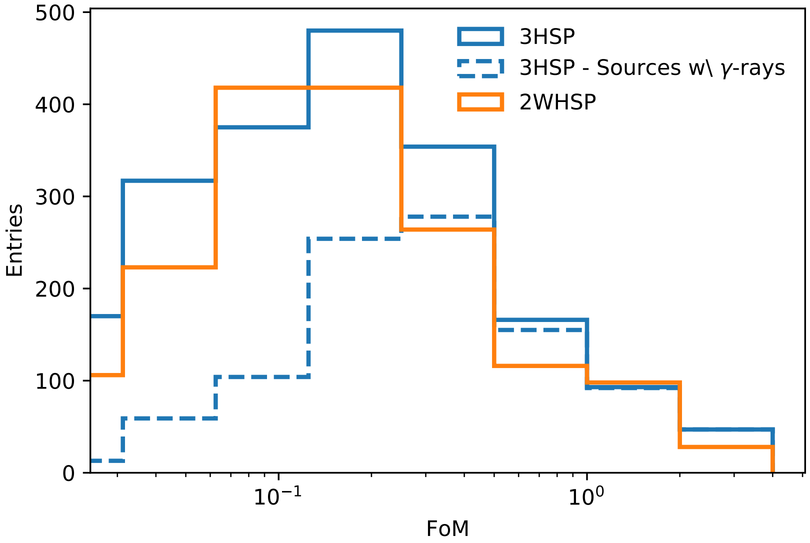

Figure 5.10: Distribution of the sources in the 3HSP (blue) and 2WHSP (orange) catalogs as a function of FoM. The solid line indicates the full catalogs, the dashed line indicates the sources with observed γ-ray emission.

of counterparts is presented. Even though the different tests are highly correlated, a trial correction due to performing multiple tests is applied. The corresponding p-value and its significance in units of sigmas of the Normal distribution is reported once for each randomisation, and once for the complete set of tests. As a cross-check, the exact same procedure has also been applied by selecting areas of fixed size around neutrinos. The radii chosen are $0.5°$, $1°$, $1.5°$, $2°$ and $3°$.

5.6.1 RESULTS

Table 5.2 (top) presents the results of the counterpart test on the 3HSP catalog. Only neutrino events with a track-like topology are used in the calculations of the probability presented in the following table.

An additional scan in FoM, in parallel to what has been done with the energy flux for the 3FHL Catalog in Section 5.5 is reported in Figure 5.11. The plot on the left represents the analysis on the complete 3HSP Catalog, the plot on the right shows the scan only for the sources with observed γ-ray emission. The neutrino angular uncertainty used for the test is the one provided by the IceCube collaboration. Figure 5.12 shows the same results, but in this case obtained by increasing the neutrino angular uncertainty by a factor of 1.3, the value that gives the highest significance in Table 5.2.

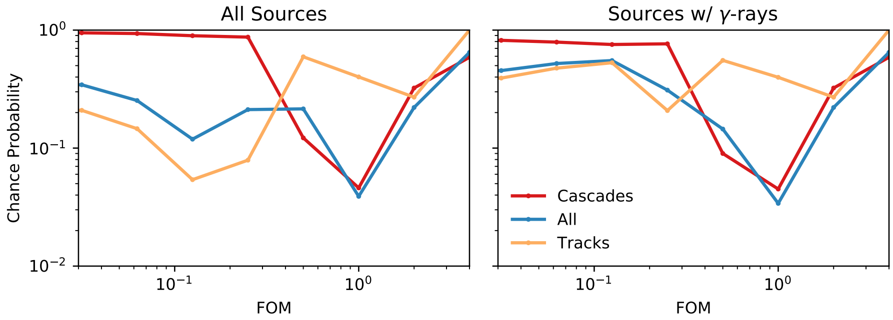

Figure 5.11: Chance probability of correlation between IceCube neutrinos and sources from the 3HSP catalog. The solid line is valid for the full catalog, the dashed line for sources with observed γ-ray emission. The x-axis represents the thresholds in FoM at which the catalog has been partitioned. The results using the complete neutrino sample are represented in blue, while the results divided by topology show cascade-like events in red and track-like events in orange. The plot shows the results obtained by using the neutrino angular uncertainty provided by the IceCube collaboration [116].

5.6.2 Discussion

A reported in Table 5.2, the best p-value observed is 0.007 pre-trial, corresponding to 2.26 sigma after correction for trials. This p-values correspond to counting 27 counterparts over $\sim$ 20 expected from a pure background case and it is obtained by randomizing the galactic longitudes of the full 3HSP Catalog, while using a neutrino angular uncertainty 30% larger than the published angular uncertainty. In contrad-

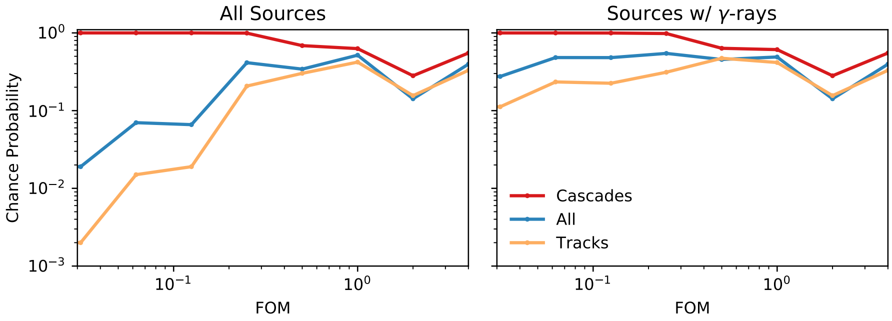

Figure 5.12: Chance probability of correlation between IceCube neutrinos and sources from the 3HSP catalog. The solid line is valid for the full catalog, the dashed line for sources with observed γ-ray emission. The x-axis represents the thresholds in FoM at which the catalog has been partitioned. he results using the complete neutrino sample are represented in blue, while the results divided by topology show cascade-like events in red and track-like events in orange. The plot shows the results obtained by increasing the neutrino angular uncertainty by 30%.

diction to the expectations, the subcatalog of objects with observed γ-ray emission does not seem to contribute to the significance. This can be explained because the contribution to the significance seems to stem from sources with a FoM of the order of 10^{-1}, which are by definition fainter and harder to detect in the γ-ray band. A detailed look at the correlating objects in the regions of sky selected by IceCube events seems therefore to be needed to understand the nature of these potential neutrino sources. It is important to notice that these regions seem to be slightly larger than the angular uncertainty provided by the IceCube collaboration. A dedicated paper is currently in preparation to provide a better insight on these interesting objects [124].

3HSP Catalog			
All Sources		(2012 Objects)	
$\Delta\Psi$	Observed Nr.	Expected Nr.	*p-value*
1σ	17	14.3	0.202
1.1σ	19	15.9	0.183
1.3σ	27	19.2	0.007
1.5σ	29	22.3	0.021
Post trials p-value		0.012 (2.26σ)	
0.5°	5	2.7	0.131
1°	14	10.1	0.115
1.5°	25	20.4	0.143
2°	34	31.2	0.279
3°	51	48.0	0.211
Post trials p-value		0.322 (0.46σ)	
Sources w/ γ-rays		(1012 Objects)	
1σ	10	9.0	0.392
1.1σ	10	10.1	0.592
1.3σ	16	12.5	0.124
1.5σ	19	14.9	0.105
Post trials p-value		0.137 (1.09σ)	
0.5°	3	1.3	0.141
1°	4	5.1	0.787
1.5°	10	11.2	0.701
2°	21	18.5	0.282
3°	36	33.8	0.341
Post trials p-value		0.354 (0.37σ)	

Table 5.2: The table on the *top* reports the observed number of neutrino-source counterparts obtained by using the complete 3HSP Catalog, while the table on the *bottom* report the same quantity obtained by using only the sources with observed γ-ray emission. The number of counterparts can be compared to the expectation from background. Additionally, the probability of observing a larger number of counterparts is presented. A trial correction due to performing multiple tests is applied. The corresponding p-value and its significance in units of sigmas of the Normal distribution is reported. As a cross-check, the exact same procedure has also been applied by selecting areas of fixed size around neutrinos.

5.7 The Random Chance Probability of a Coincidence with a Neutrino Alert

On September 22nd of 2017 an EHE selected neutrino event measured by IceCube triggered a GCN Alert and a follow-up was successfully performed by multiple experiments. For the first time, a coincidence in space and time was observed with the flaring object TXS 0506+056 at a significance of $\sim 3\sigma$ [3]. A subsequent analysis performed on IceCube archival data strongly suggests the presence of a neutrino flare of ~ 5 months length in 2014-2015 from the same source [125]. Further multiwavelength studies show how the object, at first thought to be an ISP *BL Lac*, is instead a masquerading *BL Lac* [126].

It is not the purpouse here to enter the discussion about the object itself, but only to present a statistical framework developed during the first weeks after the observation of the coincidence. The assessment of a spatio–temporal coincidence probability with catalogs of sources and single objects within the catalog is here discussed. This discussion was firstly summarized in an IceCube Internal Report paper (*icecube/201710001*).

We consider the coincidence between one detected neutrino event issued via an EHE or HESE alert and one observed flare from either a generic source from an ensamble or a specific source in a catalog. The coincidence is defined both in time and in angular coordinates. Each IceCube event defines a point in time and a region of the sky to be followed up by other experiments. The coverage by another telescope is approximated as full-sky. The flaring state of the source is defined as a binary decision: the source can be in a *quiescent* state or in a *flaring* one. A quiescent state is equivalent to not observing any coincidence. Every EHE or HESE alert is considered as an independent experiment.

We define the probability of an alert as p_{IC} and the probability a flare as p_{fl}. The goal is to compute the probability that among n trials an alert and a flare are coincident (P_C). Alternatively $P_{\overline{C}}$ is the probability that no coincidence is observed. Since C and $\overline{C}$ are also mutually exclusive, $P_C = 1 - P_{\overline{C}}$.

The binomial distribution is here used with parameters n and p for the discrete probability distribution of the number of coincidences in a sequence of n independent experiments. Each experiment has two possible and mutually exclusive outcomes, namely coincidence or no coincidence.

Two chance probabilities are here considered: the coincidence rate between one generic neutrino alert and one generic flare from a generic source in a catalog, and the coincidence rate between one generic neutrino alert and one generic flare of a specific source. The method we follow here is a classical frequentist method that relies largely on calculating probabilities for spurious coincidences under a null hypothesis of no true associations.

5.7.1 COINCIDENCE WITH SPECIFIC SOURCE

A random association of one neutrino alert with a single source in the sky is given by the probability of the source to be inside the solid angle $\Delta\Omega \approx 2\pi(1 - \cos\Delta\Psi)$ identified by the IceCube event angular uncertainty uncertainty $\Delta\Psi$.

$$P_\Omega = \frac{1 - \cos\Delta\Psi}{2} \approx \frac{\Delta\Psi^2}{4}, \tag{5.4}$$

The probability of a source to be in a flaring state is independent from P_Ω. It is estimated by measuring the fraction of time that the source spent in a flaring state on the total time of the observation. The probability can be expressed as:

$$P_{\text{Flare}} = \frac{T\,(\text{Flaring})}{T(\text{Tot})} \equiv \alpha, \tag{5.5}$$

The probability of the random coincidence is then

$$P_C = P_\Omega \cdot P_{\text{Flare}} \, . \tag{5.6}$$

5.7.2 COINCIDENCE WITH AN ENSAMBLE OF SOURCES

Equation 5.6 considers a single, specific source in the sky. For an ensemble of sources of size N, the probability to see *at least* one source in coincidence with an alert is

$$P_C' = 1 - (1 - P_C)^N \, , \tag{5.7}$$

where $N = 4\pi\eta \approx 41253 \ \rho$ for a density $\eta \ \left[\mathrm{sr}^{-1}\right]$ or $\rho \ \left[\mathrm{deg}^{-2}\right]$ of sources in the sky.

The probability of the coincidence can be extended to a population of sources in case the source was already known prior to the alert. This is the case if a source belongs to a specific catalog. We can consider each possible realization of the ensamble of sources as Poisson distributed around a mean density value η times 4π (considering the full sky). The coincidence probability is given by the following weighted mean:

$$P_C'' = e^{-4\pi\eta} \sum_{N=0}^{\infty} \frac{(4\pi\eta)^N}{N!} P_C'(N) \tag{5.8}$$

$$= 1 - e^{-4\pi\eta} \sum_{N=0}^{\infty} \frac{1}{N!} \left(4\pi\eta\,(1 - P_C)\right)^N \tag{5.9}$$

$$= 1 - e^{-4\pi\eta P_C} \tag{5.10}$$

$$\approx 1 - e^{-\pi\eta\Delta\Psi^2\alpha} \tag{5.11}$$

$$\approx 1 - e^{-41253\rho\frac{\Delta\Psi^2}{4}\alpha} . \tag{5.12}$$

Considering a total number of n IceCube alerts, the probability of observing at least one coincidence needs to be corrected with an additional trial factor:

$$P_C^{\mathrm{Tot}} = 1 - (1 - P_C'')^n \tag{5.13}$$

$$\approx 1 - e^{-n\pi\eta\Delta\Psi^2\alpha} \tag{5.14}$$

$$\approx 1 - e^{-41253 n\rho \frac{\Delta\Psi^2}{4}\alpha}. \tag{5.15}$$

If a chosen value ϵ for the final significance is fixed, the requirements for the flaring source density $\alpha \cdot \eta$ can be obtained by

$$\alpha \cdot \eta \leq -\frac{\log(1-\epsilon)}{\pi n \Delta\Psi^2} \approx \frac{\epsilon}{n\pi\Delta\Psi^2}, \tag{5.16}$$

where the approximation holds for small probabilities. This yields a two dimensional parameter space for allowed source densities and flaring probabilities of the sources to assess whether the occurrence of a coincidence is significant or not.

To estimate the chance probability to see a coincidence between a neutrino alert issued by IceCube and a known source, we use here the Fermi/LAT 3FHL catalog as a template. Similar studies can be done with different catalogues. We consider here the parameter space number density vs flare probability (see Fig. 5.14). The background diagonal lines represent different levels of significance. We note that the number density of the Fermi/LAT catalog depends on the energy flux by different orders of magnitudes (see Fig. 5.13). Parameters used to perform the calculation on the 3FHL catalog are listed in Table 5.3.

$\Delta\Psi$	0.7°
P_Ω	$4.2 \cdot 10^{-5}$
P_{Flare}	0.03
$\rho_{\mathrm{TXS0506+056}}$	$2.5 \cdot 10^{-3}$
ρ_{3FHL}	$[2.5 \cdot 10^{-4}, 4.5 \cdot 10^{-3}]$
n	10

Table 5.3: List of quantities used to calculate the Coincidence Probability for the 3FGL(*left*) and the 3FHL(*right*) catalogues.

5.7.3 DISCUSSION

The first result here provided is the range of chance probabilities for the coincidence between one IceCube alert among $n = 10$ alerts issued and one generic source in a catalogue (3FHL). The flare probability is left floating in this generic scenario. This can be eventually refined with detailed population studies. For a source flaring few percent of the time the random chance probability is in the range of 2-3 σ. The second result here provided is the chance probability for the coincidence between one IceCube alert among the $n = 10$ alerts issued and a source with similar properties to the TXS 0506+056. This coincidence happens with a probability of $\sim 3\sigma$. This result is in good agreement with the assessment of the same probability with more detailed methods by the multi-collaboration analysis [3]. It can be concluded that this simple method can be used as a quick and stable first-guess estimator of the significance of a coincidence.

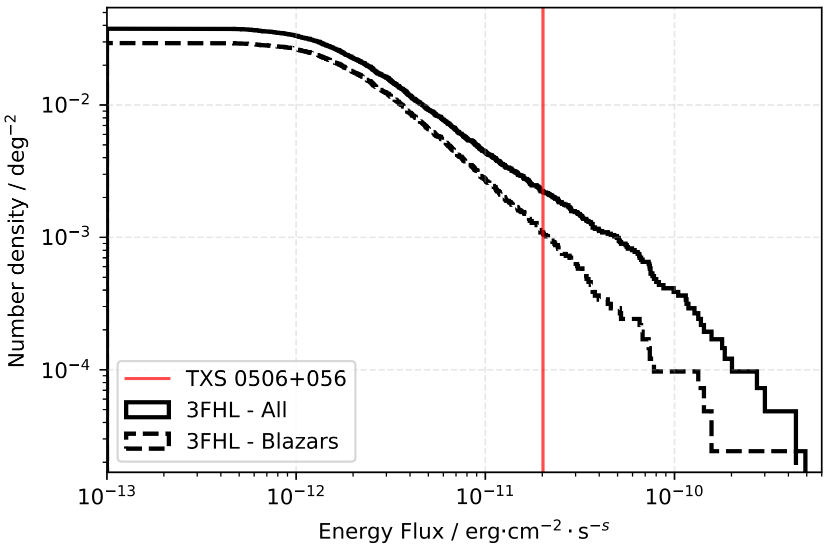

Figure 5.13: Number densities of the sources in the 3FHL catalog. The solid line represents the whole catalogue, while the dashed line shows only the blazars. The red vertical line is placed at the quoted steady state flux of the TXS 0506+056.

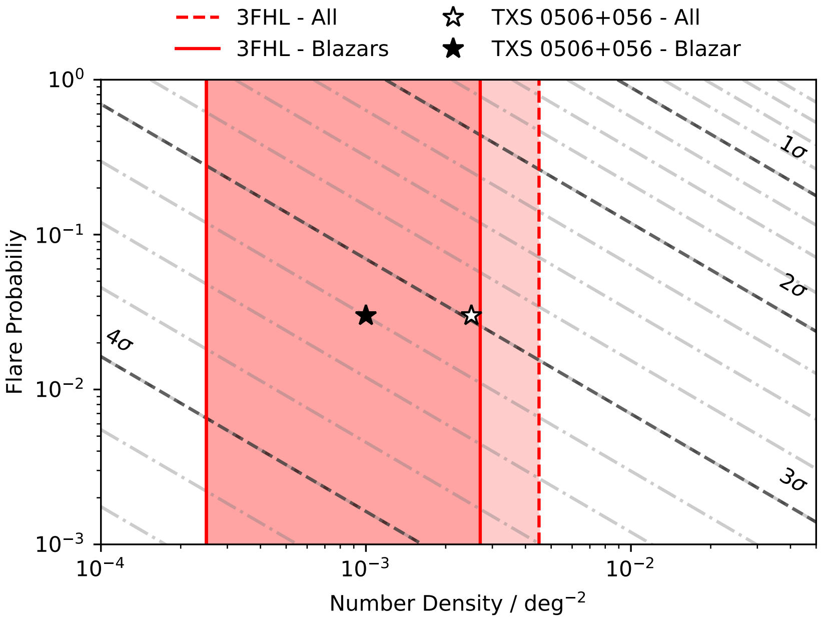

Figure 5.14: Probability density in the space source number density vs flare probability for the 3FHL catalog. The star represents the probability of having seen one IceCube alert in space-time coincidence with an object similar to the TXS 0506+056 and with a chosen characteristics flaring rate of 3%. The shaded area represents the area covered by the number density of the catalog.

6

Connecting the three messengers

This Chapter presents the most recent results on a test developed to connect the three different messengers: neutrinos, γ-rays and UHECR. In the first sections I describe the two observatories (Pierre Auger and Telescope Array) that register CR at the highest energies. Their publicly available data is used for the analysis. The statistical method for looking for correlation between the three different messengers is then presented in details. Finally, the results obtained with the most recent data publicly available are reported. This work has been done in collaboration with E. Resconi, P. Padovani, P. Giommi, Y.L. Chang and B. Arsioli and part of it has been presented at the the 35th International Cosmic Ray Conference.

6.1 ULTRA HIGH ENERGY COSMIC RAYS TELESCOPES

6.1.1 THE PIERRE AUGER OBSERVATORY

The Pierre Auger Observatory (PAO) [127] is an hybrid detector system located in Argentina, which employs two independent methods to detect and study high-energy cosmic rays. One part of the telescope consists of a surface array made of 1660 water Cherenkov stations, spaced in a triangular grid over an area of approximately 3000 km^2. The single station incorporates three photomultipliers into a water tank. They record the Cherenkov light of charged particles passing through the water contained in the tank and are also sensitive to high-energy photons converting in electron-positron pairs. The second part of the observatory consists of a fluorescence detector, which can follow the development of the shower in the atmosphere thanks to the fluorescence produced by the nitrogen molecules in the atmosphere. The fluorescence detector is made of 24 telescopes located at four different locations around the surface detector, orientated facing in. The fundamental feature of such an hybrid detector is to observe a single event with two simultaneous and idependent techniques: the fluorescence telescopes image the development of the air-shower and the surface detector measures the interaction of the shower particles once they reach the ground. Even though the fluorescence detector can operate only on clear, dark nights, the surface detector has a 100% duty cycle. Additionally, it can take advantage of the measurements done in combination with the fluorescence detector in order to have a better calibration even when operating alone. The performances of the hybrid detector are estimated at an 8% energy resolution and a 0.6° angular resolution for the reconstruction of cosmic-ray events at energies larger than $3 \cdot 10^{18}$ eV, where the detector is at full efficiency.

6.1.2 The Telescope Array Observatory

The Telescope Array (TA) observatory [128] is an hybrid detector system that consists of a surface detector and a fluorescence detector similar to PAO. The experiment is located in Utah (USA) providing an observatory in the northern hemisphere with a complementary role to what PAO is for the southern hemisphere. The surface detector covers an area of 762 km^2 with 576 scintillator detectors disposed on a square grid at 1.2 km of distance each. Scintillators have been chosen over Cherenkov water tanks because of the smaller systematic error in the determination of the primary energy, resulting in an efficiency of 100% at 10^{19} eV energies. The fluorescence detector consists of three stations facing inwards, over the area covered by the surface detector. Each station is equipped with 12-14 telescopes. The operating principles of the hybrid detector are the same as the ones described in Section 6.1.1.

6.2 Ultra High Energy Cosmic Ray Data

The PAO and TA observatories collected multiple UHECR events over the years, producing a sample of the cosmic rays with the highest energies ever obseved. This public sample consists of 340 events of which 231 have been measured by PAO above $52 \cdot 10^{18}$ eV, and 109 measured by TA above $57 \cdot 10^{18}$ eV [129, 130]. Multiple tests on these samples provided indications of small scale anisotropies in the UHECR sky at the level of 2-3 sigma when allowing a deflection of the cosmic rays of 20°. A more recent analysis presents the observation of a large scale anisotropy in the arrival direction of cosmic rays with energies higher than $8 \cdot 10^{18}$ eV [19], but no counterparts have been observed yet. Multiple indications of correlation with different populations of extragalactic γ-ray sources have also been recently discussed [131]. The significances obtained with a likelihood ratio test comparing an isotropic sky to different catalogs of sources range from 2 to 4 sigmas for different catalogs, namely a 2.7σ post-trial p-value is observed for the 2FHL catalog for events with energies larger than $60 \cdot 10^{18}$ eV. The IceCube, PAO and TA collaborations have also performed multiple tests to investigate the possibility of a neutrino-UHECR correlation. A possible correlation has been presented at the significance level of 2.3σ [132]. This significance does not seem to grow with the addition of new data, leaving still open all the questions regarding a possible joint production of UHECR and neutrinos.

6.3 The counterpart method with three messengers

The statistical method used to assess a possible correlation between neutrino-selected sources and UHECR has been developed on the basis of the technique described in Section 5.2. The number of UHECR events with at least one catalog object at an angular distance closer than θ is counted. The value of θ corresponds here to an angular uncertaintainty on the directional reconstruction of the UHECR event. Since its evaluation is extremely complex due to the deflection by magnetic fields of a cosmic ray particle, a scan at angular distances going from 1° to 30° at 1° steps is performed. The mathematical expression of the test is the following

$$n^{CR}_{w/\nu}(i, \theta) = \sum_{CR} \Theta \left(\sum_{\gamma \in \mathcal{S}_i} \sum_{\nu} \Theta \left(\sigma_\nu - \psi_{\gamma,\nu} \right) \Theta \left(\theta - \psi_{\gamma,CR} \right) \right), \tag{6.1}$$

where the sums are performed over all the events in the UHECR sample (CR), all the sources that belong to the sub-group $\mathcal{S}_i$ of the γ-ray catalog (γ) and all the events in the neutrino sample (ν). As done in the counterpart method, each subsample is created by selecting all the sources of the catalog that have a flux larger than a specific threshold. The variable ψ indicates the angular distance between one UHECR (neutrino) event and a source. The neutrino angular uncertainty corresponds to σ_ν. The function $\Theta(x)$ is the Heaviside step-function. The counting is then repeated by selecting only the sources that do not have a neutrino correlation:

$$n^{CR}_{w/o\ \nu}(i,\theta) = \sum_{CR} \Theta\left(\sum_{\gamma\in\mathcal{S}_i}\sum_{\nu} \Theta\left(\psi_{\gamma,\nu} - \sigma_\nu\right)\Theta\left(\theta - \psi_{\gamma,CR}\right)\right). \tag{6.2}$$

A Test Statistic is then defined as a likelihood ratio test between the two hypothesis

$$\Lambda = \frac{P\left(n^{CR}_{w/\nu}(i,\theta)\right)}{P\left(n^{CR}_{w/o\ \nu}(i,\theta)\right)} \tag{6.3}$$

As done for the counterpart analysis with γ-ray sources and neutrinos, the results of the test are trial corrected by using the distribution obtained from random scramblings of the sky, as described in Section 5.2.

6.4 RESULTS

The results of the counterpart method with three messengers are presented here for two different catalogs of γ-ray sources, in parallel to what has been done in Chapter 5. The two catalogs considered are the 3FHL and the 3HSP. As also described in Chapter 5, objects lying closer than 10° to the Galactic Plane are removed to avoid the influence of the galaxy in the determination of the characteristics of the sources. A similar analysis [54] has been performed with smaller neutrino and UHECR data samples on different γ-ray catalogs (2FHL, 2WHSP, 3LAC). These previous analysis showed an intriguing hint of a correlation between sources of the HBL type and the other two messengers. We follow this first hint here.

6.4.1 3FHL CATALOG

Figure 6.1 presents the p-values obtained by the scan in flux applied to the different population of sources of the 3FHL catalog, which are represented with different colours. Figure 6.2 shows the p-values for the scans in the θ angle opening. Finally, Figure 6.3 shows the results of the likelihood ratio test introduced in Eq. 6.3. The final trial corrected p-values obtained from the likelihood ratio test are reported in Table 6.1. A skymap showing both neutrinos correlating with γ-ray sources and UHECR is showed in Figure 6.4 for the HBL objects of the catalog.

Source Class	Λ p-value
All Sources	0.30
Blazar	0.25
HBL	0.10
Non-Blazar	0.27

Table 6.1: Summary of the counterpart analysis with three messengers on the 3FHL catalog. The analysis is p erformed separately on the different classes of sources, identified after the manual fit of ν peak [121]. P-values are trial corrected for testing multiple partitions of the catalog. Calculations are performed on sets of 5000 backgroud-like sky realization.

CASCADES VS. TRACKS

This section presents the the same results of the previous one, focusing on the differences between events with cascade-like and track-like topology. Figure 6.5 and 6.7 presents the p-values of the scan in flux, and Figure 6.6 and 6.8 are the corresponding values from the scan in θ angle for cascade-like and track-like events respectively. The final trial corrected p-values obtained from the likelihood ratio test are reported in Table 6.2.

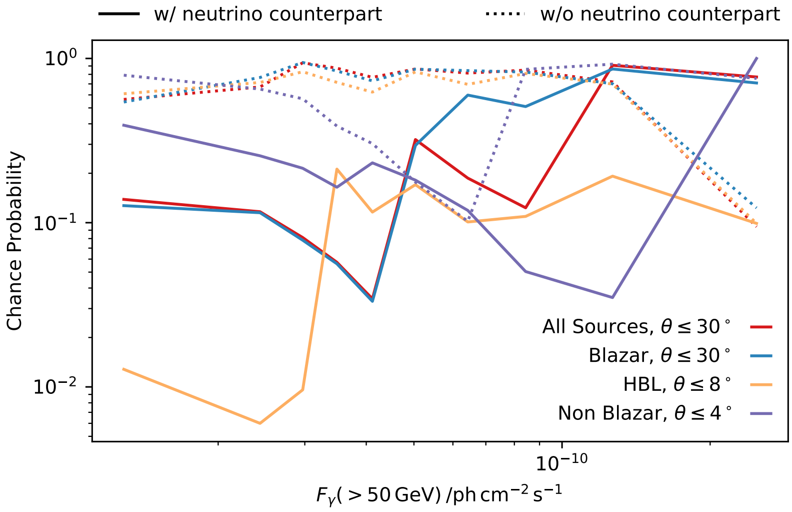

Figure 6.1: P-values resulting from the counterpart method with three messengers applied to different populations of sources (different colors) from the 3FHL catalog. The scan in flux is here presented. A solid line represents the result obtained from the sources with a neutrino counterpart, while a dotted line represents the result obtained from the sources without a counterpart.

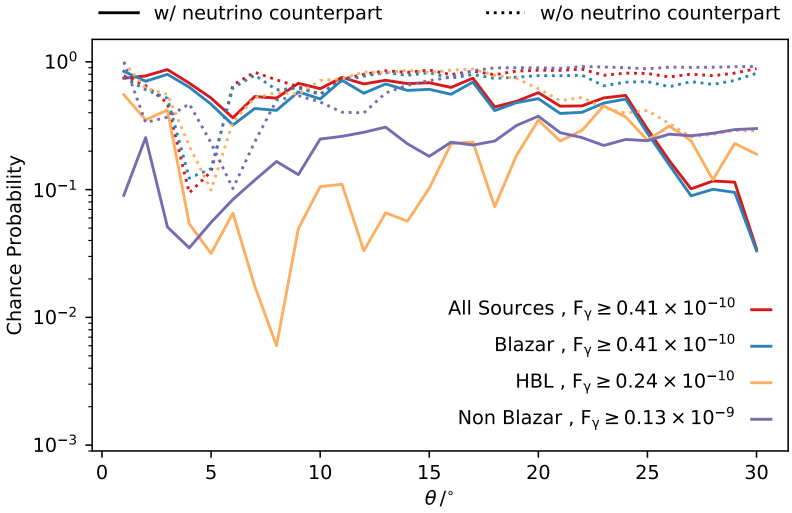

Figure 6.2: P-values resulting from the counterpart method with three messengers applied to different populations of sources (different colors) from the 3FHL catalog. The scan in θ is here presented. A solid line represents the result obtained from the sources with a neutrino counterpart, while a dotted line represents the result obtained from the sources without a counterpart.

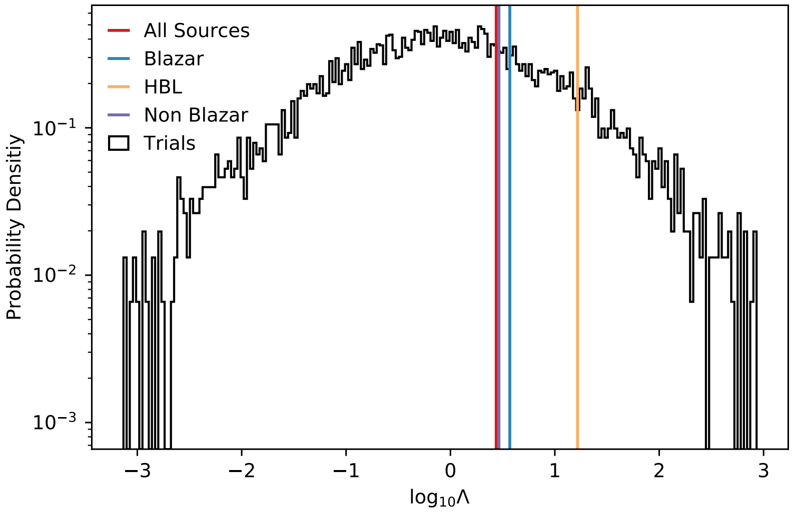

Figure 6.3: Example of the likelihood ratio test results for the 3FHL catalog. The values for different sources types are represented with vertical coloured lines. The black line histogram represents the distribution of background-like random trials.

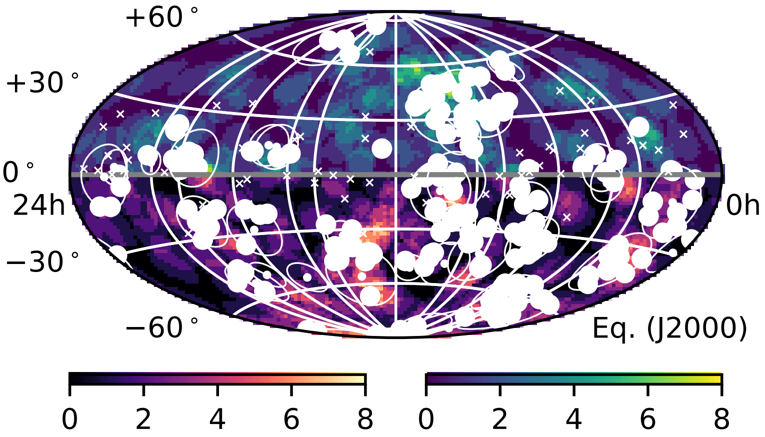

Figure 6.4: Skymap of 3FHL sources of HBL type positions (white and grey dots), neutrinos (cascade-circles and tracks-crosses) and UHECRs arrival directions (color scale). The objects of the 3FHL catalog belong to the catalog partition which provides the most significant p-value in the scan. White dots represent sources with a neutrino counterpart. Only the neutrino events with a γ-ray counterpart are illustrated. UHECRs from the northern and southern hemispheres are shown with different color to highlight the origin from different experiments, the skymap is drawn using the θ angle which provides the most significant p-value in the scan.

Source Class	Λ p-value Cascades	Λ p-value Tracks
All Sources	0.71	0.09
Blazar	0.71	0.08
HBL	0.31	0.02
Non-Blazar	0.27	0.17

Table 6.2: Summary of the counterpart analysis with three messengers on the 3FHL catalog performed separately on track-like and cascade-like neutrino events. The analysis is performed separately on the different classes of sources, identified after the manual fit of ν peak [121]. P-values are trial corrected for testing multiple partitions of the catalog. Calculations are performed on sets of 5000 backgroud-like sky realization. Trial correction is applied.

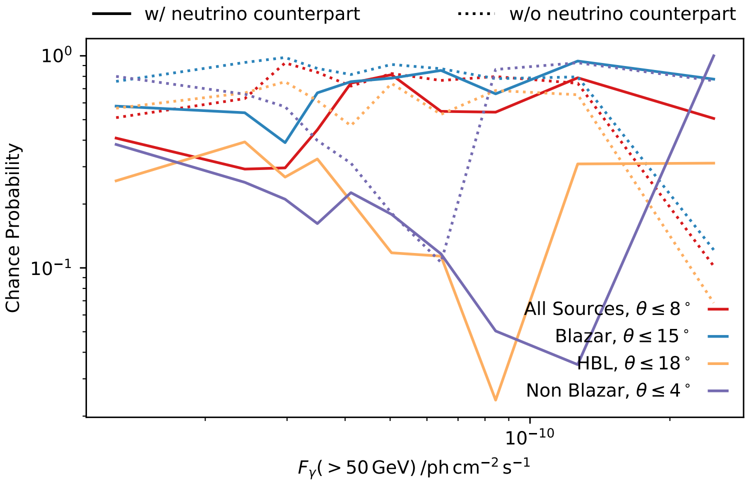

Figure 6.5: P-values resulting from the counterpart method with three messengers applied to different populations of sources (different colors) from the 3FHL catalog. The scan in flux is here presented. A solid line represents the result obtained from the sources with a neutrino counterpart, while a dotted line represents the result obtained from the sources without a counterpart. Only neutrinos with a cascade-like topology are used.

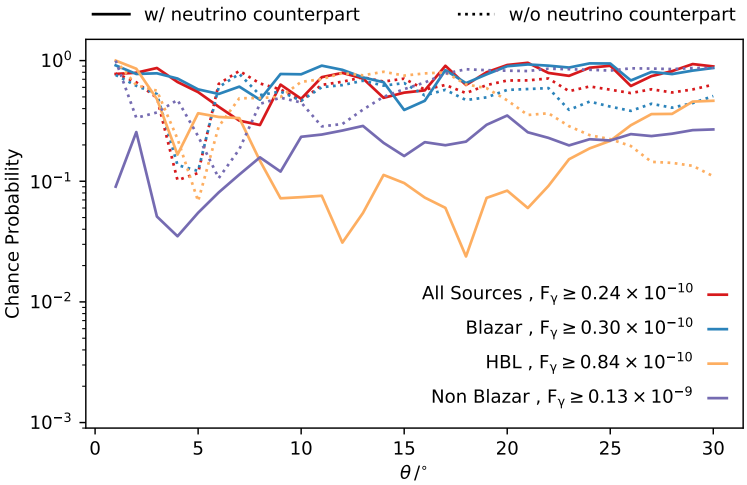

Figure 6.6: P-values resulting from the counterpart method with three messengers applied to different populations of sources (different colors) from the 3FHL catalog. The scan in θ is here presented. A solid line represents the result obtained from the sources with a neutrino counterpart, while a dotted line represents the result obtained from the sources without a counterpart. Only neutrinos with a cascade-like topology are used.

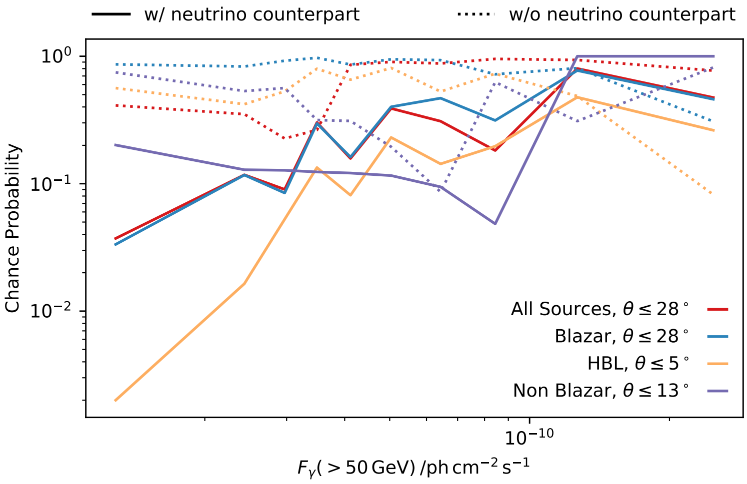

Figure 6.7: P-values resulting from the counterpart method with three messengers applied to different populations of sources (different colors) from the 3FHL catalog. The scan in flux is here presented. A solid line represents the result obtained from the sources with a neutrino counterpart, while a dotted line represents the result obtained from the sources without a counterpart. Only neutrinos with a track-like topology are used.

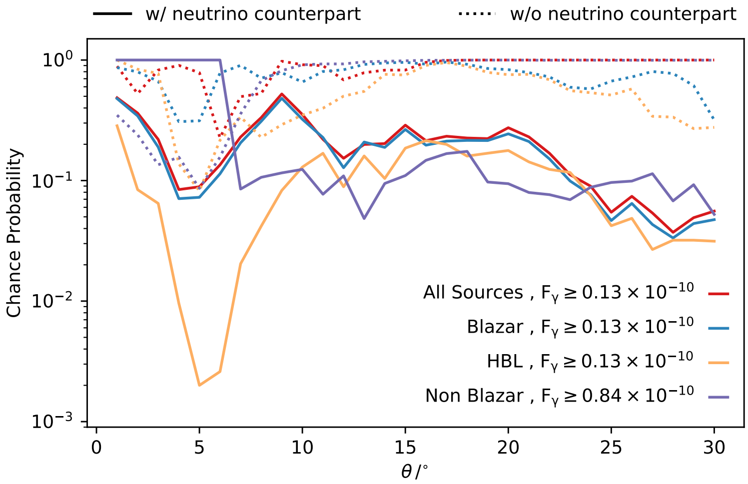

Figure 6.8: P-values resulting from the counterpart method with three messengers applied to different populations of sources (different colors) from the 3FHL catalog. The scan in θ is here presented. A solid line represents the result obtained from the sources with a neutrino counterpart, while a dotted line represents the result obtained from the sources without a counterpart. Only neutrinos with a track-like topology are used.

DISCUSSION

As expected from the preliminary steps illustrated in Chapter 5, the results here presented show a decrease in significance from the similar analysis performed in [54] on the 2FHL catalog. Nevertheless, the outcome confirms the hints of a correlation between UHECR and γ-ray sources of the HBL type selected using the neutrino events measured by IceCube. The significance of this correlation can be quantified with a p-value of 0.10, from sources with $F_{\gamma}(> 50\mathrm{GeV}) \leq 2.4^{-11}\,\mathrm{ph\,cm^{-2}s^{-1}}$, and for a $\theta = 8^{\circ}$. When performing the analysis separately for track-like and cascade-like events, it is interesting to notice that the first events from with track topology start to correlate with the most faint sources, similarly to what showed in Chapter 5 for the 3HSP catalog. In addition to the increase in statistics, this fact might explain why track-like events were not correlating with the objects of the 2FHL catalog, which have been selected at an higher luminosity. As discussed in Chapter 5, in parallel to the increase in significance from track-like events, the discriminating power of cascade-like events seems to behave as expected and it starts to decrease when UHECR are included in the analysis. An update in the analysis algorithm, possibly including a form of neutrino-dependent weighting for the γ-ray objects selected by the neutrinos seems therefore necessary for the next iterations of the analysis. The effects of the increase in statistics of the UHECR data seems to have minor effects. For the future steps of the analysis, an update in the treatment of the θ angle of the events will be possible only when more information about the single events, *e.g.* composition studies, and about the effects of the extra-galactic and galactic magnetic fields will be available.

6.4.2 3HSP CATALOG

Figure 6.10 presents the p-values obtained by the scan in flux applied both to the 3HSP Catalog as a whole, and only on the sources detected in the γ-ray band. Figure 6.11 shows the same p-values for the scan in the θ angle. Figure 6.12 shows the results of the likelihood ratio test introduced in Eq. 6.3. The final trial corrected p-values obtained from the likelihood ratio test are reported in Table 6.3 for all the sources of the catalog and only for the sources with associated γ-ray detection. A skymap showing both neutrinos correlating with γ-ray sources and UHECR is showed in Figure 6.9.

Source Type	Λ p-value
All Sources	0.11
Sources w/ γ-ray	0.05

Table 6.3: Summary of the counterpart analysis with three messengers on the 3FHL catalog. The analysis is p erformed separately on the full catalog and only on sources with γ-ray detection. Calculations are performed on sets of 5000 backgroud-like sky realization.

CASCADES VS. TRACKS

A more in depth check of the differences between cascade-like and track-like events is also performed for the 3HSP catalog. Figure 6.13 and 6.15 presents the p-values of the scan in flux, and Figure 6.14 and 6.16 are the corresponding values from the scan in θ angle for cascade-like and track-like events respectively. Additionally, the results of the same analysis performed using track-like neutrino events with an angular uncertainty increased by 30% are reported in Figure 6.17 and 6.18. The final trial corrected p-values obtained from the likelihood ratio test are reported in Table 6.4

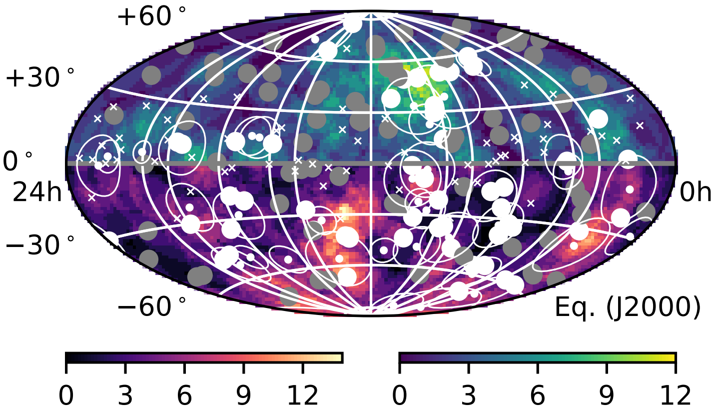

Figure 6.9: Skymap of 3HSP sources positions (white and grey dots), neutrinos (cascade-circles and tracks-crosses) and UHECRs arrival directions (color scale). The objects of the 3HSP catalog belong to the catalog partition which provides the most significant p-value in the scan. White dots represents sources with a neutrino counterpart, grey dots sources with no counterpart. Only the neutrino events with a γ-ray counterpart are illustrated. UHECRs from the northern and southern hemispheres are shown with different color to highlight the origin from different experiments, the skymap is drawn using the θ angle which provides the most significant p-value in the scan.

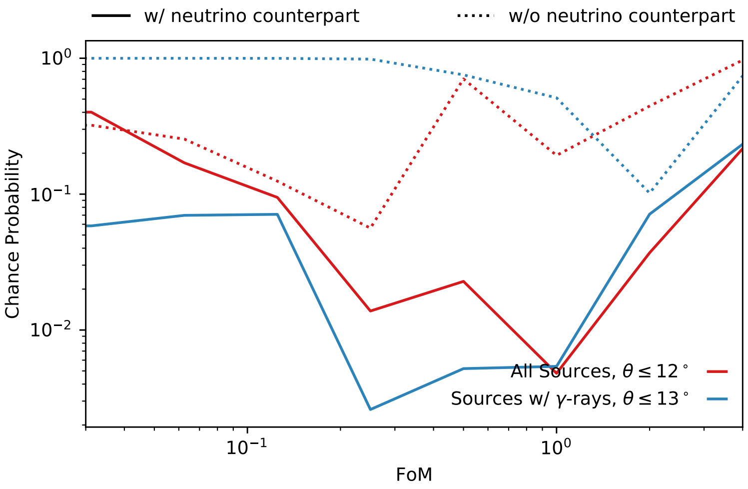

Figure 6.10: P-values resulting from the counterpart method with three messengers applied to the 3HSP catalog. The scan in FoM is here presented. A solid line represents the result obtained from the sources with a neutrino counterpart, while a dotted line represents the result obtained from the sources without a counterpart. The red line represents the analysis performed on the whole catalog, while the blue line only considers objects with have been detected in the γ-ray band.

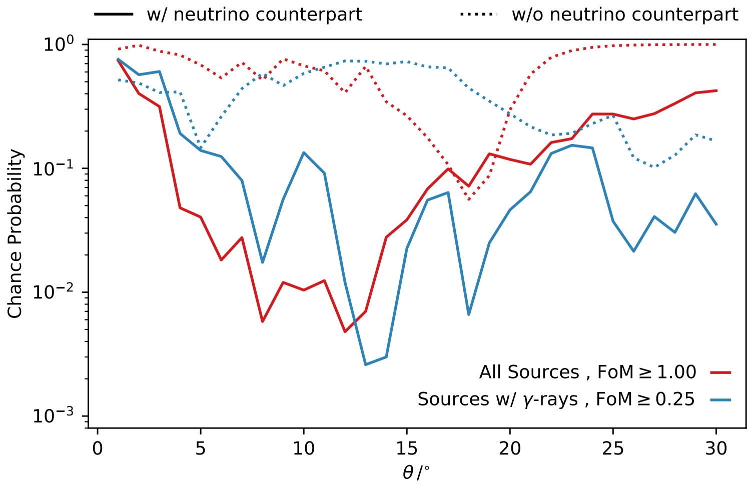

Figure 6.11: P-values resulting from the counterpart method with three messengers applied to the 3HSP catalog. The scan in θ is here presented. A solid line represents the result obtained from the sources with a neutrino counterpart, while a dotted line represents the result obtained from the sources without a counterpart. The red line represents the analysis performed on the whole catalog, while the blue line only considers objects with have been detected in the γ-ray band.

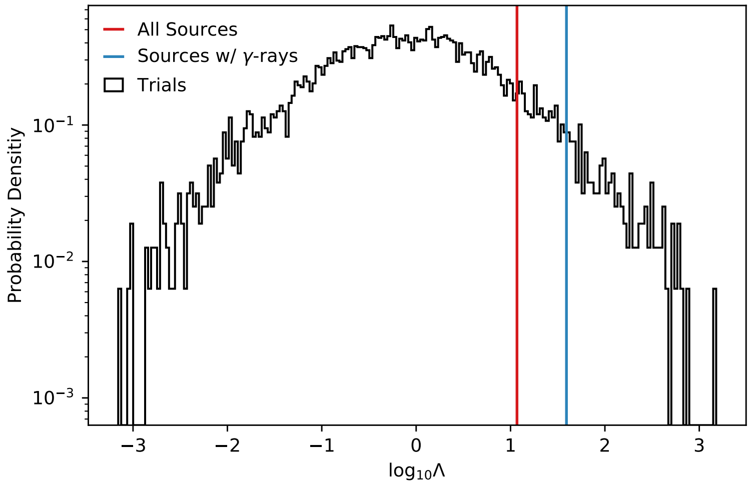

Figure 6.12: Example of the likelihood ratio test results for the 3HSP catalog. The values for different sources types are represented with vertical coloured lines. The black line histogram represents the distribution of background-like random trials. The red line represents the analysis performed on the whole catalog, while the blue line only considers objects with have been detected in the γ-ray band.

Source Type	Λ p-value Cascades	Λ p-value Tracks	Λ p-value Tracks - Larger Uncertainty
All Sources	0.34	0.12	0.15
Sources w/ γ-ray	0.27	0.19	0.14

Table 6.4: Summary of the counterpart analysis with three messengers on the 3FHL catalog. The analysis is performed separately on the full catalog and only on sources with γ-ray detection. Calculations are performed on sets of 5000 backgroud-like sky realization. Trial correction is applied.

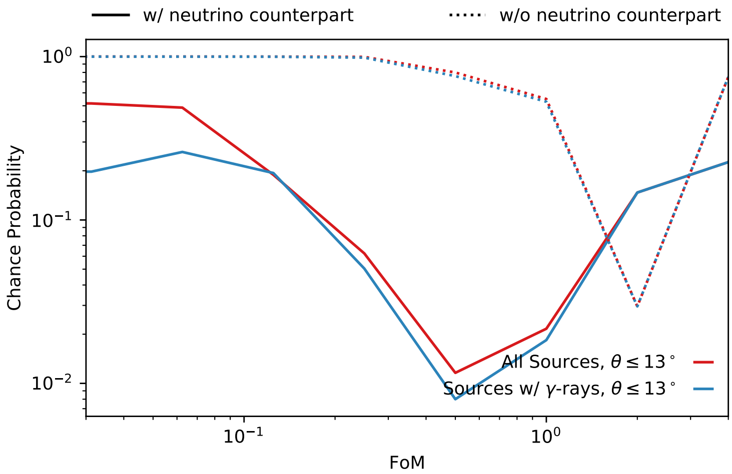

Figure 6.13: P-values resulting from the counterpart method with three messengers applied to the 3HSP catalog. The scan in FoM is here presented. A solid line represents the result obtained from the sources with a neutrino counterpart, while a dotted line represents the result obtained from the sources without a counterpart. The red line represents the analysis performed on the whole catalog, while the blue line only considers objects with have been detected in the γ-ray band. Only neutrinos with a cascade-like topology are used.

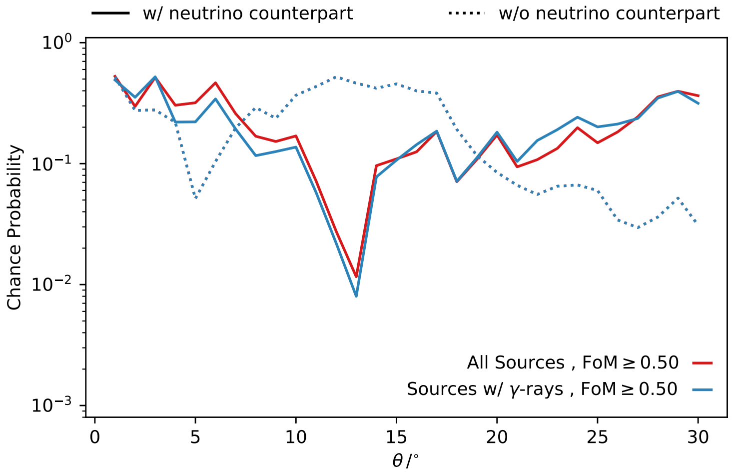

Figure 6.14: P-values resulting from the counterpart method with three messengers applied to the 3HSP catalog. The scan in θ is here presented. A solid line represents the result obtained from the sources with a neutrino counterpart, while a dotted line represents the result obtained from the sources without a counterpart. The red line represents the analysis performed on the whole catalog, while the blue line only considers objects with have been detected in the γ-ray band. Only neutrinos with a cascade-like topology are used.

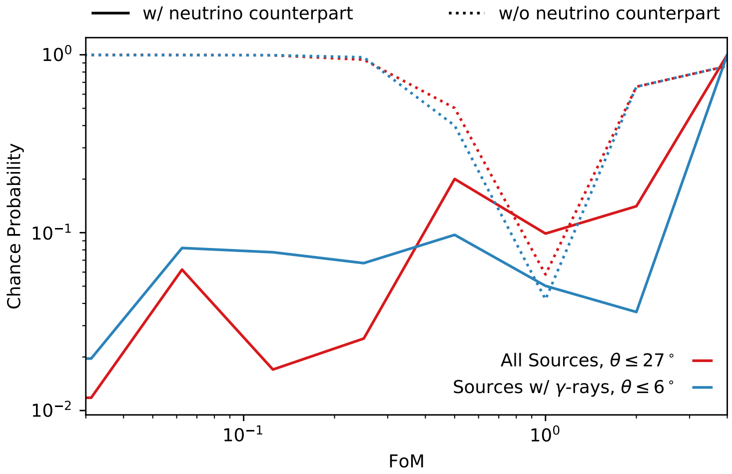

Figure 6.15: P-values resulting from the counterpart method with three messengers applied to the 3HSP catalog. The scan in FoM is here presented. A solid line represents the result obtained from the sources with a neutrino counterpart, while a dotted line represents the result obtained from the sources without a counterpart. The red line represents the analysis performed on the whole catalog, while the blue line only considers objects with have been detected in the γ-ray band. Only neutrinos with a track-like topology are used.

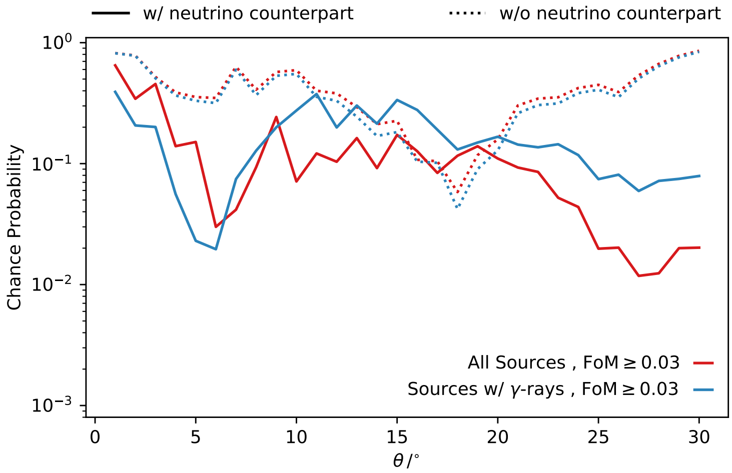

Figure 6.16: P-values resulting from the counterpart method with three messengers applied to the 3HSP catalog. The scan in θ is here presented. A solid line represents the result obtained from the sources with a neutrino counterpart, while a dotted line represents the result obtained from the sources without a counterpart. The red line represents the analysis performed on the whole catalog, while the blue line only considers objects with have been detected in the γ-ray band. Only neutrinos with a track-like topology are used.

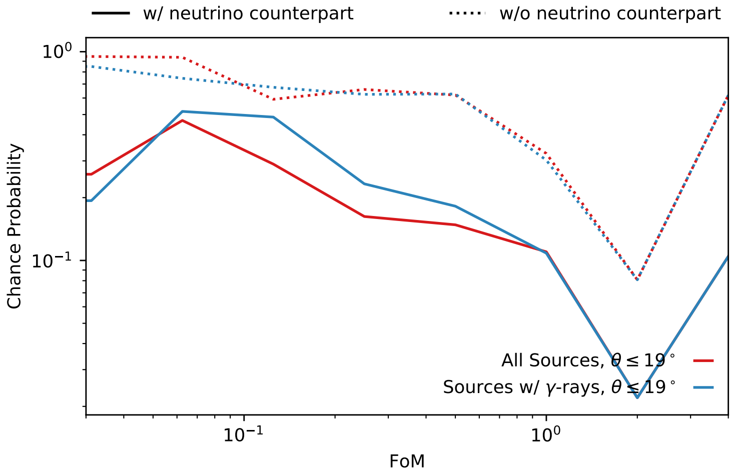

Figure 6.17: P-values resulting from the counterpart method with three messengers applied to the 3HSP catalog. The scan in FoM is here presented. A solid line represents the result obtained from the sources with a neutrino counterpart, while a dotted line represents the result obtained from the sources without a counterpart. The red line represents the analysis performed on the whole catalog, while the blue line only considers objects with have been detected in the γ-ray band. Only neutrinos with a track-like topology are used and the angular uncertainty is increased by 30%.

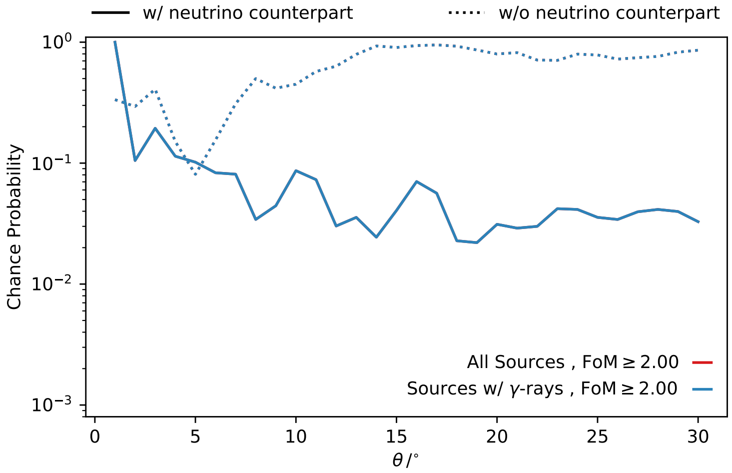

Figure 6.18: P-values resulting from the counterpart method with three messengers applied to the 3HSP catalog. The scan in θ is here presented. A solid line represents the result obtained from the sources with a neutrino counterpart, while a dotted line represents the result obtained from the sources without a counterpart. The red line represents the analysis performed on the whole catalog, while the blue line only considers objects with have been detected in the γ-ray band. Only neutrinos with a track-like topology are used and the angular uncertainty is increased by 30%.

6.5 DISCUSSION

The results of the analysis on the 3HSP catalog show a slight reduction in significance when compared to the analysis performed on the 2WHSP catalog in [54]. A trial corrected p-value of 0.05 is observed from sources with a FoM ≤ 0.25 at a $\theta = 13°$. Interestingly, the intuitive scenario in which the significance is higher for the objects which have been observed in the γ-ray band is confirmed. The analysis performed on track and cascade-like neutrino events separately provides less significant results when compared to the complete neutrino sample, and of comparable significance between the two topologies. The only difference is that track-like events correlate at the highest significance with faint sources within in the first bin of the FoM scan (FoM≤ 0.03), while cascade-like events correlate with objects approximately ten times more likely to be detected in γ-rays (FoM≤ 0.5). This can also explain why the cascades give a more significant correlation with sources already detected in the γ-ray band, while tracks present a smaller p-value by using the whole 3HSP catalog. The exercise of increasing the neutrino angular uncertainty provides the interesting result of selecting objects with FoM≤ 2.0, where there is no difference between the two partitions of the catalog. The number of objects at this FoM is very low, providing a low level significance as a final result.

7

AGN Outflows as Neutrino sources

The first quantitative test aimed at connecting astrophysical neutrinos from the IceCube experiment and AGN outflows is presented in this chapter. The statistical analysis relies on the method described in chapter 5. The process of selection of the objects charachterised as AGN outflows is presented in the next sections, together with the results of the test and an outlook for future analyses. The work described in this chapter has been done in collaboration with P. Padovani and E. Resconi and has been published in *P. Padovani, A. Turcati, and E. Resconi. AGN outflows as neutrino sources: an observational test. Monthly Notices of the Royal Astronomical Society, 477(3):3469–3479, 2018*[116].

7.1 AGN Outflow catalogs

Two different sets of objects presenting evidence of AGN outlflows have been selected for the analysis. Each one of the two sets presents unique features, allowing to perform two different tests in a complementary way.

7.1.1 The AGN outflow list

In order to study the scaling relations between AGN, the host galaxy an the outflows, the authors of [72] created the first list of objects with outflow detection. From literature, they put together a list of 94 AGN with confirmed massive outflows observations, for which there is an estimate on the physical size of the high velocity gas in the wind. The sample suffers from strong selection biases, different for various types of outflows, and it is by no mean complete, not qualifying to be called a catalog. Among these effect, molecular winds and ultrafast outflows (UFOs) can only be studied at $z \lesssim 0.2$, ionised winds are found both at low-redshift and at $z \sim 2-3$, while broad absorption line (BAL) sources are at $z \sim 2-3$. This list is not complete enough to permit robust statistical studies, but it can be complemented by the SDSS catalog presented in the next subsection.

7.1.2 The SDSS catalog

This catalog consists of a total of 23,264 AGN at $z < 0.4$ selected from the Sloan Digital Sky Survey (SDSS) DR7 database [133]. For each object the [O III] $\lambda 5007$ line profiles have been measured, which can be used to determine the kinematic properties of the emittng gas. Using the available data, the [O III] $\lambda 5007$ flux-weighted average full width half-maximum ($\mathrm{FWHM}_{\mathrm{Avg}}$) has been calculated using the following expression:

$$\mathrm{FWHM_{Avg}} = \sqrt{(\mathrm{FWHM_{broad}}\,F_{\mathrm{broad}})^2 + (\mathrm{FWHM_{narr}}\,F_{\mathrm{narr}})^2}, \qquad (7.1)$$

where F_{broad} and F_{narr} are the fractional fluxes contained within the two fitted Gaussian components of the [O III] λ5007 line, a broad and a narrow one. A $\mathrm{FWHM_{Avg}} > 500$ km s^{-1} is the standard lower limit used for the selection of follow-up targets for spectroscopic studies of AGN outflows [134]. A fraction of 17% of the sources of the SDSS catalog has a $\mathrm{FWHM_{Avg}}$ above this value, providing a large statistical sample of AGN with possible outflows. To confirm this claim, the authors of [134] presented integral field units observations of 16 objects with high $\mathrm{FWHM_{Avg}}$ belonging to the SDSS catalog, showing the presence of high-velocity outflows in all of them. Power provides another good proxy for the presence of outflows, we therefore also use the observed $L_{[\mathrm{O\,III}]}$ in [133] for the statistical study. Figure 7.1 shows the distribution of the objects of the catalog in luminosity vs. $\mathrm{FWHM_{Avg}}$.

7.2 STATISTICAL METHOD

The process of finding a counterpart for the IceCube neutrinos does not change if the putative sources are switched from blazars to AGN outflows. The statistical method developed in Section 5.2 can be used with the two source lists identified in the previous Section. Only a minimal change is necessary to accomodate the SDSS catalog: as previously discussed, the random scrambling of the neutrino right ascension values does not conserve the total area sampled by their uncertainty. If the source survey is not uniform in the sky, in order to avoid a bias, the overlapping area identified by the neutrino angular uncertainty and the portion of the sky covered by the survey must be conserved in each random realisation. Given the irregular shape in the sky of the

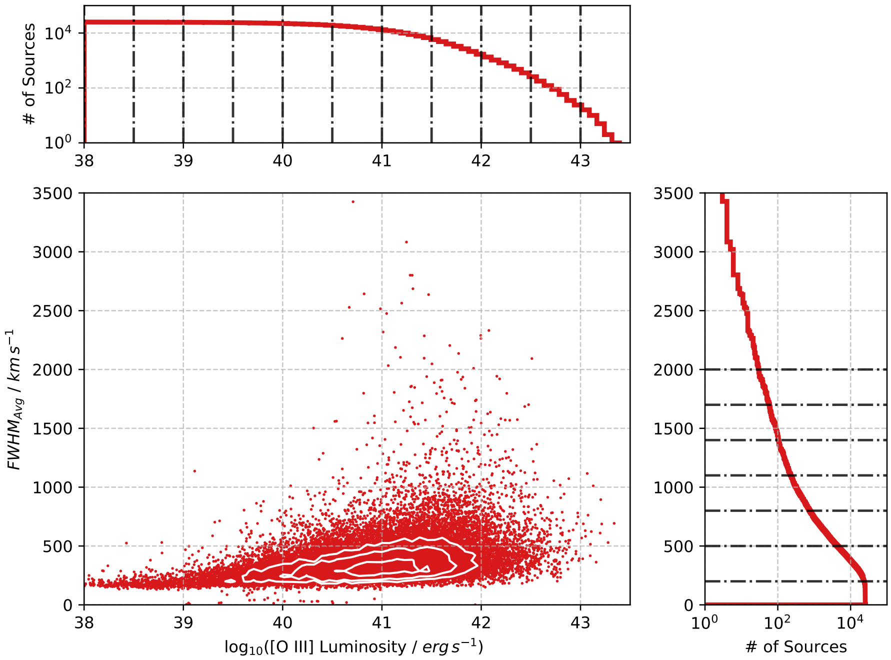

Figure 7.1: Distribution of the AGN of the SDSS catalog in $L_{[\mathrm{O\,III}]}$ (x-axis) versus $\mathrm{FWHM}_{\mathrm{Avg}}$ (y-axis). The one dimensional histograms show the cumulative distribution of the objects of the catalog in the single variable: $L_{[\mathrm{O\,III}]}$ at the top, $\mathrm{FWHM}_{\mathrm{Avg}}$ on the right.

SDSS catalog, it is not possible to fulfill this requirement neither by randomising the neutrinos in right ascension, nor by scrambling the objects of the catalog. The goal can indeed be achieved by randomising the SDSS coordinates inside the portion of the sky covered by the survey. This area has been approximated with a mask by using an HEALPix sky pixelisation with a total of 49152 pixels, each covering 0.84 square degrees. The neutrino sample is the same one identified in Section 5.3.

7.3 Results

By cross-correlating the IceCube neutrinos with the list of confirmed AGN outflows, one or multiple counterparts where identified for 15 of the events, all of cascade topology. The selected objects are 35 AGN, a detailed discussion of the objects can be found in [116]. Figure 7.2 shows the position of the AGN on the list on a skymap (blue circless), together with the IceCube neutrinos. The angular uncertainty for each neutrino event is represented by a circular line, black for the correlating events and grey for the non-correlating ones.

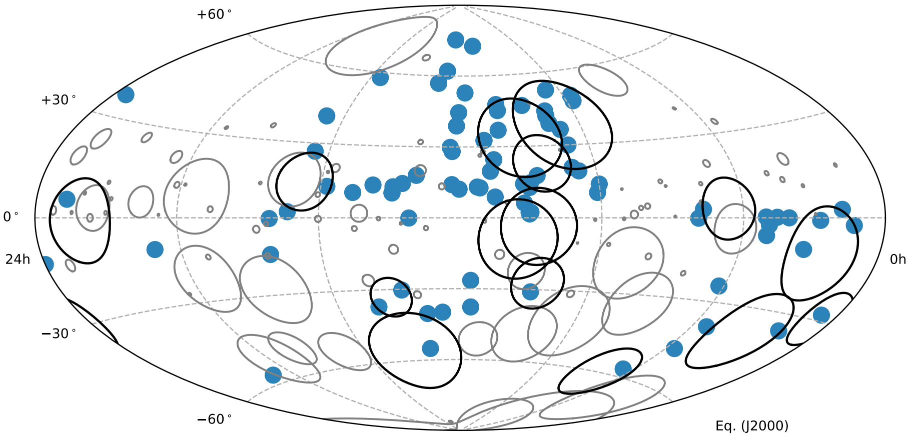

Figure 7.2: Skymap in equatorial coordinates. Blue circles indicate the position of the AGN with outflows from [72]. IceCubes events are represented as circles with radius equal to the angular uncertainty. Black circles indicate neutrinos with a counterpart, grey circles neutrinos without counterparts.

As discussed in Section 7.1.1, it is not possible to extract a meaningful statistical evaluation of the significance from this list of AGN, it is nevertheless interesting to study the characteristics of the selected objects in comparison to the non-correlated ones. Figure 7.3 shows the distribution of the kinetic power ($\frac{1}{2}\dot{M}_{OF}v_{max}^2$, where v_{max} is the maximum velocity of the outflow) for AGN outflows. The solid line indicates objects with a neutrino counterpart, while the dashed line is used for the ones without counterparts. The two distributions are significantly different [116]. The AGN outflows with IceCube counterparts show an $\dot{E}_{\mathrm{Kin}}$ larger by a factor of 7 than the corresponding value for objects without neutrino counterparts.

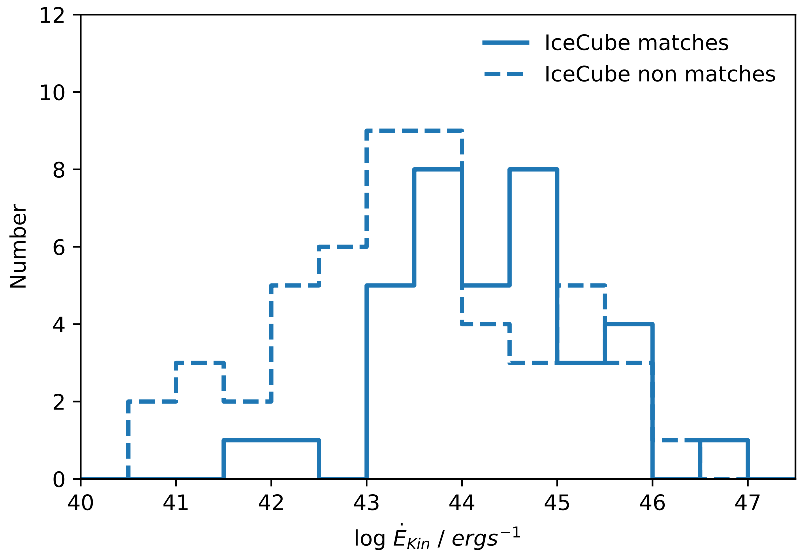

Figure 7.3: Distribution of the kinetic power for objects in the AGN outflows. The solid line indicates objects with a neutrino counterpart, while the dashed line is used for the ones without counterparts.

In a similar way, Figure 7.4 shows the distribution of $\dot{M}_{\mathrm{OF}}$ for outflows objects with a neutrino counterpart (solid line) and without (dashed line). The two distributions are again significantly different [116], showing another factor 7 separating the two. Finally, the AGN bolometric power distribution for AGN outflows with and without IceCube counterparts show only a minor difference. Objects with a neutrino counterparts have a bolometric power larger by a factor of 4 with respect to objects with no counterpart.

This interesting result has been followed up by applying the formal statistical test

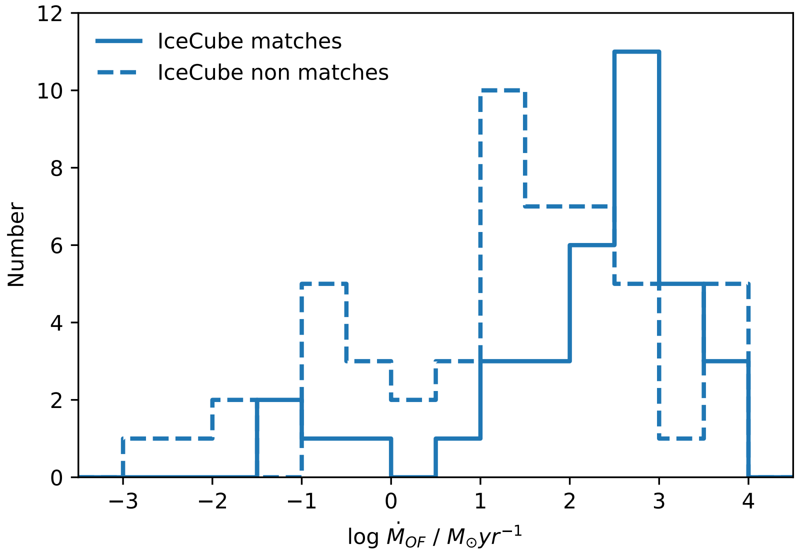

Figure 7.4: Distribution of the mass outflow rate for objects in the AGN outflows list. The solid line indicates objects with a neutrino counterpart, while the dashed line is used for the ones without counterparts.

described in Section 5.2 on the SDSS catalog. A p-value is calculated for each of the bins $\mathrm{FWHM}_{\mathrm{Avg},i}$ ($\mathrm{L}_{[\mathrm{O_{III}}],i}$), for a total of 8 (11) p-values. A trial correction is applied when reporting only the most significant p-value. Figure 7.5 shows the position on a skymap of the objects in the SDSS catalog (red dots) together with the neutrino events. The angular uncertainty for each neutrino event is represented by a circular line, black for the correlating events and grey for the non-correlating ones. IceCube events with large angular uncertainy, mostly of cascade topology, will almost always identify a counterpart due to the large density of the SDSS sources, even when the sample size is reduced with cuts. It is therefore very hard to obtain evidence of a signal from this topology.

Figure 7.6 shows the chance probability of association with IceCube neutrinos for the SDSS catalog. The catalog has been partitioned in $\mathrm{FWHM}_{\mathrm{Avg}}$. A p-value $\sim 17\%$

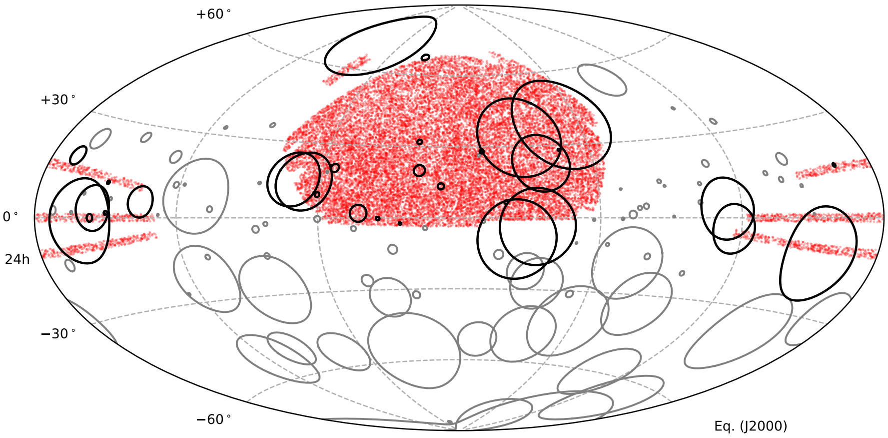

Figure 7.5: Skymap in equatorial coordinates. Red dots indicate the position of the objects of the SDSS catalog. IceCubes events are represented as circles with radius equal to the angular uncertainty. Black circles indicate neutrinos with a counterpart, grey circles neutrinos without counterparts.

is calculated for $\mathrm{FWHM}_{\mathrm{Avg}} \gtrsim 800$ km s^{-1} for track-like events. After trial correction it corresponds to $\sim 48\%$. A p-value $\sim 30\%$ is observed for $\mathrm{FWHM}_{\mathrm{Avg}} \gtrsim 2,000$ km s^{-1} for cascade-like events. After trial correction it corresponds to $\sim 60\%$. As discussed above, an evidence for signal is not expected in the cascade channel due to the large density of SDSS sources. Strong fluctuations in the p-values are nevertheless expected at large velocities due to the small statistics of the catalog partition. The partition that shows the highest significance presents 9 observed neutrino-source correspondence, while the expected number from random trials is 6.9. Since the total number of neutrinos inside the survey area is 33, this implies a contribution to the IceCube signal from AGN outflows at the 6% level.

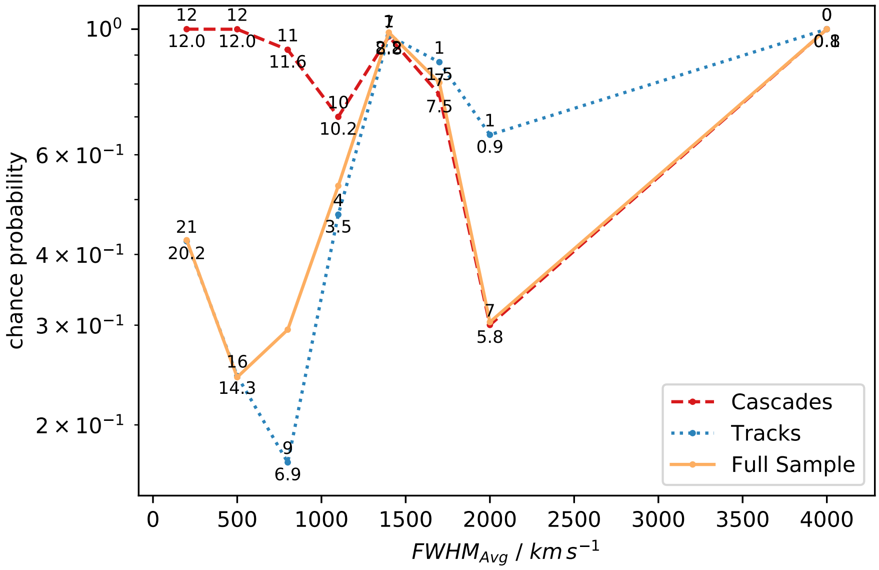

Figure 7.6: Chance probability of association of SDSS AGN for objects having $\mathrm{FWHM}_{\mathrm{Avg}}$ larger than the value on the x-axis. The complete sample of IceCube events is represented with a solid orange line, events with cascade topology with a dashed red line, and track-like events with a dotted blue line. The numbers give the observed number of counterparts (above the points) and the same value expected from random trials (below the points). A p-value ~ 17 per cent is reached for $\mathrm{FWHM}_{\mathrm{Avg}} \gtrsim 800$ km s^{-1} for tracks.

Figure 7.7 shows the chance probability of association with IceCube neutrinos for the SDSS catalog. The catalog has been partitioned in $L_{[\mathrm{O_{III}}]}$. A p-value of $\sim 37\%$ is calculated for $\log L_{[\mathrm{O_{III}}]} \gtrsim 40$ erg s^{-1} for track-like events. After trial correction it corresponds to $\sim 48\%$. A p-value $\sim 72\%$ is observed for $\log L_{[\mathrm{O_{III}}]} \gtrsim 42.5$ erg s^{-1} for cascade-like events. After trial correction it corresponds to $\sim 91\%$.

7.4 DISCUSSION

The first intriguing result of the test is that AGN with an observed outflow which are associated with IceCube neutrinos have larger $\dot{E}_{\mathrm{kin}}$, $\dot{M}_{\mathrm{OF}}$ and bolometric power with respect to objects without a neutrino counterpart. This is physically explainable

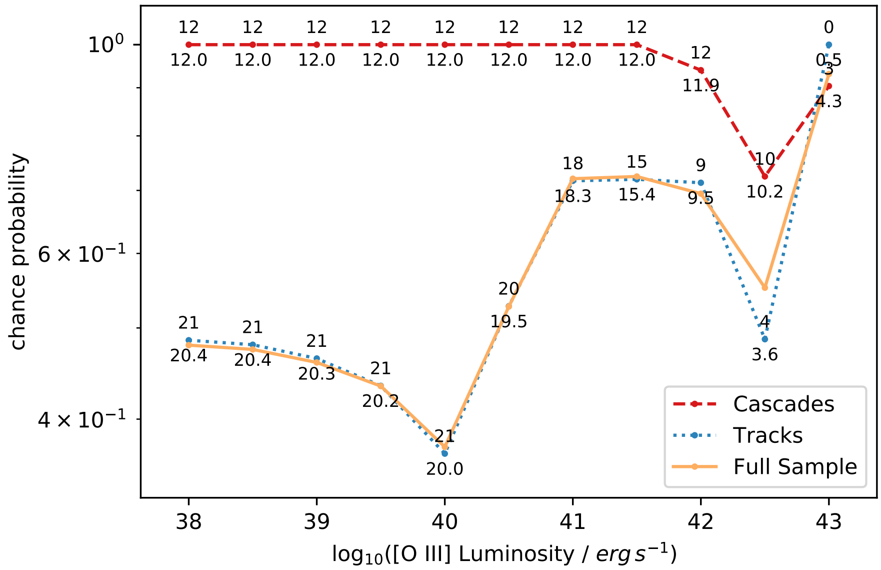

Figure 7.7: Chance probability of association of SDSS AGN for objects having $L_{[\mathrm{O\,III}]}$ larger than the value on the x-axis. The complete sample of IceCube events is represented with a solid orange line, events with cascade topology with a dashed red line, and track-like events with a dotted blue line. The numbers give the observed number of counterparts (above the points) and the same value expected from random trials (below the points). A p-value $\sim\ 37$ per cent is reached for $\log L_{[\mathrm{O\,III}]} \gtrsim 40$ erg s^{-1} for tracks.

by the fact that AGN with a larger outflow, kinetic energy rate and bolometric power are more likely to be stronger neutrino emitters [76, 78, 79].

The statistical analysis performed on the SDSS catalog does not provide additional evidence of an association between IceCube neutrinos and AGN outflows. Nevertheless, the outcome of the analysis is interesting. Infact, the value of $\mathrm{FWHM}_{\mathrm{Avg}}$ at which the highest significance is observed is above the standard limit used to select targets for follow-up studies of AGN outflows. Since only a small fraction of the objects in the SDSS catalog has a confirmed outflow, this can also partly explain the absence of a significant result.

The most likely implication of the test is that AGN outflows are not relevant in the explanation of the origin of astrophysical neutrinos. However, the results can also be explained with a lack of statistics both on the neutrino and on the source samples. AGN outflows may be a very faint type of neutrino source, making them very hard to be revealed as a point source, but still contributing to the total diffuse astrophysical flux. In this framework, this results do not support a scenario in which AGN outflows explain the full IceCube signal [76, 78], but they are still compatible with a smaller contribution [79].

8

Conclusion

From the discovery of the astrophysical diffuse neutrino flux to the very recent observation of a flaring blazar in coincidence with an extremely-high-energy neutrino event, the interest of the scientific community in using different messengers to broaden our picture of the Universe has been steadily increasing. The role of the neutrino particle in the field of multimessenger astronomy has become central in the quest of discovering the sources of cosmic rays and understanding their underlying physical processes. The inclusion of different particles brings multiple and different challenges together with the excitement for the potential of this new-born physical field.

The first step of this thesis consisted in a single-messenger analysis, using neutrinos in order to find small scale anisotropies in the extragalactic and galactic sky. The results have been negative so far, producing stringent limits for steady sources with an unbroken power-law energy spectrum. These results can be interpreted as an opportunity to broaden the horizon of the searches and consider the inclusion of a second messenger: γ-rays, in order to focus the investigation on objects that are already known emitters of high-energy particles. A first update on an analysis technique looking for counterparts of IceCube neutrinos among *Fermi*-LAT selected sources was presented in this thesis. The focus has been put into high-synchrotron-peaked blazars of the BL-Lac type. The inclusion of new statistic both in the neutrino and in the γ-ray data produced a reduction in the significance when compared to the previous tests performed on similar catalogs of sources. While identifying features of the analysis method that need to be addressed in a future iteration with increased neutrino statistics, the most likely cause of the diminished significance was identified in the neutrino data. Nevertheless, hints of the presence of many interesting objects in the proximity of neutrino events with good angular reconstruction are confirmed through a statistical test. This test also opens to the possibility that the angular uncertainty of track-like neutrino events is slightly underestimated. In a further step, UHECRs are added to the neutrinos and γ-ray sources in an updated three-messengers analysis. Additional statistics on the cosmic ray data did not change the behaviour already observed in the previous step of the analysis: a moderate reduction of the significance of the correlation between neutrino-selected high-synchrotron-peaked blazars of the BL-Lac type. This serie of results should not be interpreted as a proof of the absence of correlation between the origin of the three messengers, but as a confirmation that both the data description and the analysis algorithm have to be improved in order to provide definitive results. Different points of the analysis chain have been identified, which can lead to a positive development:

- The neutrino data can be improved by the IceCube collaboration by publicly releasing events with uniform reconstructions and a more detailed description of the angular uncertainties.

- The detailed study of specific γ-ray objects is very important to understand the characteristics of the sources that show an evidence of correlation between different messengers. Very bright γ-ray objects are not mandatory bright neutrino or UHECR emitters, thus the ideal catalog to study correlations does not exist yet.
- A better description of UHECR deflection during propagation and a more precise measurement of their composition can directly improve the statistical power of the counterpart method by making the angular scan unnecessary.
- The counterpart method itself can be improved by the development of dedicated scheme to weight the sources selected by the neutrino. The number of neutrinos selecting an object, the energy of these neutrinos, and finally the distance of their reconstructed coordinates from the position of the source as a function of the neutrino angular uncertainty can all contribute to creating a better filter. Numerous tests are nevertheless needed to identify the correct way to include this information in an unbiased way.

The final Chapter of the thesis shows the application of the same revised methods used thus far in order to experimentally test a new possible population of multimessenger emitters: AGN with ultrarelativistic outflows. This test was applied here for the first time both on a *bona fide* list of objects with measured outflows and on a catalog of objects with a very high likelihood of presenting an outflow. The results are in agreement with the most recent and stringent theoretical models and suggest that a followup with a standard stacked point-like source analysis might provide very strong limits on the model.

Acknowledgments

The work here presented would not have been possible without the support of many friends and colleagues that I would like to thank. First of all I would like to thank my supervisor, Prof. Elisa Resconi, for introducing me to the field of multi-messenger astronomy, guiding me through these past years and always encouraging me to follow my interests. It has been a pleasure to have you as an example to what it means to be a scientist. I would like to thank Paolo Padovani and Paolo Giommi for the many insightful meetings, and for always being available to share their deep knowledge in astronomy. I also want to thank Prof. Lothar Oberauer for being the second reviewer of this work, and Prof. Andreas Weiler for agreeing to be the chair of the review commission. Very special thanks go to all my colleagues, the members of the ECP group, that welcomed me in Munich and became good friends, always available for an advice and for sharing a coffee in the Coffice. In particular I would like to thank Matthias, Kai, Stefan, Imma, Theo, Stephan, Martin and Martina for being good collaborators in the office and great friends outside. I would like to thank my family, that always supported me and loved me, and especially Silvia, for being at my side every time I needed her. A final thank you goes to all my friends, that make me smile every day.

Bibliography

[1] M. G. Aartsen et al. Observation of High-Energy Astrophysical Neutrinos in Three Years of IceCube Data. *Phys. Rev. Lett.*, 113:101101, 2014.

[2] M. G. Aartsen et al. Observation and Characterization of a Cosmic Muon Neutrino Flux from the Northern Hemisphere Using Six Years of IceCube Data. *ApJ*, 833:3, December 2016.

[3] IceCube Collaboration et al. Multimessenger observations of a flaring blazar coincident with high-energy neutrino IceCube-170922A. *Science*, 361:eaat1378, July 2018.

[4] T. K. Gaisser, R. Engel, and E. Resconi. *Cosmic Rays and Particle Physics*. June 2016.

[5] Maurizio Spurio. *Particles and astrophysics: a multi-messenger approach*. Astronomy and Astrophysics Library. Springer, Cham, 2015.

[6] M. Aguilar et al. Precision Measurement of the Proton Flux in Primary Cosmic Rays from Rigidity 1 GV to 1.8 TV with the Alpha Magnetic Spectrometer on the International Space Station. *Phys. Rev. Lett.*, 114:171103, Apr 2015.

[7] Y. S. Yoon et al. Proton and Helium Spectra from the CREAM-III Flight. *The Astrophysical Journal*, 839(1):5, 2017.

[8] M. Amenomori et al. The All-Particle Spectrum of Primary Cosmic Rays in the Wide Energy Range from 1014 to 1017 eV Observed with the Tibet-III Air-Shower Array. *The Astrophysical Journal*, 678(2):1165, 2008.

[9] M. G. Aartsen et al. Measurement of the cosmic ray energy spectrum with IceTop-73. *Phys. Rev. D*, 88:042004, Aug 2013.

[10] R. Alfaro et al. All-particle cosmic ray energy spectrum measured by the HAWC experiment from 10 to 500 TeV. *Phys. Rev. D*, 96:122001, Dec 2017.

[11] Darko Veberič, editor. *The Pierre Auger Observatory: Contributions to the 35th International Cosmic Ray Conference (ICRC 2017)*, 2017.

[12] Yoshiki Tsunesada et al. Energy Spectrum of Ultra-High-Energy Cosmic Rays Measured by The Telescope Array. *PoS*, ICRC2017:535, 2018.

[13] N. Grevesse, M. Asplund, and A. J. Sauval. The Solar Chemical Composition. *Nucl.Phys.A*, 777, 2006.

[14] M. Casolino et al. Launch of the Space experiment PAMELA. *Adv. Space Res.*, 42:455–466, 2008.

[15] O. Adriani et al. Time dependence of the proton flux measured by pamela during the 2006 july-2009 december solar minimum. *The Astrophysical Journal*, 765(2):91, 2013.

[16] T. Antoni et al. KASCADE measurements of energy spectra for elemental groups of cosmic rays: Results and open problems. *Astropart. Phys.*, 24:1–25, 2005.

[17] Andreas Haungs. Cosmic Rays from the Knee to the Ankle. *Phys. Procedia*, 61:425–434, 2015.

[18] The KASCADE-Grande Collaboration et al. The spectrum of high-energy cosmic rays measured with KASCADE-Grande. *ArXiv e-prints*, June 2012.

[19] Alexander Aab et al. Observation of a Large-scale Anisotropy in the Arrival Directions of Cosmic Rays above 8×10^{18} eV. *Science*, 357(6537):1266–1270, 2017.

[20] R. U. Abbasi et al. First observation of the Greisen-Zatsepin-Kuzmin suppression. *Phys. Rev. Lett.*, 100:101101, 2008.

[21] J. Abraham et al. Observation of the suppression of the flux of cosmic rays above 4×10^{19}eV. *Phys. Rev. Lett.*, 101:061101, 2008.

[22] A. Aab et al. Depth of maximum of air-shower profiles at the Pierre Auger Observatory. II. Composition implications. *Phys. Rev.*, D90(12):122006, 2014.

[23] R. U. Abbasi et al. Study of Ultra-High Energy Cosmic Ray composition using Telescope Array's Middle Drum detector and surface array in hybrid mode. *Astropart. Phys.*, 64:49–62, 2015.

[24] R. Abbasi et al. Report of the Working Group on the Composition of Ultra High Energy Cosmic Rays. *JPS Conf. Proc.*, 9:010016, 2016.

[25] T. Abu-Zayyad et al. Measurement of the cosmic ray energy spectrum and composition from 10**17-eV to 10**18.3-eV using a hybrid fluorescence technique. *Astrophys. J.*, 557:686–699, 2001.

[26] V. L. Ginzburg and S. I. Syrovatskii. *The Origin of Cosmic Rays*. 1964.

[27] E. Fermi. On the origin of the cosmic radiation. *Phys. Rev.*, 75:1169–1174, Apr 1949.

[28] E. Fermi. Galactic Magnetic Fields and the Origin of Cosmic Radiation. *ApJ*, 119:1, Jan 1954.

[29] J. D. Finke et al. Modeling the Extragalactic Background Light from Stars and Dust. *ApJ*, 712:238–249, March 2010.

[30] F. W. Stecker et al. Intergalactic Photon Spectra from the Far-IR to the UV Lyman Limit for $0 < z < 6$ and the Optical Depth of the Universe to High-Energy Gamma Rays. *ApJ*, 648:774–783, September 2006.

[31] P. Padovani, D. M. Alexander, R. J. Assef, B. De Marco, P. Giommi, R. C. Hickox, G. T. Richards, V. Smolcic, E. Hatziminaoglou, V. Mainieri, and M. Salvato. Active Galactic Nuclei: what's in a name? 2017.

[32] D. J. Mortlock et al. A luminous quasar at a redshift of $z = 7.085$. *Nature*, 474:616–619, June 2011.

[33] Marie-Helene Ulrich et al. Variability of active galactic nuclei. *Annual Review of Astronomy and Astrophysics*, 35(1):445–502, 1997.

[34] A. Merloni and S. Heinz. *Evolution of Active Galactic Nuclei*, page 503. 2013.

[35] J. V. Wall. The quasars from the Parkes 2700-MHz survey. *The Observatory*, 95:196–204, October 1975.

[36] J. A. Peacock and S. F. Gull. Multifrequency models for the cosmological evolution of extragalactic radio sources. *Monthly Notices of the Royal Astronomical Society*, 196(3):611–633, 1981.

[37] Chris J. Willott et al. The radio luminosity function from the low-frequency 3crr, 6ce and 7crs complete samples. *Monthly Notices of the Royal Astronomical Society*, 322(3):536–552, 2001.

[38] C. M. Urry and P. Padovani. Unified Schemes for Radio-Loud Active Galactic Nuclei. *PASP*, 107:803, September 1995.

[39] P. Giommi, P. Padovani, and G. Polenta. A simplified view of blazars: the γ-ray case. *MNRAS*, 431:1914–1922, May 2013.

[40] R. Barvainis. Hot dust and the near-infrared bump in the continuum spectra of quasars and active galactic nuclei. *ApJ*, 320:537–544, September 1987.

[41] R. Antonucci. Unified models for active galactic nuclei and quasars. *ARAA*, 31:473–521, 1993.

[42] Ivan Hubeny et al. Non-lte models and theoretical spectra of accretion disks in active galactic nuclei. iv. effects of compton scattering and metal opacities. *The Astrophysical Journal*, 559(2):680, 2001.

[43] J. A. Baldwin. Luminosity Indicators in the Spectra of Quasi-Stellar Objects. *ApJ*, 214:679–684, June 1977.

[44] J. Torrealba, V. Chavushyan, I. Cruz-González, T. G. Arshakian, E. Bertone, and D. Rosa-González. Optical Spectroscopic Atlas of the MOJAVE/2cm AGN Sample. *RMxAA*, 48:9–40, April 2012.

[45] R. A. Jansen, D. Fabricant, M. Franx, and N. Caldwell. Spectrophotometry of Nearby Field Galaxies: The Data. *ApJS*, 126:331–397, February 2000.

[46] B. Luo et al. The Chandra Deep Field-South Survey: 7 Ms Source Catalogs. *APJS*, 228:2, January 2017.

[47] Marat Gilfanov and Andrea Merloni. Observational appearance of black holes in x-ray binaries and agn. *Space Science Reviews*, 183(1):121–148, Sep 2014.

[48] M. Ackermann et al. Search for gamma-ray emission from x-ray-selected seyfert galaxies with fermi-lat. *The Astrophysical Journal*, 747(2):104, 2012.

[49] P. Padovani and P. Giommi. The connection between x-ray- and radio-selected BL Lacertae objects. *ApJ*, 444:567–581, May 1995.

[50] A. A. Abdo et al. The Spectral Energy Distribution of Fermi Bright Blazars. *ApJ*, 716:30–70, June 2010.

[51] L. Maraschi et al. A jet model for the gamma-ray emitting blazar 3C 279. *ApJ*, 397:L5–L9, September 1992.

[52] M. Böttcher et al. Leptonic and Hadronic Modeling of Fermi-detected Blazars. *ApJ*, 768:54, May 2013.

[53] P. Padovani, E. Resconi, P. Giommi, B. Arsioli, and Y. L. Chang. Extreme blazars as counterparts of IceCube astrophysical neutrinos. *Monthly Notices of the Royal Astronomical Society*, 457(4):3582–3592, 2016.

[54] Elisa Resconi, Stefan Coenders, Paolo Padovani, Paolo Giommi, and Lorenzo Caccianiga. Connecting blazars with ultra high energy cosmic rays and astrophysical neutrinos. 10(February):1–10, 2016.

[55] J. Terrell. Luminosity Fluctuations and a Local Model of Quasi-Stellar Objects. *ApJ*, 147:827, February 1967.

[56] M. Böttcher and C. D. Dermer. Timing signatures of the internal-shock model for blazars. *The Astrophysical Journal*, 711(1):445, 2010.

[57] W. Max-Moerbeck et al. Time correlation between the radio and gamma-ray activity in blazars and the production site of the gamma-ray emission. *MNRAS*, 445:428–436, November 2014.

[58] M. Ajello et al. The Origin of the Extragalactic Gamma-Ray Background and Implications for Dark Matter Annihilation. *ApJ*, 800:L27, February 2015.

[59] M. S. Longair. *High Energy Astrophysics*. February 2011.

[60] M. Böttcher. Models for the Spectral Energy Distributions and Variability of Blazars. *ArXiv e-prints*, June 2010.

[61] F. Tavecchio and G. Ghisellini. Spine-sheath layer radiative interplay in subparsec-scale jets and the TeV emission from M87. *MNRAS*, 385:L98–L102, March 2008.

[62] R.-Y. Liu et al. A hadronuclear interpretation of a high-energy neutrino event coincident with a blazar flare. *ArXiv e-prints*, July 2018.

[63] P. Padovani et al. A simplified view of blazars: The neutrino background. *Monthly Notices of the Royal Astronomical Society*, 452(2):1877–1887, 2015.

[64] S. Dimitrakoudis, M. Petropoulou, and A. Mastichiadis. Self-consistent neutrino and UHE cosmic ray spectra from Mrk 421. *Astroparticle Physics*, 54:61–66, February 2014.

[65] P. Giommi, P. Padovani, G. Polenta, S. Turriziani, V. D'Elia, and S. Piranomonte. A simplified view of blazars: Clearing the fog around long-standing selection effects. *Monthly Notices of the Royal Astronomical Society*, 420(4):2899–2911, 2012.

[66] M. Ackermann et al. The Spectrum of Isotropic Diffuse Gamma-Ray Emission between 100 MeV and 820 GeV. *ApJ*, 799:86, January 2015.

[67] David S.N. Rupke and Sylvain Veilleux. Integral field spectroscopy of massive, kiloparsec-scale outflows in the infrared-luminous QSO Mrk 231. *Astrophysical Journal Letters*, 729(2 PART II), 2011.

[68] Nahum Arav et al. Quasar outflows and AGN feedback in the extreme UV: HST/COS observations of HE 0238-1904. *Monthly Notices of the Royal Astronomical Society*, 436(4):3286–3305, 2013.

[69] A. others Lamastra. Galactic outflow driven by the active nucleus and the origin of the gamma-ray emission in NGC 1068. 68(Ic):1–12, 2016.

[70] Kastytis Zubovas and Andrew King. Clearing out a galaxy. *The Astrophysical Journal Letters*, 745(2):L34, 2012.

[71] Andrew King and Ken Pounds. Powerful Outflows and Feedback from Active Galactic Nuclei. 200(2), 2015.

[72] F. Fiore et al. AGN wind scaling relations and the co-evolution of black holes and galaxies. pages 1–23, 2017.

[73] K. A. Pounds et al. A high-velocity ionized outflow and xuv photosphere in the narrow emission line quasar pg1211+143. *Monthly Notices of the Royal Astronomical Society*, 345(3):705–713, 2003.

[74] F. Tombesi et al. Evidence for ultra-fast outflows in radio-quiet active galactic nuclei. ii. detailed photoionization modeling of fe k-shell absorption lines. *The Astrophysical Journal*, 742(1):44, 2011.

[75] Xiawei Wang and Abraham Loeb. Probing the gaseous halo of galaxies through non-thermal emission from AGN-driven outflows. *Monthly Notices of the Royal Astronomical Society*, 453(1):837–848, 2015.

[76] A. Lamastra et al. Extragalactic gamma-ray background from AGN winds and star-forming galaxies in cosmological galaxy formation models. 2017.

[77] Xiawei Wang and Abraham Loeb. Quasar-driven Outflows Account for the Missing Extragalactic γ -Ray Background. *arXiv preprint*, 2016.

[78] Xiawei Wang and Abraham Loeb. Cumulative neutrino background from quasar-driven outflows. *Journal of Cosmology and Astroparticle Physics*, 2016(12), 2016.

[79] Ruo-Yu Liu et al. Can winds driven by active galactic nuclei account for the extragalactic gamma-ray and neutrino backgrounds? pages 1–16, 2017.

[80] Xiawei Wang and Abraham Loeb. Ultrahigh energy cosmic rays from nonrelativistic quasar outflows. *Physical Review D*, 95(6):4–8, 2017.

[81] The IceCube Collaboration. *Latest results on astrophysical neutrinos using high-energy events with contained vertices*. Zenodo, Jun 2018.

[82] The Pierre Auger Collaboration. The Pierre Auger Observatory: Contributions to the 34th International Cosmic Ray Conference (ICRC 2015). *ArXiv e-prints*, September 2015.

[83] M. Fukushima. Recent results from telescope array. In *European Physical Journal Web of Conferences*, volume 99 of *European Physical Journal Web of Conferences*, page 04004, August 2015.

[84] K. Greisen. End to the Cosmic-Ray Spectrum? *Physical Review Letters*, 16:748–750, April 1966.

[85] G. T. Zatsepin and V. A. Kuz'min. Upper Limit of the Spectrum of Cosmic Rays. *Soviet Journal of Experimental and Theoretical Physics Letters*, 4:78, August 1966.

[86] J. Ahrens et al. Muon track reconstruction and data selection techniques in AMANDA. *Nucl. Instrum. Meth.*, A524:169–194, 2004.

[87] A. Cooper-Sarkar, P. Mertsch, and S. Sarkar. The high energy neutrino cross-section in the Standard Model and its uncertainty. *Journal of High Energy Physics*, 8:42, August 2011.

[88] R. Gandhi et al. Ultrahigh-energy neutrino interactions. *Astroparticle Physics*, 5:81–110, August 1996.

[89] M. G. Aartsen et al. The IceCube Neutrino Observatory: Instrumentation and online systems. *Journal of Instrumentation*, 12(3), 2017.

[90] M. Ackermann et al. Optical properties of deep glacial ice at the south pole. *Journal of Geophysical Research D: Atmospheres*, 111(13), 7 2006.

[91] N. van Eijndhoven, O. Fadiran, and G. Japaridze. Implementation of a Gauss convoluted Pandel PDF for track reconstruction in Neutrino Telescopes. *Astropart. Phys.*, 28:456–462, 2007.

[92] M. G. Aartsen et al. Energy Reconstruction Methods in the IceCube Neutrino Telescope. *JINST*, 9:P03009, 2014.

[93] C. Patrignani et al. Review of Particle Physics. *Chin. Phys.*, C40(10):100001, 2016.

[94] R. Abbasi et al. Measurement of the atmospheric neutrino energy spectrum from 100 GeV to 400 TeV with IceCube. *Phys. Rev.*, D83:012001, 2011.

[95] M. G. Aartsen et al. The IceCube Neutrino Observatory - Contributions to ICRC 2017 Part II: Properties of the Atmospheric and Astrophysical Neutrino Flux. 2017.

[96] Kwang-Chang Lai, Guey-Lin Lin, and T. C. Liu. Determination of the Neutrino Flavor Ratio at the Astrophysical Source. *Phys. Rev.*, D80:103005, 2009.

[97] M. G. Aartsen et al. The IceCube Neutrino Observatory Part II: Atmospheric and Diffuse UHE Neutrino Searches of All Flavors. In *Proceedings, 33rd International Cosmic Ray Conference (ICRC2013): Rio de Janeiro, Brazil, July 2-9, 2013*, 2013.

[98] Stefan Schonert, Thomas K. Gaisser, Elisa Resconi, and Olaf Schulz. Vetoing atmospheric neutrinos in a high energy neutrino telescope. *Phys. Rev.*, D79:043009, 2009.

[99] M. G. Aartsen et al. Evidence for High-Energy Extraterrestrial Neutrinos at the IceCube Detector. *Science*, 342:1242856, 2013.

[100] M. G. Aartsen et al. Differential limit on the extremely-high-energy cosmic neutrino flux in the presence of astrophysical background from nine years of IceCube data. *Phys. Rev.*, D98(6):062003, 2018.

[101] Icecube realtime hese - amon - gcn. `https://gcn.gsfc.nasa.gov/amon.html`.

[102] M. G. Aartsen et al. The IceCube Neutrino Observatory - Contributions to ICRC 2017 Part I: Searches for the Sources of Astrophysical Neutrinos. 2017.

[103] M. G. Aartsen et al. All-sky Search for Time-integrated Neutrino Emission from Astrophysical Sources with 7 yr of IceCube Data. *Astrophys. J.*, 835(2):151, 2017.

[104] R. Abbasi et al. Time-integrated Searches for Point-like Sources of Neutrinos with the 40-string IceCube Detector. *ApJ*, 732:18, 2011.

[105] M. G. Aartsen et al. Search for Time-independent Neutrino Emission from Astrophysical Sources with 3 yr of IceCube Data. *Astrophys. J.*, 779:132, 2013.

[106] Kai Schatto. Stacked searches for high-energy neutrinos from blazars with IceCube. *PhD Thesis*, Johannes Gutenberg University Mainz, 2014.

[107] M. G. Aartsen et al. Searches for Extended and Point-like Neutrino Sources with Four Years of IceCube Data. *Astrophys. J.*, 796(2):109, 2014.

[108] M. G. Aartsen et al. Searches for small-scale anisotropies from neutrino point sources with three years of IceCube data. *Astropart. Phys.*, 66:39–52, 2015.

[109] A. A. Abdo et al. A Measurement of the Spatial Distribution of Diffuse TeV Gamma Ray Emission from the Galactic Plane with Milagro. *Astrophys. J.*, 688:1078–1083, 2008.

[110] A. A. Abdo et al. Spectrum and Morphology of the Two Brightest Milagro Sources in the Cygnus Region: MGRO J2019+37 and MGRO J2031+41. *Astrophys. J.*, 753:159, 2012.

[111] Alexis Popkow. The VERITAS Survey of the Cygnus Region of the Galaxy. *PoS*, ICRC2015:750, 2016.

[112] B. Hona, A. Robare, H. Fleischhack, and P. Huentemeyer. Correlated GeV–TeV Gamma-Ray Emission from Extended Sources in the Cygnus Region. *PoS*, ICRC2017:710, 2018. [35,710(2017)].

[113] Tova M. Yoast-Hull, John S. Gallagher III, Francis Halzen, Ali Kheirandish, and Ellen G. Zweibel. The γ-Ray Puzzle in Cygnus X: Implications for High-Energy Neutrinos. 2017.

[114] Mehmet Guenduez, Julia Becker Tjus, Björn Eichmann, and Francis Halzen. Identification of Gamma-Rays and Neutrinos from the Cygnus-X Complex Considering Radio Gamma Correlation. 2017.

[115] M. G. Aartsen et al. The contribution of Fermi-2LAC blazars to the diffuse TeV-PeV neutrino flux. *Astrophys. J.*, 835(1):45, 2017.

[116] P. Padovani, A. Turcati, and E. Resconi. AGN outflows as neutrino sources: an observational test. *Mon. Not. Roy. Astron. Soc.*, 477(3):3469–3479, 2018.

[117] W. B. Atwood et al. The Large Area Telescope on the Fermi Gamma-Ray Space Telescope Mission. *ApJ*, 697:1071–1102, Jun 2009.

[118] M. Ajello et al. 3FHL: The Third Catalog of Hard Fermi-LAT Sources. *Astrophys. J. Suppl.*, 232(2):18, 2017.

[119] M. Ackermann et al. The First Fermi-LAT Catalog of Sources Above 10 GeV. *Astrophys. J. Suppl.*, 209:34, 2013.

[120] M. Ackermann et al. 2FHL: The Second Catalog of Hard Fermi-LAT Sources. *Astrophys. J. Suppl.*, 222(1):5, 2016.

[121] B. Arsioli, Y.L. Chang, P. Giommi, P. Padovani, and E. Resconi. Private communication.

[122] Chang Y.L., B. Arsioli, P. Giommi, P. Padovani, E. Resconi, and T. Glauch. Private communication.

[123] Y. L. Chang, B. Arsioli, P. Giommi, and P. Padovani. 2WHSP: A multi-frequency selected catalogue of high energy and very high energy γ-ray blazars and blazar candidates. *Astron. Astrophys.*, 598:A17, 2017.

[124] Chang Y.L., B. Arsioli, P. Giommi, P. Padovani, E. Resconi, T. Glauch, and A. Turcati. Private communication.

[125] IceCube Collaboration et al. Neutrino emission from the direction of the blazar TXS 0506+056 prior to the IceCube-170922A alert. *Science*, 361:147–151, July 2018.

[126] P. Padovani, F. Oikonomou, M. Petropoulou, P. Giommi, and E. Resconi. TXS 0506+056, the first cosmic neutrino source, is not a BL Lac. *Mon. Not. Roy. Astron. Soc.*, 484:L104, 2019.

[127] Alexander Aab et al. The Pierre Auger Cosmic Ray Observatory. *Nucl. Instrum. Meth.*, A798:172–213, 2015.

[128] H. Kawai et al. Telescope Array Experiment. *Nuclear Physics B Proceedings Supplements*, 175:221–226, January 2008.

[129] Alexander Aab et al. Searches for Anisotropies in the Arrival Directions of the Highest Energy Cosmic Rays Detected by the Pierre Auger Observatory. *Astrophys. J.*, 804(1):15, 2015.

[130] R. U. Abbasi et al. Indications of Intermediate-Scale Anisotropy of Cosmic Rays with Energy Greater Than 57 EeV in the Northern Sky Measured

with the Surface Detector of the Telescope Array Experiment. *Astrophys. J.*, 790:L21, 2014.

[131] Alexander Aab et al. An Indication of anisotropy in arrival directions of ultra-high-energy cosmic rays through comparison to the flux pattern of extragalactic gamma-ray sources. *Astrophys. J.*, 853(2):L29, 2018.

[132] Darko Veberič, editor. *The IceCube Neutrino Observatory, the Pierre Auger Observatory and the Telescope Array: Joint Contribution to the 35th International Cosmic Ray Conference (ICRC 2017)*, 2018.

[133] J. R. Mullaney, D. M. Alexander, S. Fine, A. D. Goulding, C. M. Harrison, and R. C. Hickox. Narrow-line region gas kinematics of 24,264 optically-selected AGN: the radio connection. *Mon. Not. Roy. Astron. Soc.*, 433:622, 2013.

[134] C. M. Harrison, D. M. Alexander, J. R. Mullaney, and A. M. Swinbank. Kiloparsec-scale outflows are prevalent among luminous AGN: outflows and feedback in the context of the overall AGN population. *Mon. Not. Roy. Astron. Soc.*, 441(4):3306–3347, 2014.